Computational Study of Solid-State Superionic Conductor using DFT & Bond Valence Approaches

Thesis submitted in accordance with the requirements of the University of Liverpool for the degree of Doctor in Philosophy by

Rhun Elfed Morris

Supervised by

Dr Matthew S. Dyer & Prof Matthew J. Rosseinsky

January 2022

Contents

Acknowledgements

I would like to sincerely thank my supervisors Dr Matthew Dyer and Prof Matthew Rosseinsky. Dr Matthew Dyer provided endless support and encouragement throughout the research and was always willing to aid with any query I had, no matter how insignificant. Prof Matthew Rosseinsky gave thorough feedback and guidance throughout. Both Dr Matthew S. Dyer and Prof Matthew J. Rosseinsky‘s support and guidance has helped further my development as an academic, researcher and professional for which I will always be grateful. I would also like to thank Dr. John B. Claridge, Dr. Paul Sharp and Dr Chris Collins which gave me assistance with any queries throughout my research, and I would like to thank the wider MJR Solid State research group which provided valuable feedback during my research. Without the generosity of the above, this thesis would not have been possible.

During my time at the University of Liverpool I have gained a broad range of new skills professionally and most importantly I have made new friends and connections both personally and professionally. My skills within research and my understanding of how research at the forefront of the field have expanded beyond my expectation. I have also developed knowledge and skills outside of academia which includes entrepreneurship and business training which was provided by the University of Liverpool which will pave the way for my career ahead of me.

I would also like to thank my friends and family for the support they have given me throughout my studies.

Through such unprecedented times with significant change to how research can be carried out, I would also like to acknowledge the continuous support given by Dr Matthew Dyer which helped to adapt and overcome the difficulties faced.

Preface

The content within this thesis is the research I carried out from the 11th of October 2017 over a three-and-a-half-year period. The work I have carried out was done from the Surface Science Research Centre at the University of Liverpool. Work was also done in co-ordination and collaboration of many colleagues who are experimental researchers within the Materials Innovation Factory at the University of Liverpool. My own research was carried out as a part of the Rosseinsky research group which was led by Prof Matthew J Rosseinsky at the Materials Innovation Factory as well as Dr Matthew Dyer's research group from within the Surface Science Research Centre.

Computational research within this study was carried out by myself unless stated and sourced otherwise from referenced resources. Experimental research within this thesis was carried out by my colleagues from the Rosseinsky research group and is stated as so in the chapters. Experimental results are included for completeness of discussion of the materials which have been studied, as the primary function of the computational research is to identify new potential materials which are experimentally viable.

Rhun E. Morris

2021/22

Abstract

Currently, attempts are being made to identify an ‘ideal’ solid state superionic conductor that is viable as a solid-state electrolyte, but the significant problem being faced is the high cost, toxicity, stability, and conductivity of current candidates. With the development of new materials, new challenges are faced which hinder their performance. Solid-state electrolytes face significant degradation in performance from dendrite formation as an example of one of the major issues faced. To improve upon materials which are currently in use, this research aims to identify a viable alternative, using doping mechanisms and chemical intuition, which is not burdened with the problems listed above. The work carried out in this thesis aims to use computational approaches to firstly identify new potential solid state electrolyte materials and cathode materials with the objective of resolving the issues faced by the technology. Work has also been carried out with the objective of developing new approaches to materials discovery for solid state conductors through high-throughput computation.

The use of the Goldschmidt tolerance factor was used for the lithium rich anti-perovskites as an indicative way of probing for new anion and cation combinations, more specifically the Li_3XF (X = S, Se), Li_3XOH (X = S, Se) and Li_2MOS (M = Ca, Mg, Zn) anti-perovskites and their distorted structure’s stabilities were analysed using a DFT approach identifying their convex hull energies. The most promising candidate was found to be Li_3SeF, but the attempted synthesis of the compound was unsuccessful. Although the study did not produce any new compounds, it demonstrated that the lithium rich anti-perovskite structures are an area which could be further explored to identify new conductor materials.

A computational investigation was carried out on the $Na_2Fe_2OS_2$ oxychalcogenide which was successfully synthesised by Jacinthe Gamon and Arnaud J. Perez. The objective of the work carried out was to identify the stability and magnetic ordering of the structure using DFT calculations to determine the convex hull energy of the structure, thus the stability, and by using bandstructure, bandgap and phonon frequency plots. The investigation identified that the most stable magnetic

ordering was the blocked checkerboard ordering which was classified as stable with the convex hull energy of 0 meV/atom above the hull.

High-throughput approach to identifying potential new superionic conductors was explored. The primary approach used was the bond valence sum mapping method due to its low computational cost. We also used the lithium occupancy and minimum lithium occupancy metric as a method of screening. There was no clear metric which correlated strongly to conductivity out of the dataset used. Although the study didn't identify a clear correlation for a given metric, it did however identify areas in which further studies could lead to stronger correlations from combining metrics and how a larger dataset might create a more in-depth understanding of the correlations.

Finally, the stabilities of the anti-bixbyite magnesium structures of $Mg_{2.75}X_{0.125}N_2$ (X = Zr, Sn, Si), $Mg_{2.625}X_{0.25}N_2$ (X = Al, Ga, In) and the $Mg_{3.125}N_{1.75}Si_{0.25}$ was identified using the convex hull energy of each compound. The study identified a series of them to be metastable but attempts of synthesising the metastable structures were unsuccessful. Although further synthetic studies could yield results in creating the doped structures.

Chapter 1: Introduction

The information given in this chapter will provide background context, concepts and information of current advances and progress being made within research surrounding the topics of this thesis.

1.1. Introduction to Battery Technology & Current Challenges

Battery cells conventionally, consist of an anode, cathode, electrolyte, and a separator illustrated in **figure 1.1**. The anode is constructed of a negative electrode material where the oxidation half-reaction occurs. Most commonly, graphite is used as an anode in lithium batteries as it is electrically conductive, able to intercalate lithium and is abundant. The cathode is a positive electrode material, where the reduction half reaction occurs. Lithium cobalt oxide is a commonly used material as a cathode for lithium-ion batteries.[1] The electrolyte serves as a phase in which charge carriers can migrate through the cell. The separator is a membrane which allows for the transport of charge carriers whilst separating the anode and cathode to ensure a short-circuit of the cell does not occur. The electrochemical process consists of galvanic cell function when discharging and an electrolytic cell function when recharging.

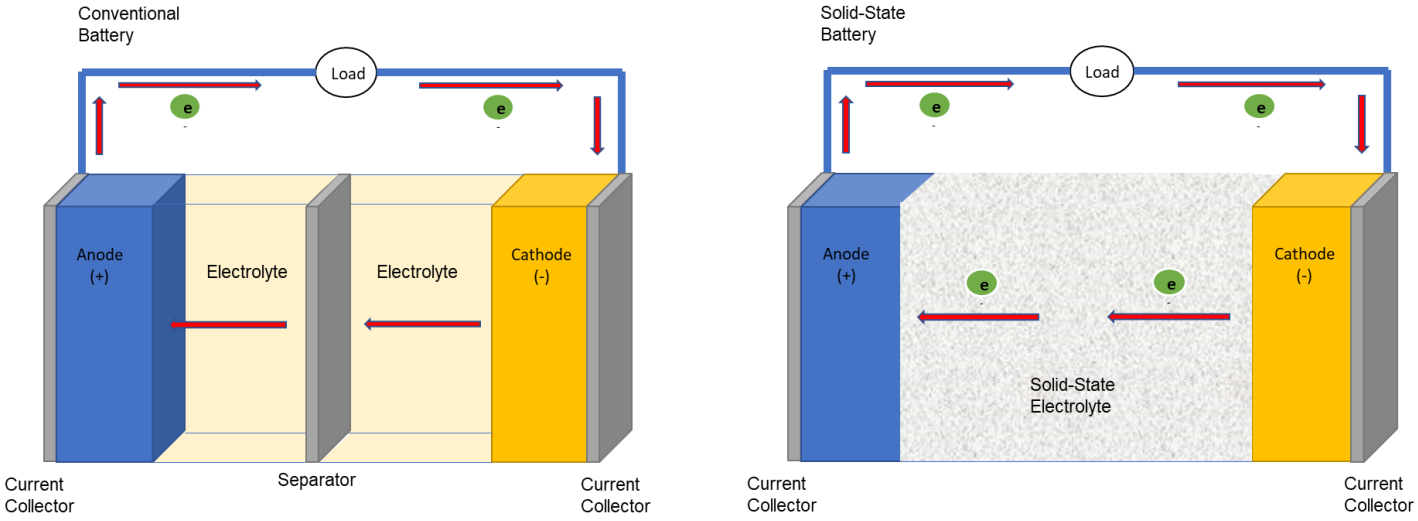

Figure 1.1. Conventional battery schematic (left) and solid-state battery schematic (right) under discharge.

In lithium-ion batteries, using a $LiCoO_2$-Graphite battery as an example. The charging process consists of an oxidation, delithiation and intercalation of $LiCoO_2$ with graphite. The discharging process consists of a reduction and de-intercalation of the lithiated carbon.

$$LiCoO_2 \rightleftharpoons CoO_2 + Li^+ + e^- \quad (1)$$

$$Li^+ + C_6 + e^- \rightleftharpoons LiC_6 \quad (2)$$

$$LiC_6 + CoO_2 \rightleftharpoons LiCoO_2 + C_6 \quad (3)$$

The reversible half-reactions 1 and 2 show the process of oxidation and delithiation of $LiCoO_2$ and intercalation of graphite carbon with the lithium. Reaction 3 shows the overall reaction where the process of discharging is seen from left to right and charging from right to left.

In recent years, the demand for new methods of energy production and storage has increased significantly. The use of traditional energy sources such as fossil fuels coal, oils and gas is finite and is becoming ever increasingly scarce. Research within scientific fields has become more focused on finding alternative production methods and energy storage. Becoming reliant on sustainable energy sources such as solar, wind and hydropower is not currently viable due to its inability to produce constant reliable energy, therefore a large focus area is on creating viable energy storage options. For example, batteries and fuel cells have become a popular area of focus within scientific research. Identifying and developing a new energy storage technology where energy can be readily stored and used would lead to economic, environmental, and technological advances, which would be a driving force behind a large change in energy reliance from traditional fossil fuels to using more environmentally friendly and sustainable methods of energy production to supply energy needs within industry, households and with transport. New viable materials would also be of great importance to the portable and smart device industry as well as the automotive industry as the most efficient technology would provide a significant marketing advantage.[2,3]

Battery technology relies heavily on the materials used. Currently lithium-ion battery technology primarily utilizes liquid electrolytes for example $LiPF_6$ and propylene carbonate dissolved $LiClO_4$. These liquid electrolytes are commonly used in portable devices such as mobile phones, laptops, digital cameras etc. $LiClO_4$ type electrolytes face many problems, an example of this would be that they are highly environmentally unfriendly as the liquid within the battery is highly corrosive, toxic, flammable and can be damaging if discarded improperly, they also suffer from a limited temperature range of operation. Current research includes attempting to improve the lithium-battery technology using lithium-metal, lithium-oxygen and lithium-sulphur technologies, these have also been widely reviewed. [4–6] There has been a large amount of research carried out to find possible alternative materials for a solid electrolyte. Lithium batteries that use a liquid electrolyte are very hazardous due to the highly reactive lithium solid being used in conjunction with a liquid electrolyte which can cause a thermal runaway reaction and lead to fires/explosions. The benefit of using a solid electrolyte rather than a liquid electrolyte would be due to it eliminating the risk posed by the liquid electrolyte as the electrodes would be separated by a solid ceramic electrolyte. Current materials that have been explored include superionic conductors such as NASICONs, LISICONs, Thio-LISICONs, Rock-salt type superionic conductors, perovskite and anti-perovskite structured superionic conductors.

To offer a technological advance in its use, a new conductor material must meet certain criteria which includes; (i) inexpensive, light and low toxicity (economic and environmentally friendly) (ii) Significant reduction in corrosion, leakage and must be thermomechanically strong, (iii) must have a large working window in relation to voltage and current, (iv) must have minimum amounts of self-discharge for a longer shelf-life, (v) must be stable in a broad temperature range of -20^{o}C to 50^{o}C, and most importantly (vi) must have a high ionic conductivity in the order of 10^{-2} S/cm at room temperature. [7]

Conventional batteries have many significant disadvantages, to attempt to solve the issues presented by electrolyte solutions two different methods are used within research. These include using a form of plasticizer to make the liquid electrolyte into a solid form and attempting to synthesize solids which

match the criteria previously mentioned in the introduction.[8,9] Currently there are a large number of structure types that have been investigated and that currently are being investigated to try and propose new viable options as solid state superionic conductors.

1.2. Current Research: Solid-State Electrolytes & Computational Studies

Current materials that have been explored include superionic conductors such as NASICONs, lithium-NASICONs, thio-LISICON, rock-salt type superionic conductor, garnet type structures, perovskite, and anti-perovskite structured superionic conductors. For structures such as NASICONs where there is a large quantity of literature, they can be separated by their mobile ion i.e., lithium type NASICONs with a mobile Li^+ ion, copper type NASICONs with mobile Cu^+ ions etc. [8]. Similar principles can be applied to rock-salt type structures, perovskites, and anti-perovskites. For example, perovskites and anti-perovskites could be separated based on the species of the A-site, B-site and C-site ions and the applications of various structures.

NASICON

In earlier years before the 1960s, ionic α-AgI, Ca^{2+} or Y^{3+} substituted ZrO_2 had been the focus of research as ionic conductors with ZrO_2 being a precursor as one of the eventual reactants to produce NASICONs. The research identified that the O^{2-} ion conductivity in Ca^{2+} or Y^{3+} stabilized zirconia was less than the traditionally used liquid electrolyte such as $LiClO_4$ and that silver halides readily decompose in air [8,10]. β-alumina ($Na_2O_{.11}Al_2O_3$) was synthesised in the 1960s which was identified as a very good Na^+ conductor. The β-alumina has a layered structure and migration of the Na^+ ions occur between two conductive planes.[11,12]

Restrictions caused by the β-alumina structure were overcome by one of the first NASICONs which was made by Hong and Goodenough et al [13,14]. The first report of a structure related to the NASICON family was a crystal structure of $NaM_2IV(PO_4)_3$ (MeIV = Ge, Ti, Zr) and the structure was studied using x-ray data (1968) [15]. Hong and Goodenough et al [13,14] , carried out synthesis and characterization of the more commonly known NASICON in 1976. The NASICON structure they had characterized and synthesised had a formula of $Na_{1+x}Zr_2Si_xP_{3-x}O_{12}$ ($0 \leq x \leq 3$), this is the more commonly known NASICON structure shown in **figure 1.2**. Compositions such as $NaZr_2P_3O_{12}$ (NZP) and $Na_4Zr_2Si_3O_{12}$ (NZS) have a rhombohedral crystal structure and a R3c space group, they also found that NASICONs that had compositions that were in the $1.8 \leq x \leq 2.2$ range distort under room temperature to a monoclinic crystal structure with a C2/c space group.

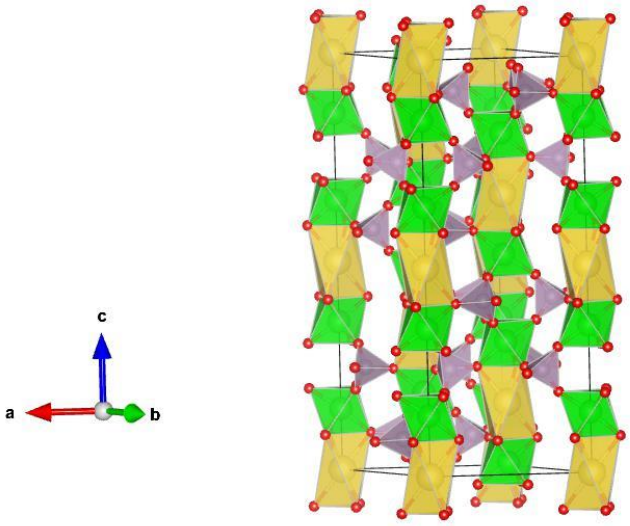

Figure 1.2. $NaZr_2P_3O_{12}$ (NZP) NASICON structure with Rhombohedral R3c space group. ICSD code 467. [13] Yellow polyhedra consist of O^{2-} co-ordinated Na, green polyhedra the O^{2-} co-ordinated Zr, and purple polyhedral the PO_4^{3-} groups.

The composition of NASICONs that are synthesised by solid-state reactions at high temperatures have been contested due to evidence within the grain boundary of ZrO2 impurity or other phase formation [16]. From this von Alpen et al [17] suggested a new formula of $Na_{1+x}Zr_{2-x/3}Si_xP_{3-x}O_{12-2x/3}$ in 1981. They also identified that with the new proposed structure compounds exhibit a pure monoclinic symmetry from $1.55 \leq x \leq 3$ and are stable with molten sodium and that they also exhibit high conductivities in the order of 10^{-3} S cm^{-1}.

For the NZP skeleton Alamo et al [18]. reviewed the crystal chemistry and properties, for example the NZP ion transport, ion exchange, poly/isomorphism, phase transitions, and the exchange and redox reactions with the NZP compound.

Research focusing on the synthesis and conductivity of the NASICON type compounds led to a question being asked regarding the Na^+ mobility depending on the structure and how the mobility could explain trends in conductivity. Tran Qui et al .[19] investigated the Na+ mobility and diffusion pathway with the NASICONs-type structure $Na_4Zr_2Si_3O_{12}$. They also investigated the diffusion pathway of Na^+ for $Na_{1+x}Zr_2P_{3-x}Si_xO_{12}$ (x = 0-3). They achieved this by using electron density maps and Fourier analysis. For both compounds they identified the main diffusion pathway for structures and that there is a direct relationship between conductivity and the size of the cell c parameter (hexagonal cell). In 1998 Losilla et al. [20] undertook a study on the Na mobility in NASICON materials, using Rietveld refinement of powder x-ray diffraction data, $^{31}P/^{23}Na$ MAS NMR and impedance data to determine the Na mobility/diffusion pathway within NASICONs. The NASICON composition being used in this study was $Na_{1.4}M_{1.6}In_{0.4}(PO_4)_3$ (M = Ti, Sn, Hf, Zr). The Rietveld refinement of powder x-ray diffraction data confirmed the rhombohedral NASICON structure with full occupancy, partial occupancy and random occupancy of the Na(1), Na(2), and octahedral In/M sites, respectively. From their research they found that M = Ti and Si NASICON compounds have a lower ionic conductivity at room temperature, M = Hf and Zr have a higher conductivity at room temperature and that a triangular bottleneck between O(1) and two O(2) positions are described as an irregular M1M2 conduction pathway for the Na^+ ion.

More recently computational methods have been employed to study the electronic and crystal structures of NASICONs, and to also look at the diffusion pathways and properties of the structures. Bui et al [21] also carried out similar research with $Na_3Zr_2Si_2PO_{12}$ based on density functional theory to also study the crystal and electronic structures and the diffusion mechanism of the NASICON compound. In their method they used density functional theory (DFT) via VASP (Vienna ab initio Simulation Package) whilst employing a Monkhorst-pack k-point sampling grid of 2x2x2, and an

energy cut-off of 500 eV for the plane-wave basis set. They also used the generalized gradient approximation (GGA), PBE (Perdew-Burke-Ernzerhof) functional to handle the exchange and correlation energy. Their study of the diffusion had been done by implementing one Na vacancy into the $Na_3Zr_2Si_2PO_{12}$ monoclinic cell which consists of 80 atoms (three formula units) and calculating the activation barriers using the nudged elastic band (NEB) method of the known diffusion pathways. For these calculations they set the convergence conditions for the energy and force calculations to 0.01 eV per formula unit and 0.01 eV $Å^{-1}$. This study confirmed that three-dimensional diffusion occurs in $Na_3Zr_2Si_2PO_{12}$ and that the material exhibits high ionic conductivity with three-dimensional diffusion.

NASICONs display great thermal and chemical stability and exhibit fast ionic conductivity. They have been extensively investigated, which includes research done on the NASICON structure using various constituents to achieve better stabilities, and ionic conductivity. Due to the wide array of research done on NASICONS and their constituent diversity, there has been a large number of computational studies done on the ionic conductivity, diffusion mechanism and migration pathways within the field.

Lithium-NASICONs (Li-NASICONs)

From extensive research being carried out on NASICONs and the impact it has created, a substantial amount of research has and is being carried out on NASICON-type structures that show resemblance to the structural formation of NASICON but with differing formulas. An example of this would be the research carried out by Takahashi et al [22] mentioned in the previous section on NASICONs. Lithium type-NASICONs have become an area of large interest as lithium is smaller and more lightweight than sodium, which leads to smaller and lighter batteries which is desirable in technological applications. Earlier studies on lithium containing NASICONs include one done by Taylor et al. [23] where they synthesised Li-NASICONs based on the structure of $LiZr_2(PO_4)_3$. The crystal structure of $LiZr_2(PO_4)_3$ can be seen in **figure 1.3**. The synthesised structures included $Li_{1-x}Zr_{2-x}Ta_x(PO_4)_3$ and $Li_{1-x}Hf_{2-x}Ta_x(PO_4)_3$. They carried out conductivity measurements on the newly synthesised Li-NASICONn

materials by measuring *a-c* conductance. The values obtained for the newly produced Li-NASICON materials were found to be in the range of 10^{-3} S cm^{-1} at 200°C. In 1986 Subramanian et al. [24] studied a range of Li-NASICONs which included; $LiZr_2(PO_4)_3$, $LiZr_{2-x}Ti_x(PO_4)_3$ (x = 0.1-2), $LiTi_2(PO_4)_3$, $Li_{1+x}Ti_{2-x}Sc_x(PO_4)_3$ and $Li_{1+x}Hf_{2-x}In_x(PO_4)_3$ ($LiB_2(PO_4)_3$, B = Ti, Zr and Hf). They identified their conductivities which varied from $2.1x10^{-5}$ S cm^{-1} at 300°C for $LiZr_2(PO_4)_3$, $5.0x10^{-3}$ S cm^{-1} at 300°C for $LiTi_2(PO_4)_3$ to $1.4x10^{-2}$ S cm^{-1} for $Li_{1.1}(Sc_{0.1}Ti_{1.9})(PO_4)_3$. The Li-NASICON $LiZr_2(PO_4)_3$ was found to be polymorphous and complex depending on the temperature used for its synthesis. Iglesias et al.[25] in 1998 conducted an investigation into the distortion and phase transition of $LiZr_2(PO_4)_3$. They found that in fact for the phase transition for $LiZr_2(PO_4)_3$ synthesised in temperatures in excess of 1100°C that the transition that actually occurs is from a triclinic configuration → rhombohedral, rather than the monoclinic → rhombohedral transition that Sudreau et al.[26] had reported. Multiple investigations have been carried out on Li-NASICON diversity. For example, Aono et al [27], in which lithium titanium phosphate with the addition or substitution of different mixed metal ions in the compound was investigated with focus on the properties and conductivity found with varying amounts of mixed metals.

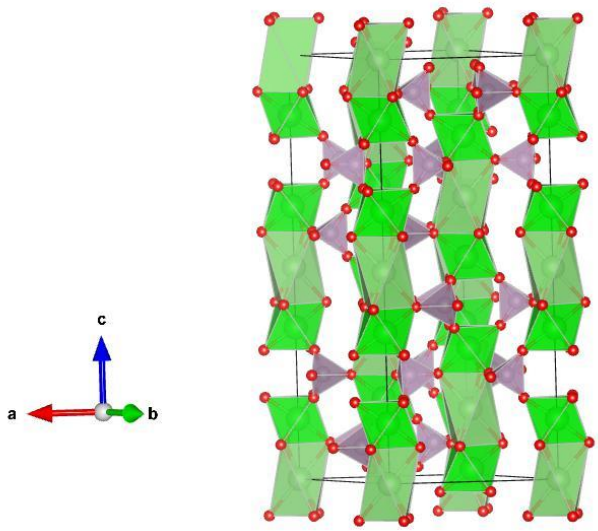

Figure 1.3. $LiZr_2(PO_4)_3$ (LZP) Li-NASICON structure with Rhombohedral R3c space group. ICSD code 201935.[28] Yellow polyhedral consist of O^{2-} co-ordinated Li, green polyhedral the O^{2-} co-ordinated Zr, and purple polyhedral the PO_4^{3-} groups.

Extensive research has also been carried out on the diffusion pathways for Li-Nasicons. Catti et al [29]. studied the lithium-ion diffusion pathway in the α- $LiZr_2(PO_4)_3$ using data collected from Powder

neutron diffraction. They found no phase transitions in the temperature range they carried out the study at (423 -873K). They also found that lithium was occupying a primary site and a secondary disordered site, which were displaced from Zr sites respectively. Both were coordinated to four Oxygen atoms (neighbouring). The lithium in the secondary site was found to have a stronger bond to the Oxygen atoms hence was the likely trapping site for Li along the main diffusion pathway along the Li network. More recent studies include research carried out by Cussen and Corr et al [30]. They improve on the performance of LZP ($LiZr_2(PO_4)_3$) as a solid-state electrolyte by reducing the impact of increased resistance that is found from having a large grain boundary. In this work, they use sol-gel chemistry to improve the densification of the material which leads to higher bulk conductivity which was found to be $1x10^{-4}$ S cm^{-1}.

Computational studies have also been conducted on lithium type NASICON structures in more recent years. The ability to use computational methods has proven useful in identifying the migration barriers, energetic properties and hence diffusion mechanisms in the structures and proves to be a valuable instrument in furthering research and developing knowledge of the compounds. One example of a computational study done on a Li-NASICON was done by Lang et al.[31] Where they used density functional theory to study the migration barriers for an interstitial Li ion and a lithium vacancy. This was done with a rhombohedral structure of $LiTi_2(PO_4)_3$. Calculations were also performed on other various structures following $LiX_2(PO_4)_3$, X = Si, Ge, Sn, Zr, Hf, Mo. The structure being analysed was a rhombohedral structure containing 108 atoms. Computational methods used for the calculations were done using the quantum ESPRESSO Pwscf code. Using a plane-wave basis set to express wavefunction of valence electrons and ultrasoft pseudopotentials for description of the ionic core and valence electron interactions. Generalised gradient approximation (GGA) Perdew, Bruke and Ernzerhof (PBE) was used for the exchange-correlation contribution. Cut-offs of 476 eV were used for the plane-wave basis and 5442 eV for the electron density representation. 3x3x1 Monkhorst pack grids were used for the calculations along with maximum force acting on atoms was set to less than 10^{-3} eV/Å. The nudged elastic band method (NEB) was used to calculate minimum energy paths of Li hopping between neighbouring metal sites.

As a part of the NASICON family Li-NASICONs have proven to be an area of particular interest within recent studies of solid-state superionic conductors. This is due to the high ionic conductivities achieved along with structures displaying high thermal and electrochemical stability. The relatively low cost of some Li-NASICON structures have made them particularly interesting due to their applicability and cost efficiency hence they are more suitable for commercial purposes.

Thio-Lisicons

Thio-Lisicons are a family of Lisicon type structures containing Sulphur. One of the first reported Thio-Lisicon structures was reported by Kanno et al.[32] where Li_2GeS_3, Li_4GeS_4, Li_2ZnGeS_4, $Li_{4-2x}Zn_xGeS_4$, Li_5GeS_4, $Li_{4+x+\delta}(Ge_{1-\delta-x}Ga_x)S_4$ were synthesised. Lattice and structure characterisation was performed using x-ray powder diffraction and Rietveld Refinement. Conductivity measurements of the compounds were done using AC impedance methods with a frequency range of 0.1 Hz to 10 MHz and at a temperature range of room temperature to 300ºC. The compound with the highest conductivity was found to be $Li_{4+x+\delta}(Ge_{1-\delta-x}Ga_x)S_4$ with a conductivity of $6.5x10^{-5}$ S/cm at 25ºC. Kanno et al also released an article shortly after investigating the Li_2S-GeS_2-P_2S_5 system. $Li_{4-x}Ge_{1-x}P_xS_4$ was synthesised with various values of x. X-ray powder diffraction was used for lattice and structural characterisation. Conductivity measurements were also carried out. The structure with the highest conductivity was found to be $Li_{4-x}Ge_{1-x}P_xS_4$ (x = 0.75) with a conductivity of $2.2x10^{-3}$ S/cm at 25ºC. Similar research was carried out on the Li_2S-P_2S_5 system where its most optimum conductivity was found to be $1.5x10^{-4}$ S cm^{-1} at 27ºC for $Li_{3+5x}P_{1-x}S_4$ (x = 0.065) [33]. Li_2ZrS_3 was also studied, for $Li_{2+2x}Zn_xZr_{1-x}S_3$, the highest conductivity was found at x = 0.1 with a conductivity of $1.2x10^{-4}$ S cm^{-1} at 30ºC [34].

Kamaya et al.[35] synthesised one of the most important Thio-Lisicons made, $Li_{10}GeP_2S_{12}$, shown in **figure 1.4**. It was found to have a conductivity of $1.2x10^{-2}$ S cm^{-1} at room temperature. The

conductivity found for this compound is extremely high, with one of the best conductivities found for Thio-Lisicons and for solid state superionic conductors studied to date.

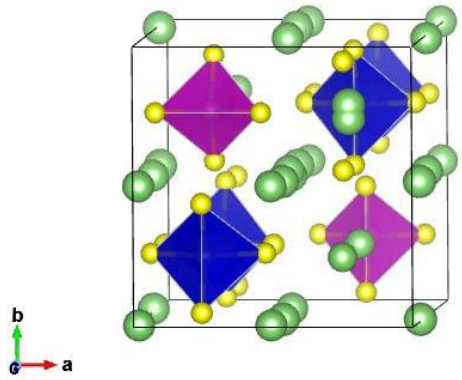

Figure 1.4. $Li_{10}GeP_2S_{12}$ Thio-lisicon structure. ICSD code 241493. [36] Ge and P polyhedral are shown as the blue and purple polyhedral respectively. Li diffusion pathways displayed along the [001] direction.

Computational studies have also been done on Thio-Lisicons, Mo et al.[37] investigated $Li_{10}GeP_2S_{12}$ and its diffusivity, stability and electrochemical window in an attempt to explain the 3D diffusion mechanism within the compound, rather than a 1D diffusion mechanism. In their investigation, they used an array of different first-principle methods, calculations were done using Vienna ab initio programme (VASP) with a projector augmented-wave approach (PAW) using the Perdew-Burke-Ernzerhof generalised-gradient approximation (GGA) to DFT (density functional theory). They found that LGPS ($Li_{10}GeP_2S_{12}$) in the phase diagram is a metastable phase. MD (molecular dynamics) calculations confirmed that diffusion occurs in the fast 1D channel along the c-direction, but they also found diffusion pathways in the ab planes. More recent research within the Thio-Lisicon field includes one done by Tarhouchi et al.[38] where $Li_{10}SnP_2S_{12}$ was electrochemically characterised. The tin analogue of $Li_{10}GeP_2S_{12}$, $Li_{10}SnP_2S_{12}$ was studied using Rietveld refinement of the Xray powder diffraction, impedance measurements and cyclic voltammetry of the synthesised structure. More recent studies of thio-lisicons include more detailed investigation of the $Li_{10}GeP_2S_{12}$ structure. One study carried out by Islam and Dawson et al [39] focuses on exploring the nanoscale effects of the

material. In their study they identified through using nanoscale modelling techniques that there are significant nanosizing effects where the conductivity of LGPS increases with a decrease in particle size.

Thio-Lisicons are currently the family of structures that contains the best proposed structure for a solid-state superionic conductor with $Li_{10}GeP_2S_{12}$, having achieved a room temperature conductivity of $1.2x10^{-2}$ S cm^{-1}. Due to this structure leading the field in terms of conductivity, further research into Thio-Lisicon structures and characterisation of their structures, migration pathways and diffusion mechanisms is an area of particular interest due to the plausibility of finding better structures.

Rock Salts

Superionic conductors aren't limited to only NASICONs, Li-NASICONs and LISICONs in structures. Research has also been focused on new superionic conductor materials within the rock salt family of structures. An example of an investigation done into a family of rock-salt related structures includes one done by Amiel et al.[40] where $Ag_4Zr_3S_8$ and $Ag_{3.8}Sn_3S_8$ were both synthesised, their crystal structures characterised using X-ray powder diffraction, and their conductivities measured. Both compounds were found to be isomorphous with 32 Sulphur atoms within a unit cell located at fully occupied positions producing 32 octahedra within the unit cell yielding similar results to the characterization of $Ag_4Hf_3S_8$ done in their previous work [41]. It is worth noting that each octahedron is connected to 12 other octahedra via their common edges. Similar to the hafnium structure the zirconium atoms are located within sulphur octahedra. $Ag_4Zr_3S_8$ was found to have a conductivity of

Ag^+ of $6.4x10^{-5}$ S cm^{-1} at 27°C but at 155°C it was found to be $1.8x10^{-2}$ S cm^{-1}. For $Ag_{3.8}Sn_3S_8$ it was found to have an Ag^+ conductivity at 141°C of $3.6x10^{-3}$ S cm^{-1}.

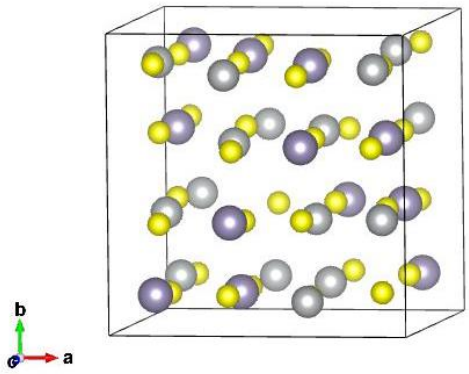

Figure 1.5. $Ag_4Sn_3S_8$ crystal structure along the [001] direction. ICSD code 241493.[42]

The diffusion mechanism of $Ag_4Sn_3S_8$ has also been studied. Hull et al.[42] used computational methods along with impedance spectroscopy methods and powder neutron diffractions to identify the temperature dependence of the crystal structure of $Ag_4Sn_3S_8$ and its Ag^+ diffusion mechanism. MD (Molecular dynamics) simulations were used utilizing interionic potentials with electronic polarization and van der Waals interaction coefficients, with a 2x2x2 supercell containing 128 Ag^+ ions, 96 Sn^{4+} ions and 256 S^{2-} ions. Ionic locations were mapped using experimental data for the initial 300K simulation. Simulations over a total of 20 temperatures in the range of 5K-1000K were performed. The conductivity values they obtained were in agreement with those achieved by Amiel et al [40].

Garnets

Garnet-type structures have also been of interest within the solid-state superionic conductor field. Garnet type structures have a general formula of $A_3B_3C_2O_{12}$ where the A, B and C cations are in a co-ordination of 8, 4 and 6, respectively. The first reported superionic garnet-type structure was done by Thangadurai et al.[43] where $Li_5La_3M_2O_{12}$ (M = Nb, Ta) were synthesised. The characterisation of the compound was done using x-ray powder diffraction and its lithium-ion conductivity was measured using the *a-c* impedance method. They had found that $Li_5La_3Nb_2O_{12}$ and $Li_5La_3Ta_2O_{12}$ both displayed bulk conductivity within the same order of 10^{-6} S cm^{-1} at 25°C. The activation energies for the ionic

conductivity at < 300ºC were identified as 0.43 and 0.56 eV for $Li_5La_3Nb_2O_{12}$ and $Li_5La_3Ta_2O_{12}$, respectively. The tantalum compound was also found to be stable in regard to reactions with molten lithium. Further research of this structure has been carried out by multiple research groups since it was first reported, which includes one done by Murugan et al.[44] where the effect substitution of La with Mg, Ca, Sr, $Sr_{0.5}Ba_{0.5}$ has on the bulk and grain boundary lithium ion conduction in $Li_5La_3Ta_2O_{12}$ and the effect the sintering temperature was studied. Diffusion pathway studies and computational studies of garnet-type structures have also been carried out an example of one where the diffusion pathway was studied via computational methods by Xu et al.[45] In this investigation, they used DFT calculations via the Vienna ab initio simulation package (VASP) to identify the mechanism of Li^+ transport in $Li_{3+x}La_3M_2O_{12}$ (M = Te, Nb, Zr). Their method consisted of using a Projector Augmented Wave (PAW) method with the Generalised Gradient Approximation (GGA) for the exchange-correlation functional. Using supercell structures for the compounds they used the nudged elastic band (NEB) method to find the minimum energy migration pathway for the Li^+ ion. They concluded that there were two distinct pathways a high energy pathway A which has an energy barrier of 0.8 eV and a low energy pathway B which has an energy barrier of 0.26 eV. More recent studies include work carried out by Goddard and Slater et al [46] where they improve on the performance of $La_3Zr_2Li_7O_{12}$ shown in **figure 1.6**. They found an increase in experimental conductivity of $1.24x10^{-4}$ S cm^{-1} at 50ºC, which is 1.5 orders more than previously reported. This was achieved by doping Ce into the Zr site of the structure which resulted in a reduction of the tetragonal distortion and lowering temperature of the tetragonal-cubic phase transition. The characteristics and properties of defining the success of a lithium garnet material has also been studied, with Slater et al [47] where they identified from a series of nince tetragonal garnets, that the octahedral site cation radius was a key factor in the structure's

transition temperature from tetragonal to cubic. Research carried out into identifying key properties which determines the performance of structures will lead to improved developments of the material.

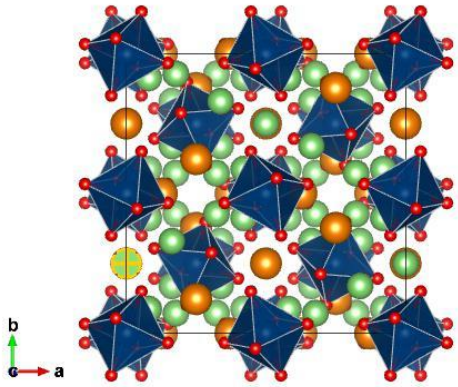

Figure 1.6. $La_3Zr_2\ Li_7O_{12}$ crystal structure. ICSD code 14991.[46] Lanthanum are shown in orange, Zr octahedra are shown in dark blue, lithium in green and oxygen in red.

Garnet-type structured compounds are an area of interest due to the highest bulk conductivity achieved with a garnet-type compound of 10^{-3} S cm^{-1} at room temperature with the $Li_{6.4}La_3Zr_{14}Ta_{0.06}O_{12}$. This value is a considerably high value in the terms of solid-state superionic compounds, further studies into their structures using computational techniques along with experimental techniques and probing possible new structures could help identify a new leader within the solid-state superionic compound field.

Perovskites

Perovskite structured materials come with a wide variety of constituents as well as having anti-perovskite type structures. Due to the variety available within the perovskite family, large amounts of research have been carried out within it to try and identify ideal superionic conductors. For example, of some perovskites studied for their conductive behaviour would include $NaMgF_3$, $KMgF_3$, $KZnF_3$, $KCaF_3$ and $CsPbF_3$ [48–51]. Latie et al.[52] synthesised the perovskite structure $Li_xLn_{1/3}Nb_{1-x}Ti_xO_3$ (Ln = La, Nd) for ionic conductivity determination. For the conductivity measurements, they used an ionically

blocking electrode with an *a.c* method over a wide range of frequencies from a temperature range of 20 to 400°C. It was found that conductivity was higher for $Li_{0.05}La_{0.33}Nb_{0.95}Ti_{0.05}O_3$ and $Li_{0.1}La_{0.33}Nb_{0.9}Ti_{0.1}O_3$ (Lanthanum perovskite compounds) than for $Li_{0.07}Nd_{0.33}Nb_{0.93}Ti_{0.07}O_3$ (Neodymium perovskite compound), that higher conductivity was found using lithium rather than sodium and that in each phase conductivity increases with Li^+ as the amount of charge carriers increase. Belous et al.[53] were the first to carry out a detailed study of lithium lanthanum titanate ($Li_{3x}La_{2/3-x}TiO_3$) in 1987 followed by an investigation into the compound by Inaguma et al.[54] in 1993, where $Li_{0.34}La_{0.5}TiO_{2.94}$ was studied, in particular its structure and conductivity to try and identify the cause of the high ionic conductivity found. The conductivity of the sample at room temperature was measured using a *d.c* polarization method using two Silver (Ag) electrodes and for the lithium conductivity they used an *a.c* impedance method using an impedance analyser over a range of frequencies and at a temperature range of 200 to 700K. Results found that the total conductivity for the perovskite was more than $2x10^{-5}$ S cm^{-1} at room temperature and that the lithium ion conductivity could be split into two contributions, one from bulk crystal and the other from grain boundaries. The bulk conductivity was found to be a high value in the range of 10^{-3} S cm^{-1} and this high conductivity indicated that the perovskite has many equivalent sites for the Li^+ ion to occupy.

An example of computational studies done on perovskites would be one on lithium lanthanum titanate by Youmbi et al.[55] where they investigated the conductivity of hexagonal $Li_{0.5}La_{0.5}TiO_{3-\delta}$ ($0 \leq \delta \geq 0.06$) which was initially reported by Alonso et al.[56] The method used by Youmbi et al was density functional theory (DFT) using the Quantum-ESPRESSO (QE) package codes pw.x and cp.x. The Vanderbilt ultrasoft pseudopotential was used along with Perdew and Wang GGA exchange correlation functional (PW91). Conductivities found for the hexagonal structure was found to be in the order of 10^{-3} S cm^{-1} at room temperature.

More recent studies include research carried out on double-perovskites such as work carried out by Cussen and Goddard et al [57]. They successfully develop a new series of lithium-rich double perovskites $Li_{1.5}La_{1.5}MO_6$ ($M = W^{6+}$, Te^{6+}) where the introduction of tungsten to the structure enables

reversible lithium-ion intercalation below 1V, allowing for an anodic application. They also found that with the substitution of tungsten with tellurium, the structure achieved a redox stability which enabled the application of the material as a solid-state electrolyte.

Perovskite solid-state superionic conductors display a good potential for commercial use. This is due to the high conductivity achieved 10^{-3} S cm^{-1} at room temperature. Although a high conductivity has been achieved with Li^{+} perovskite superionic conductors, Ti-perovskites have the potential for Ti^{4+} reduction by the metallic lithium. As an electrolyte they also have the possible formation of lithium dendrites if used with lithium anodes. Hence resolving these issues is of importance to developing lithium-perovskite solid-state superionic conductors.

Anti-Perovskites

The primary focus of research done with anti-perovskite structures are on lithium rich anti-perovskites (LiRAP) which exhibit the highest conductivities within this class of structures. Some of the initial LiRAPs to be studied were the lithium halide hydrates ($Li_{3-n}(OH)_nCl$ ($0.83 \leq n \leq 2$)) ($Li_{3-n}(OH)_nBr$ ($1 \leq n \leq 2$)) by Schwering et al.[58] In their investigation they aimed to investigate the phase transition and the lithium ionic conductivity by using differential scanning calorimetry (DSC), impedance spectroscopy and solid-state nuclear magnetic resonance spectroscopy. From their investigation they found that the lithium halide hydrates studies could be separated into three separate groups, (I) Compounds with a lithium content with an integer value, which transitions into a cubic phase at room temperature approximately 33ºC. (II) Compounds that are cubic at room temperature and show a slow lower symmetry transition at lower temperatures. (III)$LiCl.H_2O$ which remains tetragonal and does not demonstrate any conductivity. Conductivity of $Li_2(OH)Cl$ and $LiBr.H_2O$ was found to be in the order of 10^{-4} S cm^{-1} and the compound displayed a sharp increase in conductivity when transitioning from the non-cubic to cubic phase. Zhao et al.[7] synthesised a whole new class of anti-perovskites with the general formula Li_3OX (X = Cl, Br). Impedance spectroscopy, differential scanning calorimetry

(DSC) and Xray diffraction (XRD) were all used in characterising the structures. Conductivity measurements were also carried out on the compounds. The compounds were found to have a typical anti-perovskite structure but with slight deviation from the ideal cubic structure. They were also found to be highly hygroscopic and any introduction of moisture to the compounds would significantly reduce the conductivity. Initially they had found the conductivity at room temperature to be relatively low, around 10^{-7} S cm^{-1} but upon annealing in vacuum for 24 hours above 250°C, the conductivity had increased by as much as two orders (10^{-5} S cm^{-1}) at room temperature. The investigation they had carried out opened a large new area for anti-perovskite conductor research.

Doping of lithium rich anti-perovskites has also been studied for example a study done by Li et al.[59] where $Li_2(OH)X$ (X = Cl, Br) was doped with fluoride ions, replacing the -OH- ion. In their investigation they synthesised $Li_2(OH)_{0.9}F_{0.1}Cl$, through using various techniques they found that the doped compound was highly electrochemically stable and had a high lithium conductivity of $1.9x10^{-3}$ S cm^{-1}.

For the diffusion mechanism within LiRAPs, there has been a significant amount of computational research carried out to try and identify the mechanism and to try and understand what effect defects within the structures has on the conductivity. The diffusion pathway of conduction in the $Li_{3-n}O_nX$ (X= Cl, Br) has been studied. Emly et al.[60] where they used first-principle electronic structure calculations with statistical mechanical methods. Density Functional Theory (DFT) was used via the Vienna ab initio software (VASP) to calculate first-principle energies along with projector augmented wave pseudopotentials with generalised gradient approximation (GGA) using the PBE functional. To create disorder within the anti-perovskite lattice structure, cluster expansion implemented in the CASM code was used. The migration barrier calculations were performed using Monte Carlo simulations using the HSE06 hybrid functional. From their investigation they concluded that Li_3OCl and Li_3OBr are metastable relative to decomposition into Li_2O and LiCl/Br, above 2.5 eV relative to metallic lithium anode Li_3OCl becomes susceptible to decomposition into Li_2O and LiCl.

A similar computational study was done by Zhang et al.[61] in which they carried out an ab initio study on stabilities and mechanism of superionic transport (transport mechanism) for the conductivity found in LiRAPs, mainly Li_3OX (X = Cl, Br). Li_3OCl is shown in **figure 1.7**. In their methods, for calculations they used first-principle DFT methods, using the Perdew-Burke-Ernzerhof generalized gradient approximation (GGA), via the software VASP (Vienna ab initio programme). They also used the projector augmented wave pseudopotential method (PAW) with a plane-wave basis set. For the calculations of the lithium ion hopping barriers, the climbing image nudged elastic band method (CINEB) was used. For the analysis done on the lithium-ion transport, *ab* initio molecular dynamics (AIMD) simulations were performed with a 2x2x2 supercell (40 atoms) along with a 2 fs-time step. Whilst using the AIMD simulations in their investigation temperatures of up to 2000K were used to accelerate the ion-hopping process in a fixed cell, hence reducing the time taken for the simulation. They also highlighted the overestimation of melting temperature (Tm) due to the thermal expansion factor not being included. They concluded that their phase diagrams and electronic-structure calculations suggest that Li_3OCl, Li_3OBr and $Li_3OCl_{0.5}Br_{0.5}$ are metastable with Li_3OCl and Li_3OBr showing an energetic instability of -13.9 meV/atom and -25.8 meV/atom respectively towards the formation of Li_2O + LiCl/Br. They also found by studying the density of states (DOS) diagrams and identifying the band gaps, that Li_3OCl/Br are both electrochemically stable, the AIMD simulations demonstrated that perfectly structured anti-perovskites do not show good Li^+ ion conductivity and that vacancies and defects (structural disorder) promote lithium-ion transport (diffusion) due to them reducing the enthalpy barrier for migration of Li^+ ions along the favoured pathways. This study also found that Li^+ ion conductivity for $Li_3OCl_{0.5}Br_{0.5}$ was significantly higher than its Li_3OCl and Li_3OBr counterparts, they acknowledged that further research would be required to identify and explain the cause of the high conductivity found in $Li_3OCl_{0.5}Br_{0.5}$. More recent studies of anti-perovskites includes work done to better understand the effects of doping on the Li_3OCl structure, such as the study carried out by Islam et al [62]. In their study, they found that F^- doped structures have lower conductivities due to high activation barriers, this was attributed to the high binding energies seen with the introduction of F^-. They also found that doping the structure with Mg^{2+}, which was found to be the most favourable dopant, have lower binding energies hence lower activation barriers and higher lithium conductivity.

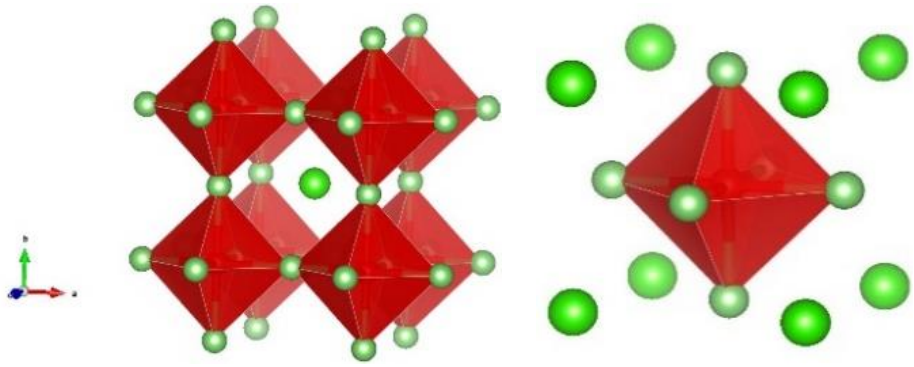

Figure 1.7. Left: Li_3OCl, green atoms are Cl^- atoms, red polyhedra are Li_6O groups. [7]

There has also been development of sodium anti-perovskites such as Na_3OX (X = Cl, Br, I, and BH_4) which was synthesised by Famprikis et al [63]. In their work they used mechanochemical synthesis to synthesise novel compositions which included $Na_3OCl_{0.5}(BH_4)_{0.5}$, $Na_3OBr_{0.5}(BH_4)_{0.5}$, $Na_3OI_{0.5}(BH_4)_{0.5}$, and $Na_3OCl_{0.33}Br_{0.33}(BH_4)_{0.33}$. They also studied the effect of substitution on the structure and the ion transport through various methods including impedance spectroscopy and diffraction. Fujii and Gao et al [64], successfully carried out high-pressure synthesis of a new series of antiperovskites which includes M_3fCh (M = Li, Na; Ch = S, Se, Te). They also carried out a series of first-principles calculations to identify migration barriers for diffusion, and identify the importance of long-range bonding interactions between mobile ions and counter chalcogen ions. The work by Fujii and Gao was completed after our research which was carried out and expanded upon in this thesis in chapter 3. The initial results reported in chapter 3 show good agreement with the development and synthesis of the Li_3FX (X = S, Se) structure.

Lithium rich anti-perovskites display a good potential for use as solid-state superionic conductors due to their stability, low cost, and high conductivities in the order of 10^{-3} S cm^{-1}. As computational methods become more widely used more and more research is being carried out on LiRAPs, due to their structural diversity there is a good potential for further research to be carried out on unknown LiRAP compounds.

1.3. Solid-State Computational Studies

Computational methods are employed in solid-state chemistry in various capacities. Traditionally, computational studies were used in a linear method of either providing supporting data which would lead to coherent sets of data from experimental and computational analysis for a more thorough study, or as an indicative method of identifying potential candidates for synthesis. A more appropriate approach to utilizing computational methods is a more connected approach, where experimental and computational methods can be used in a more synergistic approach where both methods feedback valuable data and information to each other leading to a more fluid investigation of both organic and inorganic chemistries.

In solid-state studies, the range of computational methods employed are extensive. The stability of crystal structures is often predicted and calculated based on the structural arrangement of atoms. Often stability is calculated without entropy being introduced at 0K with the inclusion of methods such as Convex Hull Energy calculations to determine the true stability of a given compound relative to its phase field. Methods which include entropy consist of Molecular Dynamics (MD) calculations, this is often done to study the movement of atoms in 3D space. Often properties of structures are calculated such as bandstructure, bandgap, density of states, and magnetic orderings using various computational methods, these properties are discussed in more detail in Chapter 2 (Methods). Many of these computational methods are mentioned in the previous section such as the *ab*-initio study on the lithium rich anti-perovskite Li_3OX (X = Cl, Br) carried out by Zhang et al [61] or the computational study of the garnet structure $Li_{3+x}La_3M_2O_{12}$ (M = Te, Nb, Zr) by Xu et al [45].

The benefit of utilizing solid-state computational approaches is that it provides a theoretical insight into discovery of new structures, by providing an indication of the viability of materials by stability, giving properties such as conductivity, magnetic properties, atomistic and nano effects within

structures. It also provides support for experimental studies in providing additional information and data which supplements conclusions which can be drawn from experimental data.

1.4. High throughput & Screening of Structures

To accelerate material discovery of organic and inorganic materials particularly within the solid-state field, high-throughput methods of screening structures are being employed with varying step methods from complex machine learning algorithms to less complex and inexpensive methods which rely on chemical intuition such as the bond valence approach.

High throughput calculations to screen for new materials requires certain pre-requisites to function, firstly there is a requirement for thermodynamic and stability calculations or experimental investigation to predict the viability of a given structure, secondly, there must be a storage of these given structures in the form of a database and thirdly there must be an analytical step which correlates a given parameter or 'descriptor' (descriptor being a measurable characteristic of a structure) with another property which is a measurable form of validating the potential for a given structure.

Many high-throughput studies of structures use first principles *ab-initio* calculations as a part of their method of processing many structures. Examples of these studies includes work by Ceder et al [65,66], where first principles calculations are used to direct a search for new potential lithium-ion cathode materials. In their work they validate the accuracy of *ab*-initio calculations in comparison to experimental data. The experimental data in this study for 80 different binary alloys were provided from the CrysMet database [67] and the Pauling File [68]. They successfully demonstrated that high-throughput calculation of a large set of structures using *ab*-initio methods provided accurate results.

Other methods of high-throughput screening of structures consists of data-driven models, an example of this is a study carried out by Sendek et al [69]. where they use a multi-step approach of initially identifying structures from a database of 12,831 structures with high structural and chemical stability and low cost, then they use an ionic conductivity classification model using logistic regression to identify potential solid state electrolyte candidates with fast ionic conductivity based on previous

experimental measures. Machine learning methods are also becoming more frequently used to identify potential solid state superionic conductor candidates such as the work of Ong et al [70], where machine learning is incorporated with various methods to resolve many issues facing high-throughput analysis. Ong aims to do this using the Materials Virtual Lab, where their objective is to discover new materials or optimize existing materials, create computationally inexpensive methods with high accuracy, and accelerate and improve on the accuracy of characterisation using machine learning. Various alternative techniques have also been developed such as MC-EMMA by Collins et al [71]. This method uses a modular approach to arranging crystal structures where modules (layered structured units in two dimensions) are stacked, and a Monte Carlo (MC) driven selection is used to evolve structures. In this work they successfully identified and synthesised two new compositions from the MC-EMMA method, $Y_{0.015}Sr_{0.383}Ca_{0.603}GaO_{2.508}$, and $Y_{0.038}Sr_{0.320}Ca_{0.848}Ga_{0.794}O_{2.416}$. The bond valence method is an example of a high-throughput computational approach which employs chemical intuition in a non-complex method of screening. One example of this would be a study carried out by Xiao et al [72]. where they used the bond valence (BV) approach to study the migration pathway using BVpath code, which uses the BV forcefield approach by Adams [73] of over 1000 structures from the ICSD (Inorganic Crystal Structure Database) [74] to screen structures, where they would then carry out high accuracy DFT calculations for optimizations of the final structures.

These are only a few examples of high-throughput methods being employed currently, but as methods and software advance, more and more methods will become available for screening of these potential structures which ultimately accelerates the discovery process of materials as a whole, and transitions material discovery from a traditional approach to a more modern approach of identifying new potential candidates.

1.5. Thesis Aims & Overview

With computational methods being increasing prevalent in driving the discovery and prediction for crystal structures there are an increasing number of methods for prediction and analysis as mentioned in the previous sections.

For solid-state superionic conductors, the largest barrier for predictive models is identifying metrics or properties which correlate with conductivity. There are no predictive models currently that can accurately predict a conductivity of a structure computationally, based on computationally measurable metrics. Machine learning methods are a more recent development which aim to resolve this problem which are making advances, but also more simplistic methods using chemical intuition are being used.

The objectives of the work which is presented in this thesis is to ultimately provide a novel discovery into identifying new potential candidates as solid-state conductors. This is done with the objective of attempting to resolve the challenges currently faced by solid-state battery technologies as mentioned in the introduction. Whilst identifying a new viable candidate is the primary focus of the work being carried out, there is a focus in trying to develop and improve on current methods by potentially providing new insight into the approaches used in identifying new materials.

In this thesis, the prediction of potential solid-state superionic conductors is carried out by studying various structural families and using primarily convex hull energy calculations to study the phase fields of target structures and identifying their viability as novel and viable structures. The development of a high-throughput method is also done with the objective of identifying if metrics used from the method can indicate and determine potential new candidates.

1.6. References

1 V. Etacheri, R. Marom, R. Elazari, G. Salitra and D. Aurbach, *Energy Environ. Sci.*, 2011, **4**, 3243–3262.

2 B. Dunn, H. Kamath and J.-M. Tarascon, *Science (80-.).*, 2011, **334**, 928–935.

3 F. T. Wagner, B. Lakshmanan and M. F. Mathias, *J. Phys. Chem. Lett.*, 2010, **1**, 2204–2219.

4 P. G. Bruce, S. a. Freunberger, L. J. Hardwick and J.-M. Tarascon, *Nat. Mater.*, 2012, **11**, 19–29.

5 W. Xu, J. Wang, F. Ding, X. Chen, E. Nasybulin, Y. Zhang and J.-G. Zhang, *Energy Environ. Sci.*, 2014, **7**, 513–537.

6 R. Younesi, G. M. Veith, P. Johansson, K. Edstrom and T. Vegge, *Energy Environ. Sci.*, 2015, **8**, 1905–1922.

7 Y. Zhao and L. L. Daemen, *J. Am. Chem. Soc.*, 2012, **134**, 15042–15047.

8 N. Anantharamulu, K. Koteswara Rao, G. Rambabu, B. Vijaya Kumar, V. Radha and M. Vithal, *J. Mater. Sci.*, 2011, **46**, 2821–2837.

9 A. . Robertson, A. . West and A. . Ritchie, *Solid State Ionics*, 1997, **104**, 1–11.

10 H. Aono, N. Imanaka and G. ya Adachi, *Acc. Chem. Res.*, 1994, **27**, 265–270.

11 N. Weber and J. Kummer, *Proc. 21st Annu. Power Sources Conf.*, 1967, **21**, 37–39.

12 M. S. Whittingham and R. A. Huggins, *J. Chem. Phys.*, 1971, **54**, 414–416.

13 H. .-P. Hong, *Mater. Res. Bull.*, 1976, **11**, 173–182.

14 J. B. Goodenough, H. .-P. Hong and J. A. Kafalas, *Mater. Res. Bull.*, 1976, **11**, 203–220.

15 H. Ove and K. Peder, *Acta Chem. Scand.*, 1968, **22**, 1822.

16 R. GORDON, G. MILLER, B. MCENTIRE, E. BECK and J. RASMUSSEN, *Solid State Ionics*, 1981, **3**–**4**, 243–248.

17 U. Von Alpen, M. F. Bell and H. H. Höfer, *Solid State Ionics*, 1981, **3**–**4**, 215–218.

18 J. Alamo, *Solid State Ionics*, 1993, **63**–**65**, 547–561.

19 D. T. Qui, J. J. Capponi, M. Gondrand, M. Saïb, J. C. Joubert and R. D. Shannon, *Solid State Ionics*, 1981, **3**–**4**, 219–222.

20 E. R. Losilla, M. a. G. Aranda, S. Bruque, M. a. París, J. Sanz and A. R. West, *Chem. Mater.*, 1998, **10**, 665–673.

21 K. M. Bui, V. A. Dinh, S. Okada and T. Ohno, *Phys. Chem. Chem. Phys.*, 2016, **18**, 27226–27231.

22 T. Takahashi, K. Kuwabara and M. Shibata, *Solid State Ionics*, 1980, **1**, 163–175.

23 B. E. Taylor, A. D. English and T. Berzins, *Mater. Res. Bull.*, 1977, **12**, 171–181.

24 M. Subramanian, R. Subramanian and A. Clearfield, *Solid State Ionics*, 1986, **18**–**19**, 562–569.

25 J. E. Iglesias and C. Pecharroman, *Solid State Ionics*, 1998, **112**, 309–318.

26 F. Sudreau, D. Petit and J. P. Boilot, *J. Solid State Chem.*, 1989, **83**, 78–90.

27 H. Aono, E. Sugimoto, Y. Sadaoka, N. Imanaka and G. ya Adachi, *Solid State Ionics*, 1990, **40**–**41**, 38–42.

28 D. Petit, P. Colomban, G. Collin and J. P. P. Boilot, *Mater. Res. Bull.*, 1986, **21**, 365–371.

29 M. Catti, A. Comotti and S. Di Blas, *Chem. Mater.*, 2003, **15**, 1628–1632.

30 H. El-Shinawi, A. Regoutz, D. J. Payne, E. J. Cussen and S. A. Corr, *J. Mater. Chem. A*, 2018, **6**, 5296–5303.

31 B. Lang, B. Ziebarth and C. Elsässer, *Chem. Mater.*, 2015, **27**, 5040–5048.

32 R. Kanno, T. Hata, Y. Kawamoto and M. Irie, *Solid State Ionics*, 2000, **130**, 97–104.

33 M. Murayama, N. Sonoyama, A. Yamada and R. Kanno, *Solid State Ionics*, 2004, **170**, 173–180.

34 Z. Liu, F. Huang, J. Yang, B. Wang and J. Sun, *Solid State Ionics*, 2008, **179**, 1714–1716.

35 N. Kamaya, K. Homma, Y. Yamakawa, M. Hirayama, R. Kanno, M. Yonemura, T. Kamiyama, Y. Kato, S. Hama, K. Kawamoto and A. Mitsui, *Nat. Mater.*, 2011, **10**, 682–686.

36 D. A. Weber, A. Senyshyn, K. S. Weldert, S. Wenzel, W. Zhang, R. Kaiser, S. Berendts, J. Janek and W. G. Zeier, *Chem. Mater.*, 2016, **28**, 5905–5915.

37 Y. Mo, S. P. Ong and G. Ceder, *Chem. Mater.*, 2012, **24**, 15–17.

38 I. Tarhouchi, V. Viallet, P. Vinatier and M. Ménétrier, *Solid State Ionics*, 2016, **296**, 18–25.

39 J. A. Dawson and M. S. Islam, *ACS Mater. Lett.*, 2022, **4**, 424–431.

40 O. Amiel, D. C. Frankel and H. Wada, *J. Solid State Chem.*, 1995, **116**, 409–421.

41 O. Amiel and H. Wada, *J. Solid State Chem.*, 1995, **115**, 112–119.

42 S. Hull, P. Berastegui and A. Grippa, *J. Phys. Condens. Matter*, 2005, **17**, 1067–1084.

43 V. Thangadurai, H. Kaack and W. J. F. Weppner, *J. Am. Ceram. Soc.*, 2003, **86**, 437–440.

44 R. Murugan, V. Thangadurai and W. Weppner, *J. Electrochem. Soc.*, 2008, **155**, A90–A101.

45 M. Xu, M. S. Park, J. M. Lee, T. Y. Kim, Y. S. Park and E. Ma, *Phys. Rev. B - Condens. Matter Mater. Phys.*, 2012, **85**, 1–5.

46 B. Dong, S. R. Yeandel, P. Goddard and P. R. Slater, *Chem. Mater.*, 2020, **32**, 215–223.

47 M. P. Stockham, A. Griffiths, B. Dong and P. R. Slater, *Chem. – A Eur. J.*, 2022, **28**, e202103442.

48 M. O'keeffe and J. O. Bovin, *Science*, 1979, **206**, 599–600.

49 N. Andersen, J. Kjems and W. Hayes, *Solid State Ionics*, 1985, **17**, 143–145.

50 A. V. Chadwick, J. H. Strange, G. A. Ranieri and M. Terenzi, *Solid State Ionics*, 1983, **9**–**10**, 555–558.

51 M. Bouznik, Y. . Moskovich and V. N. Voronov, *Chem. Phys. Lett.*, 1976, **37**, 464.

52 L. Latie, G. Villeneuve, D. Conte and G. Le Flem, *J. Solid State Chem.*, 1984, **51**, 293–299.

53 A. G. Belous, G. N. Novitskaya, S. V. Polyanetskaya and Y. I. Gornikov, *Inorg. Mater. (Engl. Transl.); (United States)*, 1987, **23:3**, 470–472.

54 Y. Inaguma, C. Liquan, M. Itoh, T. Nakamura, T. Uchida, H. Ikuta and M. Wakihara, *Solid State Commun.*, 1993, **86**, 689–693.

55 B. Sitamtze Youmbi, S. Zékeng, S. Domngang, F. Calvayrac, A. Bulou, S. Zékeng, S. Domngang, F. Calvayrac and A. Bulou, *Ionics (Kiel).*, 2012, **18**, 371–377.

56 J. A. Alonso, J. Sanz, J. Santamaría, C. León, A. Várez and M. T. Fernández-Díaz, *Angew. Chemie Int. Ed.*, 2000, **39**, 619–621.

57 M. Amores, H. El-Shinawi, I. McClelland, S. R. Yeandel, P. J. Baker, R. I. Smith, H. Y. Playford, P. Goddard, S. A. Corr and E. J. Cussen, *Nat. Commun. 2020 111*, 2020, **11**, 1–12.

58 G. Schwering, A. Hönnerscheid, L. van Wüllen and M. Jansen, *ChemPhysChem*, 2003, **4**, 343–348.

59 Y. Li, W. Zhou, S. Xin, S. Li, J. Zhu, X. Lü, Z. Cui, Q. Jia, J. Zhou, Y. Zhao and J. B. Goodenough, *Angew. Chemie Int. Ed.*, 2016, **55**, 9965–9968.

60 A. Emly, E. Kioupakis and A. Van der Ven, *Chem. Mater.*, 2013, **25**, 4663–4670.

61 Y. Zhang, Y. Zhao and C. Chen, *Phys. Rev. B*, 2013, **87**, 134303.

62 M. J. Clarke, J. A. Dawson, T. J. Mays and M. S. Islam, *ACS Appl. Energy Mater.*, 2021, **4**, 5094–5100.

63 E. Ahiavi, J. A. Dawson, U. Kudu, M. Courty, M. S. Islam, O. Clemens, C. Masquelier and T. Famprikis, *J. Power Sources*, 2020, **471**, 228489.

64 S. Fujii, S. Gao, C. Tassel, T. Zhu, T. Broux, K. Okada, Y. Miyahara, A. Kuwabara and H. Kageyama, *J. Am. Chem. Soc.*, 2021, **143**, 10668–10675.

65 G. Ceder, Y.-M. Chiang, D. R. Sadoway, M. K. Aydinol, Y.-I. Jang and B. Huang, *Nature*, 1998, **392**, 694–696.

66 S. Curtarolo, D. Morgan and G. Ceder, *Calphad*, 2005, **29**, 163–211.

67 P. S. White, J. R. Rodgers and Y. Le Page, *Acta Crystallogr. Sect. B Struct. Sci.*, 2002, **58**, 343–348.

68 P. Villars, K. Cenzual, R. Gladyshevskii and S. Iwata, in *Materials Informatics*, Wiley, 2019, pp. 55–106.

69 A. D. Sendek, Q. Yang, E. D. Cubuk, K.-A. N. Duerloo, Y. Cui and E. J. Reed, *Energy Environ. Sci.*, 2017, **10**, 306–320.

70 S. P. Ong, *Comput. Mater. Sci.*, 2019, **161**, 143–150.

71 C. Collins, M. S. Dyer, M. J. Pitcher, G. F. S. Whitehead, M. Zanella, P. Mandal, J. B. Claridge, G. R. Darling and M. J. Rosseinsky, *Nature. 2017 5467657*, 2017, **546**, 280–284.

72 R. Xiao, H. Li and L. Chen, *J. Mater.*, 2015, **1**, 325–332.

73 S. Adams, *Acta Crystallogr. Sect. B Struct. Sci.*, 2001, **57**, 278–287.

74 A. Belkly, M. Helderman, V. L. Karen and P. Ulkch, *Acta Crystallogr. Sect. B Struct. Sci.*, 2002, **58**, 364–369.

Chapter 2: Methods

This chapter details the theory behind methods being used throughout the research within this thesis. Detailed information on the theory behind computational chemistry and other calculations is given along with information on software and calculations used.

2.1. Geometry Optimization

For a given structure, finding its true ground state is key to determining its stability. To find the true ground state energy, a global minimum energy for a structure must be found when considering the Potential Energy Surface (PES). This is achieved by identifying the point at which the arrangement of atoms within a unit cell, following a computational model, applies a net inter-atomic force of almost 0 on all atoms within the cell. This position on the PES is considered stationary.

Whilst optimizing a structure, the initial structure which is considered a start-point has a high energy and therefore a high point (peak) on the PES. The process of optimization consists of performing steps which modify the atomic arrangement reducing the energy.

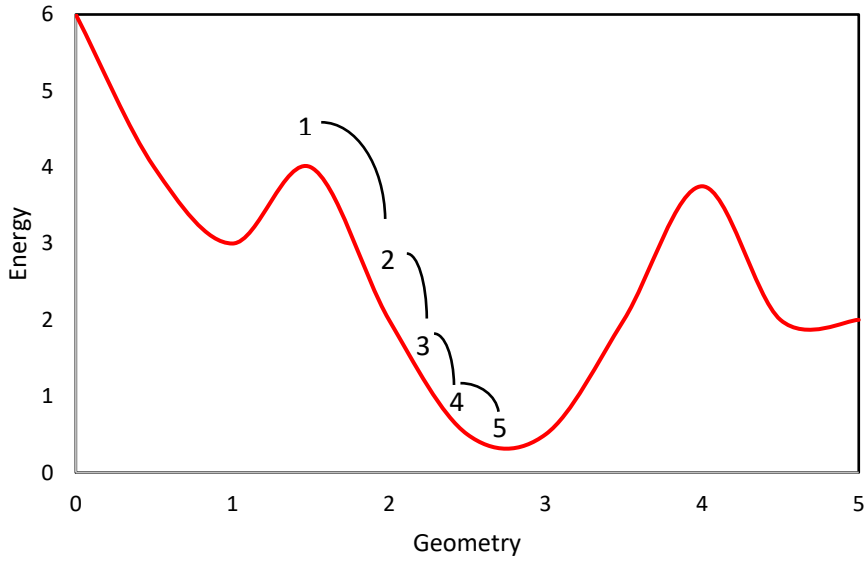

Figure 2.1. Energy Minimization Plot with step process.

In **figure 2.1**, using position 1 as the start-point, optimization steps can be seen which reduces the energy via a negative gradient to reach the minima point 5. Position 1 can also be considered a saddle-

point (highest point in the y direction between two slopes, where gradient is 0, also known as a maxima point) between a local minimum and a global minimum at position 5.

The problem of identifying a local minimum vs a global minimum is dependent on the starting point. Different start points can lead to different minimums therefore, to not exclude the identification of a global minimum when studying a structure, varied start points must be considered. An example of this would be a study of doping a crystal structure, where a displacement and insertion of a new ion into a structure can be done at multiple sites, therefore an optimization of all possible variants must be performed to identify the global minimum energy.

Mathematically, when considering the geometry optimization, a vector **r** can be used to consider the atoms' positions, we can also consider the energy to be a function of the positions $E(\mathbf{r})$. The derivative of the energy relative to the atomic positions $\partial E/\partial \mathbf{r}$, the first derivative, describes the force on each atom. The second derivative matrix of the system ($\partial^2 E/\partial r_i \partial r_j$) which is also known as a Hessian matrix, describes the gradient at point **r**, this leads to distinguishing stationary points which include local and global minimums and maximums.

Multiple mathematical models have been considered and that can be used to create a PES and carry out geometry optimizations. The steepest descent method [1] employs a series of linear sampling of function $F(\mathbf{x})$, ($E(\mathbf{r})$), along the line of steepest-descent direction (**g**) at a number of points along the x+bg line as to find the function $F(\mathbf{x})$'s minimum. By moving point **x** in the steepest-descent direction to where the function $F(\mathbf{x})$ is at a minimum the local minimum can be found. The conjugate gradient method [1] differs to steepest descent method in that the steepest descent method only determines the direction from function $F(\mathbf{x})$ information at a present point (**x**), whereas in the conjugate gradient method, the search direction is determined using function $F(\mathbf{x})$ information from all sampling points along the conjugate gradient path. The conjugate gradient method is considered more efficient than the steepest descent method as it requires less steps to find the local minimum and avoids steps which are back and forth. One other method which is an expensive calculation method is the Newton-Raphson Method [2], this method requires far fewer steps to find the local minimum but is computationally more expensive to carry out. This method uses a sequence of second-order Taylor approximations and quadratics to set the derivatives to 0 when the minimum is found.

The geometry optimization process can be summarised in a flow chart to identify the steps involved in identifying a local minimum for a structure.

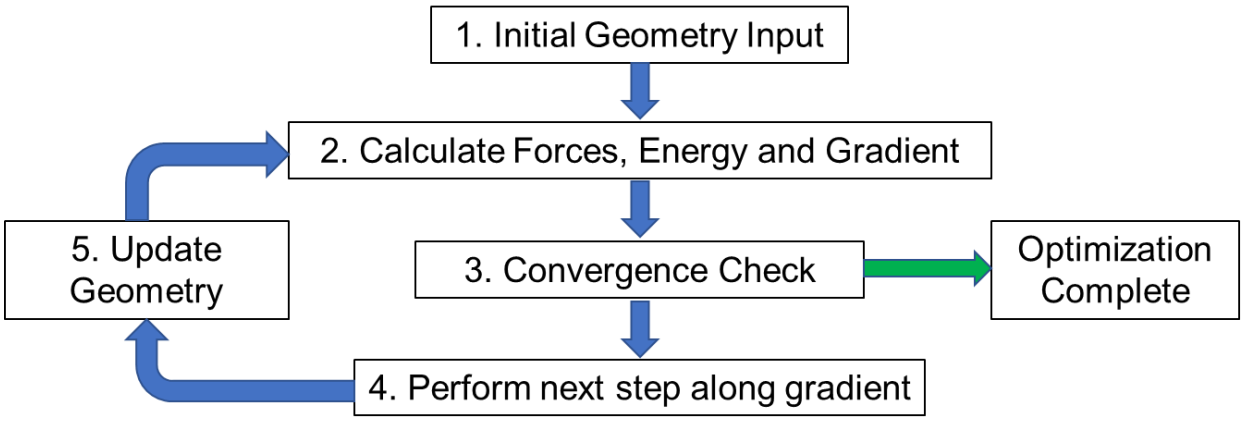

Figure 2.2. Geometry Optimization Flowchart

Figure 2.2 demonstrates a simple step process in a geometry optimization where a geometry input is given, in step 2 all forces are calculated for atoms at a given geometry along with the energy ($E(\mathbf{r})$), and gradient at that given point, ($\partial E/\partial \mathbf{r}$). The convergence check is dependent on the parameters selected for a given optimization, higher thresholds can be applied for higher levels of precision, convergence is met when forces applied to each atom, ($-\partial E/\partial \mathbf{r}$), are below a certain value specified, which is usually measured in eV/Atom. If convergence criteria are not met, the geometry of the structure is updated and a repeat process from step 2 onwards occurs until convergence is met or an iteration or step limit is met.

2.2. Density Functional Theory

Density functional theory is a quantum mechanical method for investigating a system through its electronic structure [3]. It has been used extensively from a wide range of fields such as solid-state chemistry, studying various crystal and solid structures [4], to biology where is is used to study biomolecules and metalloproteins [5,6]. In the studies carried out in this thesis, it has been used extensively to carry out geometry optimization on structures and to calculate magnetic properties, band structures and plot densities of states.

2.2.1. Schrödinger Equation

For a given structure to calculate its total ground state energy, the wavefunction must be studied. This information can be achieved by using the time-independent Schrödinger equation. For a system with a single electron the equation can be expressed as the following:

$$\hat{H}\Psi(\mathbf{r}) = E\Psi(\mathbf{r}) \tag{2.2.1}$$

Equation 2.2.1 is an expression of the time-independent Schrödinger equation and can be expanded to:

$$\left[-\frac{1}{2}\nabla^2 + \upsilon(\boldsymbol{r})\right]\Psi(\mathbf{r}) = E\Psi(\mathbf{r}) \tag{2.2.2}$$

For systems which contain more than 1 electron, a multi-electron system, the equation must further expand to:

$$\left[\sum_{i=1}^{N}\left(-\frac{1}{2}\nabla^2\right) + \sum_{i=1}^{N} V(\boldsymbol{r}_i) + \sum_{i=1}^{N} U(\boldsymbol{r}_i, \boldsymbol{r}_j)\right]\Psi = E\Psi \tag{2.2.3}$$

Where N is the number of electrons, *V* is the potential energy, and U is the electron-electron interaction. The Hamiltonian ($\hat{H}$) can be broken into three segments, a kinetic contribution, T, a potential energy contribution V and a Coulombic contribution U. The kinetic contribution can be expressed as:

$$\hat{T} = -\frac{1}{2}\sum_i \nabla_i^2 \tag{2.2.4}$$

The coulombic electron-electron interaction can be expressed as:

$$\hat{U} = \sum_{i<j} U(\boldsymbol{r_i}, \boldsymbol{r}_j) = \sum_{i<j} \frac{e^2}{4\pi\epsilon_0|\boldsymbol{r}_i - \boldsymbol{r}_j|} \tag{2.2.5}$$

$V(\mathbf{r})$ the potential part is expressed as:

$$V(\boldsymbol{r}) = \sum_{ia} \frac{Z_a}{|\boldsymbol{r_i} - \boldsymbol{R_a}|} \tag{2.2.6}$$

Where r_i is the coordinate of electron *i*, and the charge of the nucleus is Z_a. *U* and *T* for systems interacting with Coulombic interaction are identical, therefore, both *U* and *T* are considered universal operators, the system is dependent on the potential $V(\boldsymbol{r})$.

The issue found in trying to solve the many-body time independent Schrödinger equation is that the computational cost of doing so is large. The expansion of the wavefunction is done by methods such as Hartree-Fock and post-Hartree-Fock methods. In DFT the main variable that is calculated to solve the wavefunction Ψ is the electron density $n(\mathbf{r})$, this is calculated using the following method:

$$n(\boldsymbol{r}) = N \int d^3r_2 \int d^3r_3 \dots \int d^3r_N \Psi^*(\boldsymbol{r}, \boldsymbol{r_2}, \dots, \boldsymbol{r_N})\Psi(\boldsymbol{r}, \boldsymbol{r_2}, \dots, \boldsymbol{r_N}) \quad (2.2.7)$$

Through this method, DFT provides a less computationally expensive solution to solving the wavefunction and equation for a many-body system because it reduces a 3N-dimensional problem with wavefunctions to a 3D problem with the density.

2.2.2. Born-Oppenheimer Approximation

To increase the efficiency of the wavefunction calculation the Born-Oppenheimer Approximation is employed [7]. This approximation identifies the molecular wavefunction Ψ as a result of the nuclear and electronic wavefunction, therefore the Hamiltonian operator is separated to two systems, the electronic and nuclear terms. The treatment of the wavefunction and Hamiltonian operator under the Born-Oppenheimer approximation is a result of the recognition that the mass of the nuclei is much larger than that of the electron, and that motion of the nuclei is significantly slower than that of an electron therefore nuclei are considered stationary. The first process involved with the Born-Oppenheimer approximation is to remove the kinetic energy operator of the nuclei (T_{nuc}) as it is considered stationary, which then leaves the electronic Hamiltonian operator ($\hat{H}_{elec}$). Due to the nuclear positions being stationary and constant, they are considered constant parameters in the equation. This step is also known as the clamped-nuclei approximation.

This first step is demonstrated in the equations below.

$$[T_N + T_e + V_{ee}(\mathbf{r}) + V_{NN}(\mathbf{R}) + V_{eN}(\mathbf{r}, \mathbf{R})]\Psi(\mathbf{r}, \mathbf{R}) = E\Psi(\mathbf{r}, \mathbf{R}) \quad (2.2.8)$$

Equation 2.2.8 gives all operators including nuclear (T_N), electronic kinetic energy (T_e) along with the potential from electron-electron ($V_{ee}(\mathbf{r})$), nuclear-nuclear ($V_{NN}(\mathbf{R})$) and nuclear-electron ($V_{eN}(\mathbf{r}, \mathbf{R})$)interaction. After applying the first step of the approximation the Hamiltonian operator can be expressed in the following way.

$$\hat{\mathrm{H}}_{elec} = T_e(\mathbf{r}) + V_{ee}(\mathbf{r}) + V_{eN}(\mathbf{r}, \mathbf{R}) \quad (2.2.9)$$

The wavefunction Ψ(**r, R**) can also be separated by a quasi-separable ansatz which gives the following form.

$$\Psi(\boldsymbol{r}, \boldsymbol{R}) = \emptyset_N(\boldsymbol{R})\emptyset_{elec}(\boldsymbol{r}, \boldsymbol{R}) \quad (2.2.10)$$

In the clamped-nuclei approximation $V_{NN}(\mathbf{r})$ is neglected due to the nuclei's mass being orders of magnitude above that of an electron. Electrons are approximated to be adiabatically separated from the nuclei for most systems and when combined with the notion of the nuclear parts of the wavefunction being localized spatially when compared to the electron parts of the wavefunction this leads to the neglecting of the $V_{NN}(\mathbf{r})$ term.

$$[T_e + V_{ee}(\mathbf{r}) + V_{eN}(\mathbf{r},\mathbf{R})]\emptyset_{elec}(\mathbf{r},\mathbf{R}) = \hat{\mathrm{H}}_{elec}\emptyset_{elec}(\mathbf{r},\mathbf{R}) = E_{elec}\emptyset_{elec}(\mathbf{r},\mathbf{R}) \quad (2.2.11)$$

$$\hat{\mathrm{H}}_{elec}\emptyset_{elec}(\mathbf{r},\mathbf{R}) = \left[-\frac{1}{2}\sum_i \nabla_i^2 - \sum_{iJ}\frac{Z_J}{r_{Ji}} + \sum_{i>j}\frac{1}{r_{ij}}\right]\emptyset_{elec}(\mathbf{r},\mathbf{R}) = E_{elec}\emptyset_{elec}(\mathbf{r},\mathbf{R}) \quad (2.2.12)$$

Equation 2.2.12 shows the electronic Schrödinger equation under the clamped-nuclei approximation. Once the electronic energy eigenvalue (E_{elec}) is found, the second step of the approximation can be carried out where the nuclear kinetic energy (T_N) can be re-introduced.

$$\hat{\mathrm{H}}_N\emptyset_N(\mathbf{R}) = \left[-\sum_J \frac{1}{2M_J}\nabla_J^2 + E_{elec}(\boldsymbol{R}) + \sum_{J>I}\frac{Z_J Z_I}{R_{JI}}\right]\emptyset_N(\mathbf{R}) = E_{Total}\emptyset_N(\mathbf{R}) \quad (2.2.13)$$

Separating the terms to be electronic and nuclear allows for the wavefunction to be calculated for initially, the electronic wavefunction ($\emptyset_{elec}$) using stationary nuclei and then from the electronic energy eigenvalue enables the inclusion of nuclear motion and therefore the calculation of the nuclear wavefunction ($\emptyset_N$). This in turn allows for the calculation of the E_{Total} eigenvalue which is the total energy of the system.

2.2.3. Hohenberg-Kohn Theorem

The Hohenberg-Kohn theorems come in two parts and relates to any system which has electrons which move in the presence of an external potential $v_{ext}(\boldsymbol{r})$. [8]

Theorem 1 tells us:

The external potential $v_{ext}(\boldsymbol{r})$, and hence the total energy, is a unique function of the electron density $n(\boldsymbol{r})$.

In the first theorem the energy functional can be expressed in external potential terms $v(\boldsymbol{r})$, in the following way:

$$\mathrm{E}[n(\boldsymbol{r})] = \int n(\boldsymbol{r}) v_{ext}(\boldsymbol{r}) d\boldsymbol{r} + F[n(\boldsymbol{r})] \tag{2.2.14}$$

Where $\mathrm{E}[n(\boldsymbol{r})]$ is the energy functional, and $F[n(\boldsymbol{r})]$ is an unknown, universal function of electron density $n(\boldsymbol{r})$.

The second Hohenberg-Kohn theorem states:

The ground state energy can be obtained variationally: the density that minimises the total energy is the exact ground state electron density.

Therefore, when applied to equation (2.2.14), the energy functional reaches its minimum at the ground state energy of *N* electrons in the potential $v(\boldsymbol{r})$. Therefore, the minimal value of the energy functional is the ground state energy of the system $E_{(v,N)}[n]$.

2.2.4. Kohn-Sham Equations

As described in the Hohenberg-Kohn theorem the ground state energy of a system is given in equation (2.2.14), although the density functional $F[n(\boldsymbol{r})]$ is unknown, therefore, non-classical interactions, kinetic energy and Coulombic interaction contributions cannot be ascertained without more systematic modelling.

One of the earliest models for resolving the many-electron problem was the Thomas-Fermi model [9]. In this model, the electron density $n(\boldsymbol{r})$ is used as the central variable rather than the wavefunction. The total energy of the system in the Thomas-Fermi model is written as a functional $E^{TF}[n(\boldsymbol{r})]$. One of the significant problems with the Thomas-Fermi model is that the kinetic energy and exchange energy has significant error. The Kohn-Sham equations [10] were later introduced to resolve these errors providing a more accurate model.

The Kohn-Sham equation is a one electron Schrödinger (like) equation, of a Kohn-Sham system of non-interacting particles. These non-interacting particles give the same density as a system of

interacting particles. In this equation the external potential is given by an artificial potential known as the Kohn-Sham potential in which the non-interacting particles move.

In this model the energy functional can be expressed as:

$$\mathrm{E}[n(\boldsymbol{r})] = T_s[n(\boldsymbol{r})] + \int n(\boldsymbol{r}) v_{ext}(\boldsymbol{r}) d\boldsymbol{r} + E_{XC}[n(\boldsymbol{r})] + E_H[n(\boldsymbol{r})] \tag{2.2.15}$$

Where $T_s[n(\boldsymbol{r})]$ is the kinetic energy (Kohn-Sham kinetic energy) for electrons in the system where there are no electron-electron interactions, and the density of the Kohn-Sham system is the same as the real system. $T_s[n(\boldsymbol{r})]$ is expressed in Kohn-Sham orbital terms:

$$T_s[n(\boldsymbol{r})] = \sum_{i=1}^{N} \int d\boldsymbol{r} \varphi_i^*(\boldsymbol{r}) \left(-\frac{1}{2}\nabla^2\right) \varphi_i(\boldsymbol{r}) \tag{2.2.16}$$

For equation (2.2.15) $E_H[n(\boldsymbol{r})]$ is the Coulomb energy contribution. $E_{XC}[n(\boldsymbol{r})]$ is the exchange-correlation energy functional.

The exchange-correlation functional $E_{XC}[n(\boldsymbol{r})]$ is the energy difference between the true density functional $F[n(\boldsymbol{r})]$ and the remaining terms when using the Kohn-Sham model. The exchange-correlation energy accounts for the missing interactions which are not considered in the previous Kohn-Sham terms. These interactions include electron interactions, both exchange and correlation, and difference in kinetic energy of the Kohn-Sham kinetic energy $T_s[n(\boldsymbol{r})]$, and the kinetic energy of the real system $T_e[n(\boldsymbol{r})]$. Due to the form of $F[n(\boldsymbol{r})]$ being unknown, approximations must be used when considering the exchange-correlation functional $E_{XC}[n(\boldsymbol{r})]$.

Choosing the density of non-interacting electrons, to be the same as that of interacting electrons at the ground state, the Kohn-Sham equation is introduced and can be expressed as:

$$\left[\frac{1}{2}\nabla^2 + V_{ext}(\boldsymbol{r}) + V_{XC}(\boldsymbol{r}) + V_H(\boldsymbol{r})\right] \psi_i(\boldsymbol{r}) = \varepsilon_i \psi_i(\boldsymbol{r}) \tag{2.2.17}$$

ψ_i is the Kohn-Sham orbital for non-interacting electrons, with ε_i is the orbital energy of the corresponding Kohn-Sham orbital. $V_{ext}(\boldsymbol{r})$ is the external potential which is acting upon the interacting system. It describes the interaction between electron and atomic nuclei. $V_{XC}(\boldsymbol{r})$ is the exchange-correlation energy functional derivative which describes the missing interactions which are neglected as mentioned above, which contains non-classical electrostatic interaction energy and kinetic energy difference between interacting and non-interacting systems. $V_{XC}(\boldsymbol{r})$ can be expressed as:

$$V_{XC}(\boldsymbol{r}) = \frac{\delta E_{XC}[n(\boldsymbol{r})]}{\delta \boldsymbol{n}(\boldsymbol{r})} \tag{2.2.18}$$

And $V_H(\boldsymbol{r})$ is the Hartree potential which describes the Coulombic repulsion between an electron and electron density:

$$V_H(\boldsymbol{r}) = e^2 \int \frac{n(r')}{|\boldsymbol{r}-\boldsymbol{r}'|} d\boldsymbol{r}' \tag{2.2.19}$$

The Kohn-Sham equations can be solved in a step process as they are considered self-consistent, the following sequential steps are:

Step 1: Find an appropriate electron density, so that $n_{KS}(\boldsymbol{r}) = n_0(\boldsymbol{r})$

Step 2: Solve the KS equations using the $n_{KS}(\boldsymbol{r})$ to identify the KS states $\psi_i(\boldsymbol{r})$

Step 3: Calculate electron density $n_1(\boldsymbol{r})$ using KS States $\psi_i(\boldsymbol{r})$

$$n(\boldsymbol{r}) = 2\sum_i^{N/2} |\psi_i(\boldsymbol{r})|^2 \tag{2.2.20}$$

Step 4: Electron density $n(\boldsymbol{r})$, is compared to KS electron density $n_{KS}(\boldsymbol{r})$ to identify difference between both values. If a significant variance is found between both, then a new KS electron density is selected and the process is repeated until both densities are similar within a given tolerance. If both values are similar within a given tolerance of each-other, then the total energy of the system is calculated.

2.2.5. Exchange Correlation Functionals

The exchange-correlation functional previously discussed $E_{XC}(\boldsymbol{r})$ is most commonly expressed as the following:

$$E_{XC}[n] = \int n(\boldsymbol{r}) \epsilon_{XC}[n(\boldsymbol{r})] d\boldsymbol{r} \tag{2.2.21}$$

Where $n(\boldsymbol{r})$ is the electron density, and $\epsilon_{XC}[n(\boldsymbol{r})]$ is the exchange-correlation energy per electron. Assuming that the exchange-correlation energy is local:

$$\epsilon_{XC}(\boldsymbol{r}) = \epsilon_{XC}^{hom}[n(\boldsymbol{r})] \tag{2.2.22}$$

$V_{XC}(\boldsymbol{r})$ can then be expressed in the following way:

$$V_{XC}(\boldsymbol{r}) = \frac{\delta E_{XC}[n(\boldsymbol{r})]}{\delta \boldsymbol{n}(\boldsymbol{r})} = \frac{\delta[n(\boldsymbol{r})\epsilon_{XC}(\boldsymbol{r})]}{\delta \boldsymbol{n}(\boldsymbol{r})} \tag{2.2.23}$$

This expression is used for the local density approximation (LDA). The LDA assumes that *the exchange-correlation energy at a given position in space,* ***r,*** *is equal to the exchange-correlation energy of a uniform electron gas that has the same density at that given position,* ***r****.*

$$E_{XC}^{LDA}[n] = E_{X}^{LDA}[n] + E_{C}^{LDA}[n] \tag{2.24}$$

The exchange-correlation energy can be split into the exchange and correlation parts separately and can be combined linearly.

Inhomogeneities in the electron density around the given position, **r**, are disregarded by LDA, hence the LDA disregards the corrections to the exchange-correlation energy. This would make one consider LDA to be unsuccessful, but due to the LDA following the sum-rule, where one electron is excluded in the immediate area surrounding position **r**, which means LDA provides successful results. LDA is also known to overbind, therefore another exchange-correlation functional should be considered.

The generalised gradient approximation (GGA) [11] is an alternative approximation which is an improvement in accuracy over LDA. GGA includes the inhomogeneities by including electron density gradient and therefore can be written as:

$$E_{XC}^{GGA}[n] = \int n(\boldsymbol{r})\epsilon_{XC}^{hom}[n(\boldsymbol{r})]F_{XC}[n(\boldsymbol{r}), \nabla n(\boldsymbol{r})]d\boldsymbol{r} \tag{2.25}$$

Where $F_{XC}[n(\boldsymbol{r}), \nabla n(\boldsymbol{r})]$ is the factor in which enhances the accuracy. Unlike LDA where it has a unique form, GGA has many variants such as PBE [11], PW91[12] and RPBE [13]. GGA is more successful than LDA in that it reduces the overbinding experienced by using LDA and is significantly more successful when used on molecules. Overbinding results in underpredicted lattice parameters and an overestimation of the stability and resulting energies calculated for a given structure hence reducing this effect leads to more accurate results.

Meta-GGAs (MGGA) e.g. MGGA-MS [14], revTPSS [15], GMTKN30 [16], are also used as functionals due to their higher accuracy. They improve accuracy by implementing the Laplacian (second derivative) of the electron density $\nabla^2 n(\boldsymbol{r})$. In practice the non-interacting kinetic energy density is used as input for the functional.

$$E_{XC}^{MGGA}[n] = \int d\boldsymbol{r}[n(\boldsymbol{r})]\epsilon_{XC}([n(\boldsymbol{r})], \nabla[n(\boldsymbol{r})], \tau_s(\boldsymbol{r})) \quad (2.2.26)$$

Where $\tau_s(\boldsymbol{r})$ is the non-interacting kinetic energy density which is expressed as:

$$\tau_s(\boldsymbol{r}) = \frac{1}{2}\sum_{ik}|\nabla\phi_{ik}(\boldsymbol{r})|^2 \quad (2.2.27)$$

The implementation of this functional is computationally expensive.

2.2.6. DFT+U

Transition metals have strong on-site Coulombic interaction of localised electrons. LDA and GGA do not describe these interactions very well. Strong d and f electron interactions lead to both LDA and GGA underestimating the band gap for materials with strong localised electrons, this is known as the 'band-gap problem'.

To resolve this DFT+U is introduced. U (on site Coulomb interaction) and J (on site exchange) parameters are used to describe the strength of on-site interactions. The additional terms can be introduced into calculations by different methods. There are two main methods of doing so, firstly, Liechtenstein method, which was introduced by Liechtenstein et al [17] where U and J are introduced independently as corrections into the calculations, and secondly, the Dudarev method, developed by Anasimov et al [18], where an effective U_{Eff} = U – J, describes the Coulomb interaction.

The Dudarev method is implemented in the GPAW projector-augmented wave method and can be expressed as:

$$E_{DFT+U} = E_{DFT} + \sum_a \frac{U_{eff}}{2} Tr(p^a - p^a\, p^a) \quad (2.2.28)$$

Where p^a is the atomic orbital occupation matrix.

2.2.7. Basis Sets

A basis set can be used to describe an electronic wavefunction using the following equation:

$$\psi_i = \sum_j c_{ij}\varphi_i \tag{2.2.29}$$

Where the wavefunction, ψ_i, is the product of, c_{ij}, which are the expansion coefficients and φ_i which is the basis function.

There are multiple types of basis sets which include Slater Type Orbitals (STO) [19], Gaussian Type Orbitals (GTO) [20], and Plane Wave Basis set (PWB) [21]. The wavefunction is represented as a vector corresponding to the coefficients of the basis functions in a linear expansion. Commonly basis sets composed of atomic orbitals are centred around atomic nuclei in a molecule and they decay exponentially away from the nucleus.

Slater type orbitals (STOs) are functions used as atomic orbitals in a linear combination of atomic orbitals (LCAO), molecular orbital method. STOs have the following radial part:

$$R(r) = Nr^{n-1}e^{-\varsigma r} \tag{2.2.30}$$

Where n is the principle quantum number, *N* is a normalising constant, *r* is the distance of the electron from the nucleus, and ς is a constant of the effective charge of the nucleus, historically determined by Slater rules [19].

Gaussian type orbitals (GTOs) are another form of function used as atomic orbitals in a linear combination of atomic orbitals (LCAO). GTOs were an improvement on STOs in terms of accurately describing molecules.

$$G_{nlm}(r,\theta,\psi) = N_n r^{n-1}e^{-\varsigma r^2}Y_l^m(\theta,\psi) \tag{2.2.31}$$

Where $Y_l^m(\theta,\psi)$ are the angular part (spherical harmonic) with *l* and *m* being the angular momentum and magnetic quantum numbers, r,θ,ψ are the spherical co-ordinates.

For periodic systems, plane wave basis sets are used. The periodic system can be shown as two parts, a plane wave and periodic part.

$$\psi_k(\boldsymbol{r}) = U_k(\boldsymbol{r})e^{i\boldsymbol{k}.\boldsymbol{r}} \tag{2.2.32}$$

Wave vector $\boldsymbol{k}$ is constricted to the Brillouin zone. The periodicity of the lattice can be expressed as:

$$U_k(\boldsymbol{r}) = U_k(\boldsymbol{r} + \boldsymbol{R}) \tag{2.2.33}$$

Where $\boldsymbol{R}$ is a lattice vector.

Therefore, within a periodic cell, a plane wave basis set can be used to study the wavefunction. This can be expressed as:

$$U_k(\boldsymbol{r}) = \sum_G C_{k+G} e^{i\boldsymbol{G}.\boldsymbol{r}} \tag{2.2.34}$$

Where $\boldsymbol{G}$ are reciprocal lattice vectors, C_k is the plane wave coefficients. From both equation 2.2.29 and 2.2.30, the Kohn-Sham orbitals is expressed as the infinite sum of the plane waves:

$$\psi_k(\boldsymbol{r}) = \sum_G C_{k+\boldsymbol{G}} e^{i(k+\boldsymbol{G}).\boldsymbol{r}} \tag{2.2.35}$$

The sum over $\boldsymbol{G}$ vectors is infinite, but computationally a limit must be set so that the sum over $\boldsymbol{G}$ vectors is finite. This is done by applying a kinetic energy cut-off (plane wave kinetic energy cut-off). This cut-off is expressed as:

$$E_{cut} \geq \frac{1}{2}|\boldsymbol{k} + \boldsymbol{G}|^2 \tag{2.2.36}$$

Plane-wave basis sets are beneficial due to the ability to increase accuracy of calculations by increasing the energy cut-off. All points in the cell (space) are treated equally with use of waves, therefore can be used for non-periodic systems, only if a suitable periodic supercell is used, which enables the study of larger and much more complex systems to a higher degree of accuracy.

As previously discussed, the convergence can be modified to be achieved quicker to a lower accuracy or longer to a higher degree of accuracy. Convergence can also change based on the k-point sampling used in the calculations. There are a number of k-point sampling methods such as the Monkhorst-Pack

k-point sampling method [22] and Gaussian smearing to smear over the Fermi level which leads to more k-points being effectively on the Fermi surface.

2.2.8. Pseudopotentials

Kohn Sham wavefunctions require a large amount of plane waves to accurately describe electronic wavefunctions. The rapid oscillation of wavefunctions of the electrons in the core region due to the strong ionic potential leads to an expensive computational cost of calculating the wavefunctions. In **figure 3.** the rapid oscillations of wavefunctions can be seen on the Ψ^{AE} plot at low distances (r). The oscillations occur as they maintain the required orthogonality of the valence electrons relative to the core electrons. A pseudopotential can be used to resolve this issue and therefore reduce the computational cost required to calculate the Kohn-sham equations.

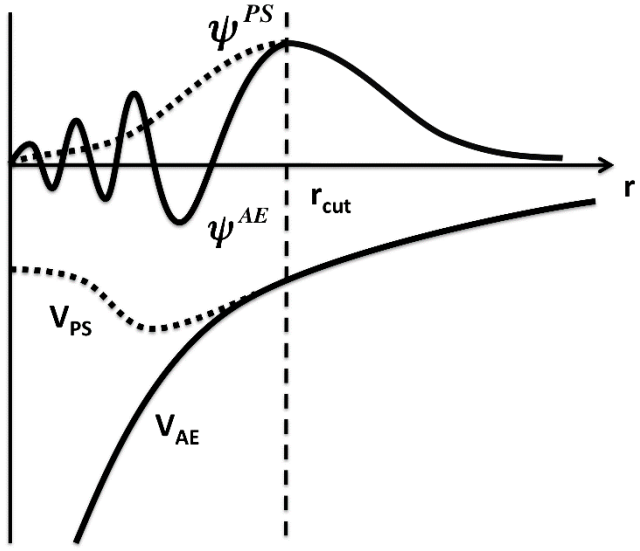

Figure 2.3. Comparison of a wavefunction in the Coulombic potential of the nucleus and the pseudopotential, with agreement seen above cut-off ($\mathbf{r_{cut}}$). [1]

For an atom in a system, a pseudopotential [23] is used to substitute the complex mobility/motion of core electrons and the nucleus with a potential. The Schrödinger equation's Coulombic potential term is replaced with this effective pseudopotential. All core states within the atomic electronic potential are removed and thus the valence electrons are described by pseudo-wavefunctions. The pseudo-wavefunctions can be described with fewer Fourier modes, i.e. plane waves, which increases the

efficiency of the calculation. One can consider the electrons for a given pseudopotential to be treated such that the core electrons are considered 'frozen' with the nucleus, as a non-polarizable, unvarying core, and the valence electrons can be treated explicitly for a calculation.

Pseudopotentials require that pseudo, and all electron valence eigenstates have the same energies and density above a given cut-off radius ($\mathbf{r_{cut}}$). **Figure 2.3** demonstrates the agreement seen in pseudopotential wavefunction and Coulombic wavefunction above a given cut-off value ($\mathbf{r_{cut}}$). Larger cut-offs lead to what is considered 'softer' pseudopotentials, this leads to a faster rate of convergence but at the cost of a decrease in accuracy.

The augmented wave method is an approach taken as an aim to resolve this, where the system is split into two sections, firstly the core section in which the wavefunctions are atomic-like basis sets (functions) and secondly the valence section where plane waves are used.

In this thesis the projector augmented wave method (PAW) [24] is used throughout. The projector augmented wave method utilizes components from both the augmented wave method and pseudopotential methods. PAW transforms the rapidly oscillating wavefunctions which are near the core states into smooth wavefunctions. This ensures that the calculations are less computationally expensive and are more efficient.

2.3. Convex Hull Energy

Convex hull calculations are used extensively throughout the research presented in this report. The purpose of a convex hull calculation and by that determining the convex hull energy of a given structure is to identify the true stability of a compound relative to all competing phases formed from the same set of elements. When considering a convex hull geometrically, for a set of given points in space, the convex hull is the smallest convex set that contains all points. This is also known as a convex closure.

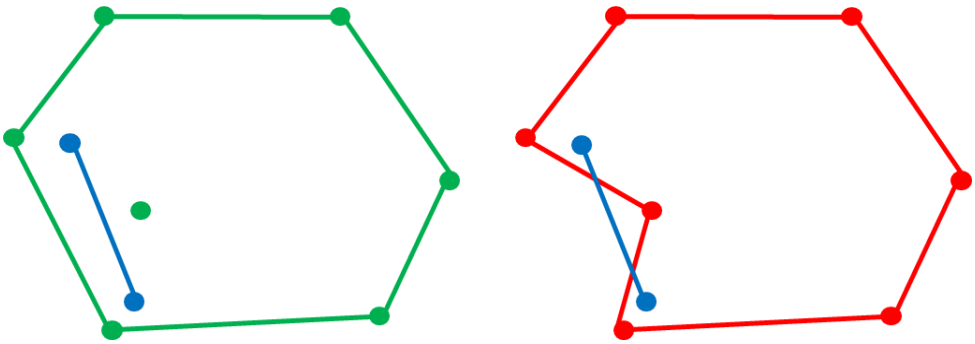

Figure 2.4. Geometric Convex Hull, left: true convex hull containing all points and cross points within polygon, right: false convex hull polygon contains points but not cross lines.

Figure 2.4 demonstrates the convex hull closure, the polygon on the left contains all points within the space including cross lines between two given points in space, the blue cross line shows this. On the right, the polygon does not contain all points and their cross lines, therefore all points are not contained within the polygon and cannot be defined as a convex closure, the blue cross line is not entirely within the polygon on the right.

This concept can be related to the stability of a structure when considering a convex hull in 3D space, similarly the convex hull in 3D space is classified as a convex closure, when the lowest points in 3D space form the convex 'hull', therefore the convex hull energy is the energy difference between the structure being analysed and the energy of the combination of phases lying on the convex hull that give the same species and stoichiometries as the target phase. This effectively represents a decomposition energy.

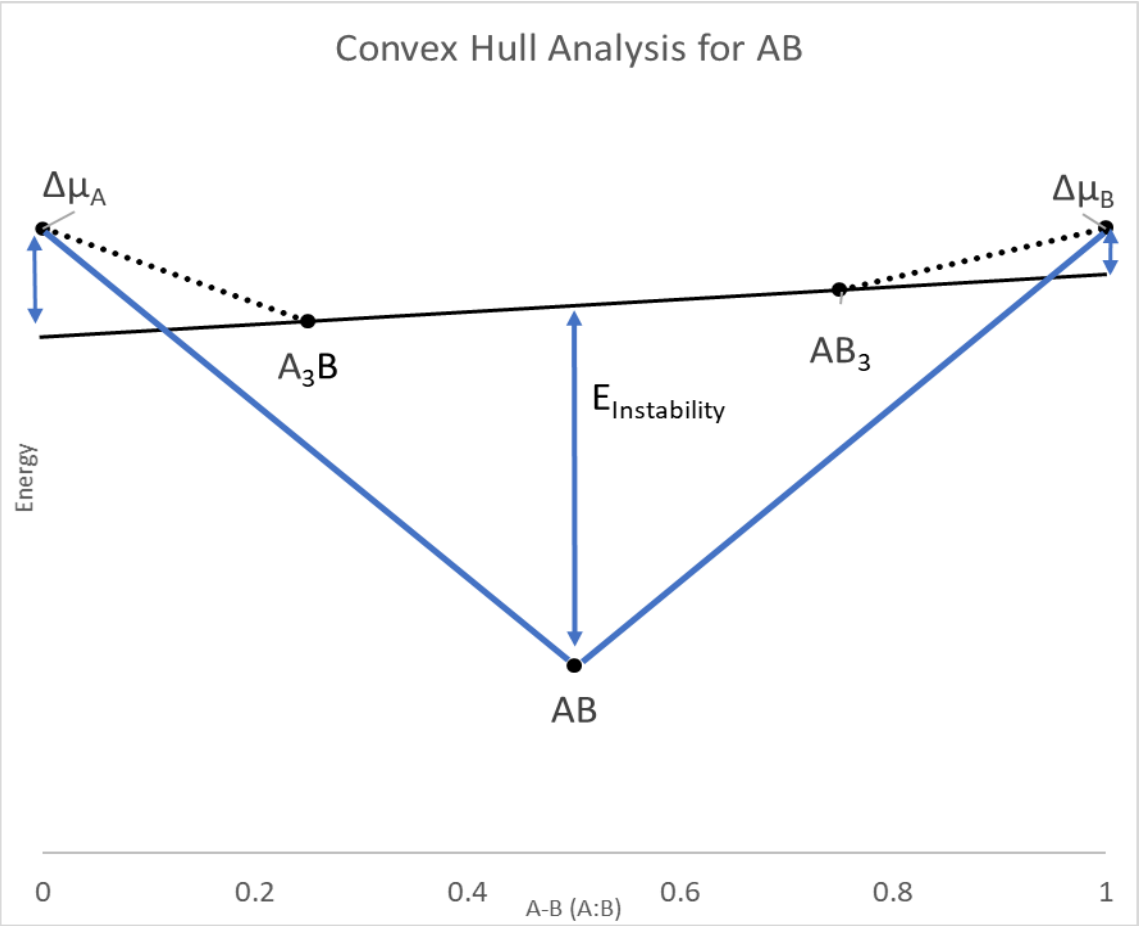

Figure 2.5. Convex Hull construct for a binary example compound AB. Formation energy for compounds calculated relative to elemental chemical potentials $\Delta\mu_A$ and $\Delta\mu_B$.

For a given structure the convex hull energy can also be demonstrated in a 2D diagram. **Figure 2.5** demonstrates a convex hull for a binary compound AB. For the AB compound, both AB_3 and A_3B are competing phases. All compounds formation energies are calculated relative to their elemental chemical potentials for the individual elements A ($\Delta\mu_A$) and B ($\Delta\mu_B$). The potentials are DFT calculated total ground state energies for each component. This can be expressed as:

$$E_{Formation} = E_{Compound} - \sum_{i=1}^{2} C_i \mu_i \qquad (2.3.1)$$

Where $E_{Compound}$ is the total ground state energy calculated for the structure being studied. In the figure all compounds AB, AB_3 and A_3B are all stable relative to the elemental chemical potentials, that is, $E_{Formation}$ are all negative. Thermodynamically, these compounds are considered stable, although when considering each compound's competing phases only AB is truly considered stable. AB in this situation becomes the lowest point of the 2D energetic system (the most negative) therefore to form a convex closure, AB forms the convex hull and has the convex hull energy of 0meV/atom. All

compounds which are above the convex hull are considered metastable or unstable, and their convex hull energy is positive, +meV/atom. A_2B would be considered unstable relative to AB-A and AB_3 would be unstable relative to AB-B. The decomposition products of a phase can be calculated by removing the target phase from the phase space and identifying the convex hull compounds, for example, for AB_3, when removing AB_3 from the phase space, the convex hull is formed by AB and B, the instability of AB_3 can then be calculated as the energy difference between the formation of AB_3 compared to AB-B. Convex hull calculations are used as it gives an overview of an entire phase-field for a given compound therefore a more efficient approach to studying the relative stability of the compound whilst ensuring all competing phases are considered.

2.4. Bond Valence Sum Mismatch Mapping

Bond Valence Sum Mismatch mapping has been developed and studied extensively, being employed in many studies as a method of analysing the mobile ion migration pathway (diffusion pathway) of conductive compounds. It provides a computationally inexpensive method of analysing mobile ion migration pathways when compared to the computationally expensive nudged elastic band method and molecular dynamics. It can be used as an alternative or to supplement NEB and MD calculations for modelling pathways. The theory behind the mapping stems from the bond valence model. For a given atom its' valence (V) is the sum of individual bond valences (v_i) surrounding the atom.

$$V = \sum v_i \tag{2.4.1}$$

For an individual bond valence (v_i), its value can be calculated from observable bond length combined with a bond valence parameter.

$$v_i = exp\left(\frac{R_0 - R_i}{b}\right) \tag{2.4.2}$$

Where R_0 is the ideal bond length for a given element when it has the bond valence of 1, R_i is the actual bond length, and b is the bond valence parameter. The same process can be applied for a diatomic bond between a cation and anion. For a mobile cation A and counter-ion X, the bond valence (S_{A-X}) is identified by:

$$S_{A-X} = exp\left(\frac{R_0 - R_{A-X}}{b}\right) \tag{2.4.3}$$

For the bond valence sum mapping, the "accessible" mobile ion (A) sites in a local structure model being identifiable via employing empirical relationships between bond length *R* between the mobile-ion and counter-ion, and the bond-valence S_{A-X} as given in equation 2.4.3.

The mobile sites are identified as sites where the mismatch:

$$|\Delta V(A)| = |\sum_X S_{A-X} - V_{id}(A)| + \sum_X P_{A-X} \quad (2.4.4)$$

at the bond valence (S_{A-X}) summed over all adjacent counter-ions X approaches the ideal valence V_{id} (A). The penalty term P_{A-X}, is included to disfavour sites which have strong unsymmetrical co-ordination and sites which are too close to other non-mobile ion within the structure. To summarise Bond Valence (BV) analysis allows for identification of charge carriers (mobile ions), transport pathways and transport mechanism via comparing BV mismatch barriers, from combining crystallographic information with force-field simulations.

When considering the bond valence S_{A-X}, the bond valence parameter b is an important factor to the outcome given in equation 2.4.3 and 2.4.4. Commonly a value of 0.37 is used as a constant value for all bond valence calculations which was used by Brese and O'keeffe [25], in which they used the 0.37 parameter to calculate bond valence values for cation and anion combinations. More recently a more intuitive approach can be employed as use for the bond valence parameter. SoftBV parameters developed by Adams et al [26], improved on the original bond valence parameter of 0.37. The initial bond valence parameter relied on the principle that the bond valence for an atom is fully determined by the interactions in the atoms first co-ordination shell. The problem found with this concept is that for a given co-ordination type, with a fixed bond valence parameter (b) of 0.37, the pseudopotential

seen in **figure 2.6** below becomes identical for all monovalent cations, regardless of the type of bonding, or polarizability of interactions which leads to less accurate descriptions.

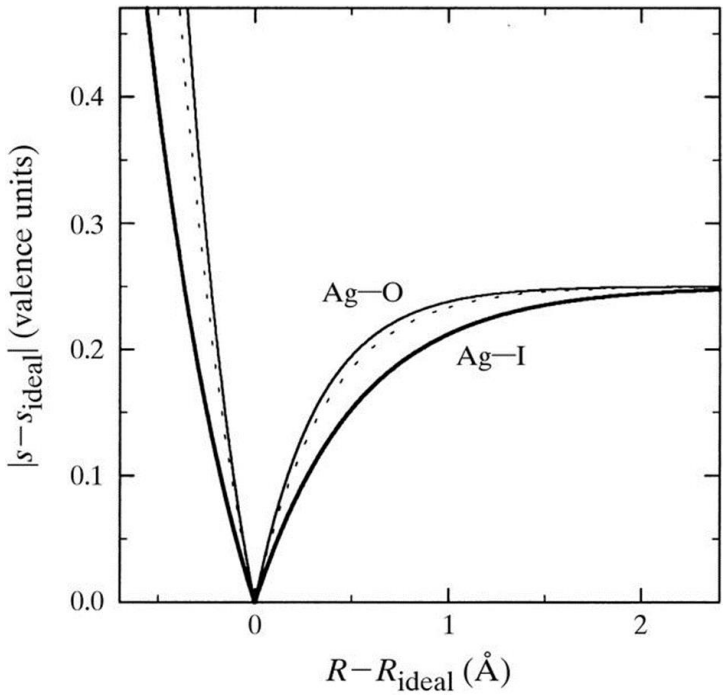

Figure 2.6. Pseudopotential representation of the correlation between bond-length R and bond valence s for both Ag-O and Ag-I. The dashed line represents the potential for both Ag-O and Ag-I using the bond valence parameter (*b*) of 0.37. S.Adams 2001. [26]

Figure 2.6 is a pseudopotential representation of the correlation between bond length and bond valence. The solid lines representing pseudopotential plots for Ag-O and Ag-I using the SoftBV parameter that includes weak interactions of the second co-ordination shell. The difference seen in both solid lines demonstrates that weak interactions of the second co-ordination shell, lead to different bond valence mismatch values therefore a different pseudopotential. For the traditional bond valence parameter (*b*) with a value of 0.37, which is non-variable and identical for all cation-anion combinations, the pseudopotential is represented in **figure 2.6** as a dashed line, which demonstrates that the accuracy of the bond valence value is less as at a given bond length, both bond valence values for Ag-O and Ag-I would be identical. Adams SoftBV parameters [26], varies depending on the shape of the mobile ion and counter-ion species' pseudopotential. This leads to the inclusion of the sum of weak interactions with atoms of the second co-ordination shell, which is found to have a significant contribution to the bond valence sum.

2.5. Calculations & Software

The research carried out in this thesis utilized many software packages which are listed below, the packages used include DFT, modular, analytical software including programming languages and the use of high-performance computing clusters, both internally and externally to the University of Liverpool.

All DFT calculations carried out in this thesis were performed using the Vienna AB-*initio* Simulation Package (VASP) [27]. Both DFT structural optimizations and DFT+U optimizations were performed using the Projector Augmented Wave method [24] with a plane wave basis set. The PBE (Perdew–Burke–Ernzerhof) [11] exchange correlation functional was used throughout all calculations. K-point densities and sampling of the Brillouin zone was done using the Monkhorst-pack k-points [22].

Modelling of all structures was carried out using the Visualisation for Electronic and Structural Analysis (VESTA) software package [28], which plots electronic and nuclear densities and structural morphology and structural models.

Identification of space groups for given structures using given atomic positions in 3D space was carried out using Findsymm [29].

Doping of structures and generating dopant conformers was carried out using the Simdope script.

All convex hull calculations in this thesis was performed using the Python Materials Genomics (Pymatgen) [30], an open-source python library for material analysis. The use of the phase diagram code was integral to the convex hull calculations and was sourced by Pymatgen from Ceder et al [31].

Python programming language was used extensively throughout the work carried out in this thesis to create new analytical scripts and for data processing purposes. The Atomic Simulation Environment (ASE) [32] python tools were also used for many of the calculation processes carried out.

Computational hardware required for the calculations throughout were rigorous. The University of Liverpool (UoL) High Performance Computing (HPC) facilities were instrumental in carrying out the research within this thesis. The UoL HPCs that were used included the Chadwick Cluster and Barkla Cluster. The University College London (UCL) Materials and Molecular Modelling (MMM) Michael

Cluster was also used throughout, this system was funded, and access was provided from the EPSRC Tier 2 system.

- **Software: VASP, VESTA, Findsymm, Simdope, Pymatgen, Python, ASE.**
- **High Performance Computing: UOL – Chadwick, Barkla. UCL (EPSRC) – MMM Michael.**

2.6. References

1 M. C. Payne, M. P. Teter, D. C. Ailan, T. A. Arias and J. D. Joannopouios, *Rev. Mod. Phys.*, 1992, **64**, 1045–1097.

2 J. Frédéric Bonnans, J. Charles Gilbert, C. Lemaréchal and C. A. Sagastizábal, *Numerical Optimization*, Springer Berlin Heidelberg, 2006.

3 W. Kohn, A. D. Becke and R. G. Parr, *J. Phys. Chem.*, 1996, **100**, 12974–12980.

4 V. Milman, B. Winkler, J. A. White, C. J. Pickard, M. C. Payne, E. V Akhmatskaya and R. H. Nobes, *Electronic Structure, Properties, and Phase Stability of Inorganic Crystals: A Pseudopotential Plane-Wave Study*, 2000, vol. 77.

5 F. Ban, K. N. Rankin, J. W. Gauld and R. J. Boyd, *Theor. Chem. Acc.*, 2002, 108, 1–11.

6 N. Gresh, G. A. Cisneros, T. A. Darden and J. P. Piquemal, *J. Chem. Theory Comput.*, 2007, **3**, 1960–1986.

7 M. Born and R. Oppenheimer, *Ann. Phys.*, 1927, **389**, 457–484.

8 P. Hohenberg and W. Kohn, *Phys. Rev.*, 1964, **136**, B864.

9 R. P. Feynman, N. Metropolis and E. Teller, *Phys. Rev.*, 1949, **75**, 1561–1573.

10 W. Kohn and L. J. Sham, *Phys. Rev.*, 1965, **140**, A1133.

11 J. P. Perdew, K. Burke and M. Ernzerhof, *Phys. Rev. Lett.*, 1996, **77**, 3865–3868.

12 J. P. Perdew and Y. Wang, *Phys. Rev. B*, 1992, **45**, 13244–13249.

13 B. Hammer, L. B. Hansen and J. K. Nørskov, *Phys. Rev. B - Condens. Matter Mater. Phys.*, 1999, **59**, 7413–7421.

14 J. Sun, B. Xiao and A. Ruzsinszky, *J. Chem. Phys.*, 2012, **137**, 8207.

15 J. P. Perdew, A. Ruzsinszky, G. I. Csonka, L. A. Constantin and J. Sun, *Phys. Rev. Lett.*, 2009, **103**, 026403.

16 L. Goerigk and S. Grimme, *J. Chem. Theory Comput.*, 2011, **7**, 291–309.

17 A. I. Liechtenstein, V. I. Anisimov and J. Zaanen, *Phys. Rev. B*, 1995, **52**, R5467.

18 S. L. Dudarev, G. A. Botton, S. Y. Savrasov, C. J. Humphreys and A. P. Sutton, *Phys. Rev. B*, 1998, **57**, 1505–1509.

19 J. C. Slater, *Phys. Rev.*, 1930, **36**, 57–64.

20 W. J. Hehre, R. F. Stewart and J. A. Pople, *J. Chem. Phys.*, 1969, **51**, 2657–2664.

21 G. Kresse and J. Furthmüller, *Phys. Rev. B*, 1996, **54**, 11169–11186.

22 H. J. Monkhorst and J. D. Pack, *Phys. Rev. B*, 1976, **13**, 5188–5192.

23 P. Schwerdtfeger, *ChemPhysChem*, 2011, **12**, 3143–3155.

24 P. E. Blöchl, *Phys. Rev. B*, 1994, **50**, 17953–17979.

25 N. E. Brese and M. O'Keeffe, *Acta Crystallogr. Sect. B Struct. Sci.*, 1991, **47**, 192–197.

26 S. Adams, *Acta Crystallogr. Sect. B Struct. Sci.*, 2001, **57**, 278–287.

27 G. Kresse and J. Furthmüller, *Comput. Mater. Sci.*, 1996, **6**, 15–50.

28 K. Momma and F. Izumi, *J. Appl. Crystallogr.*, 2008, **41**, 653–658.

29 H. T. Stokes and D. M. Hatch, *J. Appl. Cryst*, 2005, **38**, 237–238.

30 S. P. Ong, W. D. Richards, A. Jain, G. Hautier, M. Kocher, S. Cholia, D. Gunter, V. L. Chevrier, K. A. Persson and G. Ceder, *Comput. Mater. Sci.*, 2013, **68**, 314–319.

31 Y. Mo, S. P. Ong and G. Ceder, *Chem. Mater.*, 2012, **24**, 15–17.

32 A. Hjorth Larsen, J. JØrgen Mortensen, J. Blomqvist, I. E. Castelli, R. Christensen, M. Dułak, J. Friis, M. N. Groves, B. Hammer, C. Hargus, E. D. Hermes, P. C. Jennings, P. Bjerre Jensen, J. Kermode, J. R. Kitchin, E. Leonhard Kolsbjerg, J. Kubal, K. Kaasbjerg, S. Lysgaard, J. Bergmann Maronsson, T. Maxson, T. Olsen, L. Pastewka, A. Peterson, C. Rostgaard, J. SchiØtz, O. Schütt, M. Strange, K. S. Thygesen, T. Vegge, L. Vilhelmsen, M. Walter, Z. Zeng and K. W. Jacobsen, *J. Phys. Condens. Matter*, 2017, 29, 273002.

Chapter 3: Investigation of the relative stabilities of Li_3XF, Li_3XOH (X = S, Se) and Li_2MOS (M = Ca, Zn, Mg) as Solid-State Electrolytes

Contribution

All computational work that was carried out in this section was performed by R. E. Morris with support from M. S. Dyer. Experimental work which included the attempted synthesis and characterisation of the Li_3SeF target material along with the experimental report given in this paper, was performed by B. T. Leube.

3.1. Introduction

Battery technology relies heavily on the materials used. Currently lithium-ion battery technology primarily utilizes liquid electrolytes for example $LiPF_6$ and propylene carbonate dissolved $LiClO_4$. These liquid electrolytes are commonly used in portable devices such as mobile phones, laptops, digital cameras etc. $LiClO_4$ type electrolytes face many problems, an example of this would be that they are highly environmentally unfriendly as the liquid within the battery is highly corrosive, toxic, and flammable and can be damaging if discarded improperly, they also suffer from a limited temperature range of operation. Current research includes attempting to improve the Lithium-battery technology using lithium-metal, lithium-oxygen and lithium-sulphur technologies, these have also been widely reviewed [1–3]. There has been a large amount of research carried out to find possible alternative materials for a solid electrolyte. lithium batteries that use a liquid electrolyte are very hazardous due to the highly reactive lithium solid being used in conjunction with a liquid electrolyte which can cause a thermal runaway reaction. Using a solid-state electrolyte would mean that the electrodes would no longer be separated by a liquid phase, therefore removing the risks posed by liquid electrolytes. Current materials that have been explored include superionic conductors such as lithium-NASICONs [4,5], thio-LISICONs [6,7], Rock-salt type superionic conductors [8], Garnet type structures [9], perovskite [10,11] and anti-perovskite structured superionic conductors [12–15].

To offer a technological advance in its use, a new conductor material must meet a certain criteria which includes; (i) low cost, lightweight and low toxicity (economic and environmentally friendly) (ii) must not cause significant electrode corrosion, leakage and must be thermomechanically strong, (iii) must have a large working window in relation to voltage and current, (iv) must have minimum amounts of self-discharge for a longer shelf-life, (v) must be stable in a broad temperature range of -

100°C to 300°C, and most importantly (vi) must have a high ionic conductivity in the order of 10^{-2} S cm^{-1} at room temperature. [13]

Lithium Rich Anti-perovskites (LiRAP) have recently been studied and has a large potential for unexplored materials with $Li_3OCl_{0.5}Br_{0.5}$ highlighted as one of the more successful solid-state electrolytes LiRAP candidate[13,16–18]. Zhao et al [13] had their work inspired by the high temperature superionic conductivity of $NaMgF_3$ and $(K,Na)MgF_3$ [10,19–21]. They proposed an "electronically-inverted" anti-perovskite, Li_3OCl and $Li_3OCl_{0.5}Br_{0.5}$, based on a cationic and anionic inversion of the $NaMgF_3$ conductor. The 'electronic inversion' consists of replacing the traditional perovskite X_3 anion with a cation, in this case, Li^+, and replacing the perovskite A and B cations with anions (O^{2-} and Cl^-). Prior to the study on Li_3OCl and Li_3OBr [13] lithium halide hydrates ($Li_{3-n}(OH)_nCl$ ($0.83 \leq n \leq 2$)) ($Li_{3-n}(OH)_nBr$ ($1 \leq n \leq 2$)) were synthesised and studied by Schwering et al [12] for their conductivity and phase transitions.

Similar to electrolytes, cathode materials are being studied and developed in an attempt to improve battery technology. Current materials used as cathodes include olivine type-$Li_{1-x}FePO_4$ [22], delafossite-$LiCoO_2$ [23] and $LiMnO_2$ [24] and spinel-$Li_{1+x}Mn_2O_4$ [25]. Issues facing these current materials include low mobility in Li^+ ion migration in $Li_{1-x}FePO_4$, expensive and hazardous cobalt in $LiCoO_2$, and the battery degradation caused by the use of $Li_{1+x}Mn_2O_4$. The Li_2FeOS anti-perovskite was recently synthesised and studied as a Li ion conducting cathode material [26]. One method of developing a new electrolyte material is by using the known Li_2FeOS cathode material, the Fe^{2+} ions could be replaced with a more redox inactive metal, this would be done to create an electrolyte analogue of the cathode material. This method was used in a study carried out by Dyer et al [27] where the Fe^{2+} in $LiFePO_4$ was replaced with Mg^{2+}. More recent developments on the field can be found in chapter 1 which includes studied carried out by Islam, Famprikis, Fujii et al [28–30].

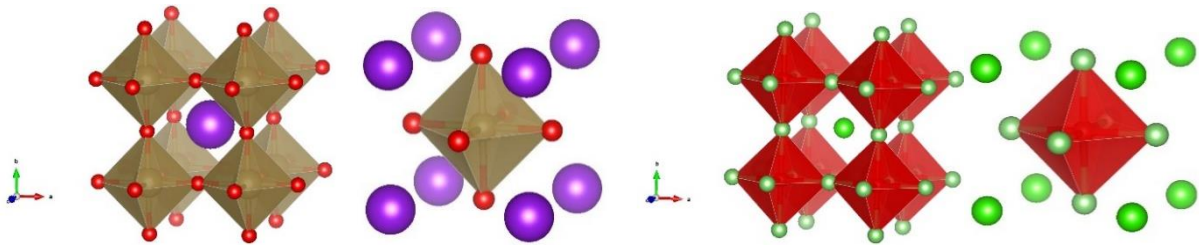

Figure 3.1: Left: $KTaO_3$ unit cell, purple atoms are K^+ atoms, brown polyhedra are TaO_6 groups (ICSD 280424 [31]). Right: Li_3OCl, dark-green atoms are Cl^- atoms, red polyhedra are Li_6O groups with Li^+ as light green atoms.

The traditional perovskite structure consists of a cubic structure which follows ABX_3, a well-known example of this structure includes $CaTiO_3$. $CaTiO_3$ at room temperature is an orthorhombic structure, hence a more suitable example of a cubic perovskite would be $KTaO_3$, where two cation sites both A which is occupied by K^+ and B which is occupied by Ta^{5+}, the X_3 anion site is occupied by the O^{2-} anions. Figure 1 (a) shows the perovskite structure of $KTaO_3$. The B cation site consists of smaller octahedral sites which are all octahedrally co-ordinated with the X site anions (BX_6). The large central A cation site is a dodecahedral site. For an anti-perovskite, the ions are electronically inverted, which results in the A site consisting of a larger anion, the B site consisting of a smaller anion which is octahedrally co-ordinated to the X site cations. Figure 1 (b) shows the anti-perovskite structure of Li_3OCl.

As identified previously, the phase stability of a solid-state electrolyte is critical in identifying a viable material. This is to ensure limited degradation of the electrolyte at the interfaces with the formation of dendrite growth and decomposition into more stable competing phases within the phase group. The phase group and stability of a perovskite and anti-perovskite can be described by the Goldschmidt Tolerance Factor (T_F). This factor can be used as an indicative method of determining if the anion and cation combination within a perovskite or anti-perovskite are compatible with a given phase. In equation 3.1.1, for a typical perovskite the tolerance factor (T_F) is the result of the sum of radius of cation A (r_A) with the radius of the system anion (r_0) over the square root of 2 by the sum of cation radius B (r_B) and anion radius (r_0). The same is true for an anti-perovskite, but in this case r_0 represents the radius of the cation in the system and r_A and r_B represent the radius of both anions. For a symmetrical cubic structure, if all edges of the cube are equal in length and are at an angle of 90° to each other, the ratio, hence the T_F for that cubic structure will be exactly 1. Therefore, T_F for a perfectly symmetrical cubic structure is 1.

$$T_F = \frac{r_A + r_0}{\sqrt{2}(r_B + r_0)} \qquad (3.1.1)$$

For a perovskite or anti-perovskite system a T_F of >1 indicates that a hexagonal or tetragonal structure will likely be present. Values ranging between 0.9-1 indicates a cubic structure perovskite or anti-perovskite. Values in the range of 0.71 to 0.9 T_F indicates that an orthorhombic or rhombohedral structure will be present. Values that are lower than 0.71 can vary significantly in structure.

In this study we explore the stability and convex hull energies of a series of new LiRAPs having selected new cationic and anionic combinations through chemical intuition along with the assessment of their agreement with the Goldschmidt tolerance factor. We report the results in 3 parts based on the

new potential materials, which are the following: (i) Li_3XF (X = S, Se), (ii) Li_3XOH (X = S, Se), (iii) Li_2MOS (M = Ca, Zn, Mg). In each section we report and discuss the relative stabilities of the materials along with their convex hull energies, identifying their decomposition. In section (i) we also report and discuss the results of the attempted synthesis of Li_3SeF.

3.2. Methods

Computational Methods

Disorder within the Li_2MOS structures were populated by using the simdope script [32], with the initial structure originating from the Li_2FeOS (ICSD 253936 [33]) structure. This was done by creating a supercell of a 100% Li occupied Li_3OS unit cell with a (***a***-***b***, ***a***+***b***, 2***c***) transformation. Simdope was then used to dope M^{2+} in to replace Li^+ at a 33.33% ratio, whilst generating all possible symmetrically unique structures. The initial Li_3OS cell contained 12 Li atoms, 4 O atoms and 4 S atoms. For the simdope substitution 4 Li atoms were removed, then repopulated with Ca, Zn and Mg separately. Resultant structures produced by the simdope script were then relaxed using first principles DFT calculations.

Optimizations of all materials was carried out using DFT calculations utilizing the Perdew-Burke-Ernzerhof generalized gradient approximation.[34] The Vienna *ab-initio* Simulation Package (VASP) was used to perform the relaxations. [35] The geometry optimizations were performed with a projection done in a reciprocal space using a conjugate gradient algorithm with Gaussian smearing [36]. For the k-point sampling of the Brillouin zone integrals, a 10×10×10 Monkhorst-Pack grid was used,[37] and an energy cutoff of 650 eV was set for the plane wave basis-set. The relaxation of the unit cell was done by the total energy minimization with breakdown conditions for the sc-loop set to $1x10^{-5}$ eV and -0.01 eV for the ionic relaxation loop. These were values selected based on earlier work in the group.

Convex hull energy (E_{Hull}) calculations for target materials were carried out using the Pymatgen software [32].

The Goldschmidt tolerance factors (T_F) which were calculated in this study used radii values from Shannon radii [38]. The values used consisted of the following, for Li_3SeF and Li_3SF, a Li^+ ionic radius of 0.76 Å, a F^- ionic radius of 1.33 Å, a S^{2-} ionic radius of 1.84 Å, and for Se^{2-} a ionic radius of 1.98 Å. For Li_3OCl and Li_3OBr, an O^{2-} ionic radius of 1.4 Å, a Cl^- radius of 1.81 Å and for Br^- a ionic radius of 1.96 Å.

For comparison of stability, the formation energies (E_{form}) of the target materials were calculated using their total ground state energies. Comparison of the calculated E_{form} was made with energies given by the Formation Energy Predictor, using an ElemNet model [39].

Experimental Methods

Synthesis

Lithium granules (Aldrich, granular, 99 %, 3.98 mmol, 27.6 mg), Selenium powder (AlfaAesar, ~200 mesh, 99.999 %, 1.99 mmol, 157.0 mg) and Lithium fluoride (Aldrich, 99.995 %, 1.99 mmol, 51.6 mg) were used as provided. The reagents were placed in an alumina crucible without grinding and sealed in in a quartz tube under vacuum (1×10^{-4} mbar). The mixture was heated to 973 K for 10 h (heating rate: 0.2 K/min) and then cooled to ambient temperature (1 K/min).

Characterisation

Powder X-ray diffraction experiments were carried out at ambient temperature on powders sealed in borosilicate glass capillaries. A Bruker D8 diffractometer with a monochromated Mo source ($K\alpha_1$, λ= 0.7093 Å) in Debye-Scherrer geometry was used for phase identification.

3.3. Results

Li_3XF (X = S, Se)

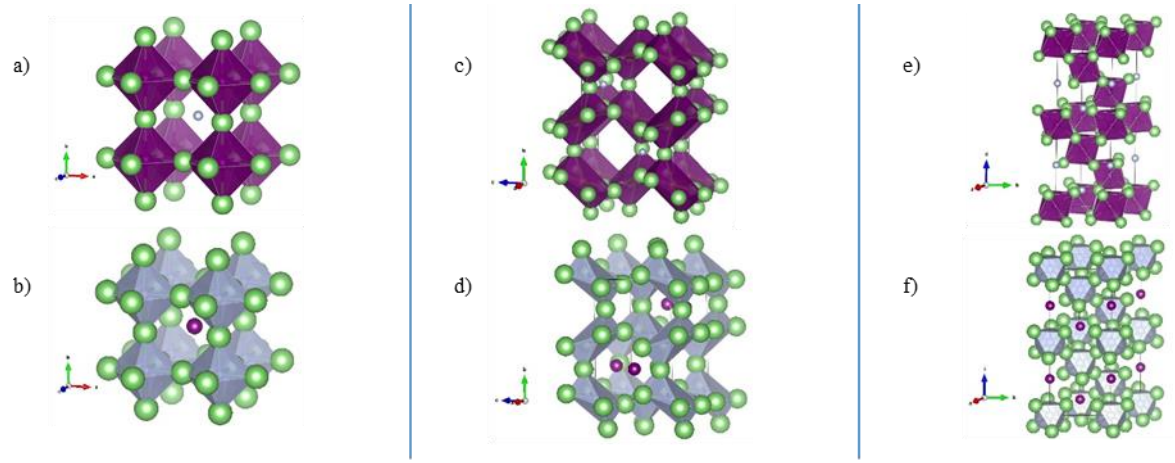

Figure 3.2. DFT optimised structures of a) Cubic Li_3SeF 'Swapped', b) Cubic Li_3SeF, c) Distorted orthorhombic Li_3SeF 'Swapped', d) Distorted orthorhombic Li_3SeF, e) Tilted rhombohedral Li_3SeF 'Swapped', f) Tilted rhombohedral Li_3SeF. Green atoms represent Li^+ position, light blue atoms represent F^- positons and purple atoms represent Se^{2-} positons. Non-swapped structures contain octahedral Se^{2-}, 'swapped' structures contain octahedral F^-.

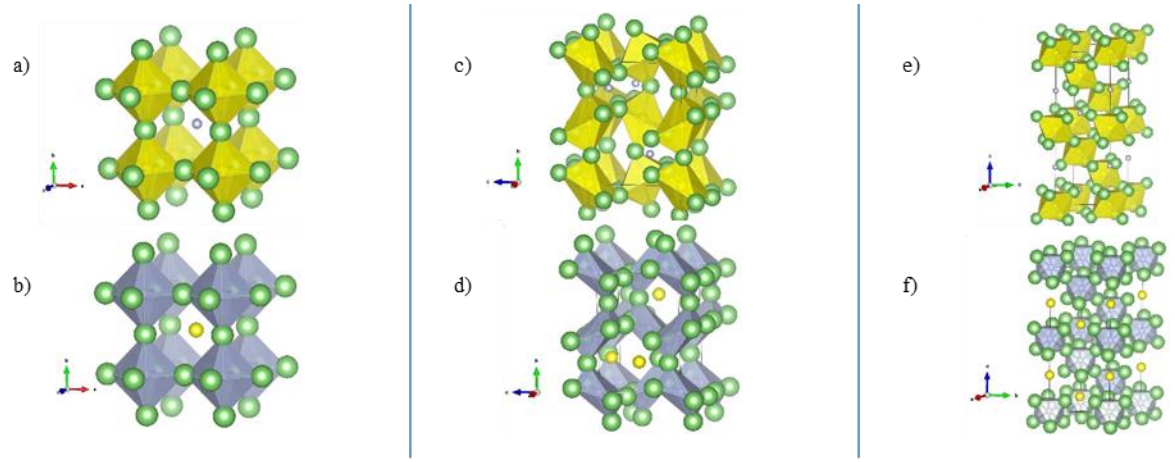

Figure 3.3. DFT optimised structures of a) Cubic Li_3SF 'Swapped', b) Cubic Li_3SF, c) Distorted orthorhombic Li_3SF 'Swapped', d) Distorted orthorhombic Li_3SF, e) Tilted rhombohedral Li_3SF'Swapped', f) Tilted rhombohedral Li_3SF. Green atoms represent Li^+ position, light blue atoms represent F^- positons and yellow atoms represent S^{2-} positions. Non-swapped structures contain octahedral Se^{2-}, 'swapped' structures contain octahedral F^-.

For Li_3XF (X = S, Se), both Li_3SF and Li_3SeF were studied with the S/Se occupying the dodecahedral positions and F in the octahedral positions. Distortion to the structures was also introduced and studied energetically, in the form of a rhombohedral tilt and an orthorhombic distortion, to increase conductivity by creating disorder within the structures. Both cubic structures consisted of the *Pm-3m* space group with the distorted orthorhombic structure as *Pnma*, this was based on the $GdFeO_3$ distorted orthorhombic perovskite [40] and the tilted rhombohedral structure has the *R-3c* structure based on the $LaAlO_3$ structure [41]. The cells were constructed by swapping the co-ordinating ABX_3 positions

with their anti-perovskite counter-parts, i.e. O_3 positions swapped for Li atoms. Their 'swapped' structures were also studied where the S/Se occupied the octahedral positions and F occupied the dodecahedral positions. **Figure 3.2** displays the final optimized structures. Introducing S and Se into the well-known Li_3OCl, Li_3OBr structure [13] was done with the interest of increasing the potential conductivity of the anti-perovskite, whilst exploring a new phase field with the *Pm-3m* structure. F^- was introduced as a counter ion in the halogen series that would closely relate to the Goldschmidt tolerance factor (T_F) for Li_3OCl and Li_3OBr. Similarly S^{2-} and Se^{2-} were selected for their radii and alignment with the T_F of Li_3OCl and Li_3OBr. Sulfide based electrolytes are also good alternatives to oxide based electrolytes as they demonstrate high ionic conductivity and low interfacial resistance over cycling [42]. T_F was calculated using values from Shannon radii [38]. Li_3SeF and Li_3SF both consist of T_F values of 0.927 and 0.879 respectively, which can be categorized as cubic following the T_F structure classification. Similarly, Li_3OCl and Li_3OBr have T_F values of 0.841 and 0.890 respectively, which can also be categorized as stable cubic structures. The 'swapped Li_3XF structures consisted of T_F values of 0.539 for Li_3SeF (swapped) and 0.568 for Li_3SF (swapped), the classification would identify these structures as non-cubic or very unstable as cubic structures.

Convex hull energies that were calculated can be seen in **table 3.1**. 'Swapped' structures which have significantly lower T_F support the categorization of stability. Reduced T_F values of 0.539 and 0.568 for Li_3SeF and Li_3SF respectively align with a significant increase in energy calculated above the convex hull. For the cubic swapped structures an increase in energy above the hull can be seen of close to 500 meV/atom for both Li_3SeF and Li_3SF with an increase in energy in the distorted orthorhombic, tilted rhombohedral structures for Li_3SF and the distorted orthorhombic Li_3SeF structure. The only decrease in energy that can be found by swapping the F and Se sites in the Li_3SeF tilted rhombohedral structure, where its energy above the hull is reduced by 20 meV/atom. The most promising candidate based on the convex hull energies calculated is the cubic Li_3SeF which can be classified as an energetically metastable structure. As a reference energy, the convex hull energy for both Li_3OCl and Li_3OBr were calculated. Both had an E_{Hull} of 0 meV/atom, which was lower compared to energies calculated by Zhang et al [16]. This result supports experimental studies carried out on these LiRAP materials where both were synthesised and were found to be stable [13].

Table 3.1 Convex Hull Energies of Li_3MCh (M = S, Se, O; Ch = F, Cl, Br) target materials.

Structure	Normal Anion Order Energy Above Hull (meV/atom)	Swapped Anion Order Energy Above Hull (meV/atom)
Li_3SF	73	498
Li_3SF (Distorted Orthorhombic)	69	143
Li_3SF (Tilted Rhombohedral)	74	122
Li_3SeF	48	569
Li_3SeF (Distorted Orthorhombic)	57	123
Li_3SeF (Tilted Rhombohedral)	132	112
Li_3OCl	0 (14)[1]	-
Li_3OBr	0 (26)[1]	-

[1] = Data from Y. Zhang, Y. Zhao, C. Chen, C. Chem, Phys.Rev.B. 87, 134303, (2013)

Attempted experimental synthesis of the Li_3SeF candidate was carried out. The reaction of lithium granules, selenium powder and lithium fluoride in an evacuated and sealed quartz tube at 973 K yielded a homogenous bulk material. Quantitative Rietveld analysis of the PXRD pattern, **figure 3.4,** indicates in the formation of 77(2) wt% Li_2Se and 22(2) wt% LiF, while no further crystalline reaction products are present. The weight fractions of the products agree well with the full conversion into Li_2Se (expected: 78.2 wt%) and LiF (expected: 21.8 wt%), showing that no reagents were lost during the reaction. A repeated firing at 1123 K for 5 h did not result in a change of the PXRD pattern. These confirm that no stable anti-perovskite phase forms in the considered experimental regime. But it remains unclear whether Li_3SeF does not form at elevated temperature and decomposes into LiF and Li_2Se or whether it does not form at all. High-temperature PXRD studies would be needed to completely study the potential Li_3SeF anti-perovskite.

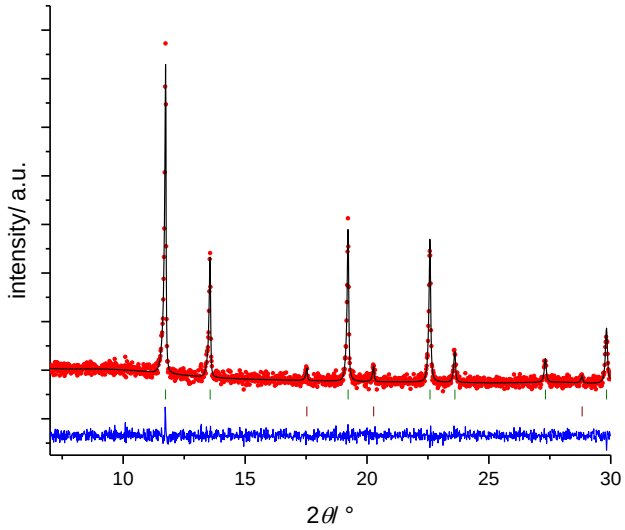

Figure 3.4. Rietveld refinement of "Li_3SeF" after firing to 973 K for 10 h. Two reaction products can be identified: Li_2Se (77(2) wt%) and LiF (22(2) wt%). The positions of Bragg reflections are indicated by tic-marks (green: Li_2Se, violet: LiF).

Products of the attempted synthesis align with the decomposition calculated by the convex hull energy calculations with Li_3SeF 48meV/atom over the hull with decomposition into LiF and Li_2Se. Similarly, for Li_3SF the decomposition indicates LiF and Li_2S as the products. This can be seen clearly in the phase diagrams produced in **figure 3.5**.

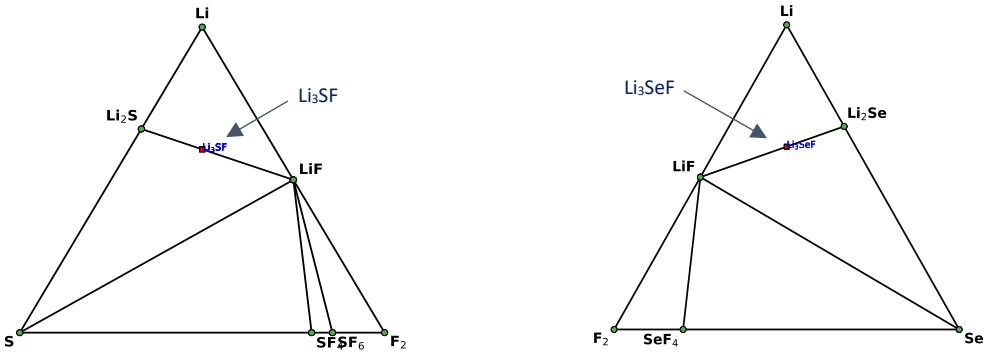

Figure 3.5. Left: Phase diagram for Li_3SF (decomposition into Li_2S and LiF). Right: Phase diagram for Li_3SeF (decomposition into Li_2Se and LiF). Green symbols on the diagrams represent stable compounds, with red symbols displaying unstable compounds.

Li_3XOH (X = S, Se)

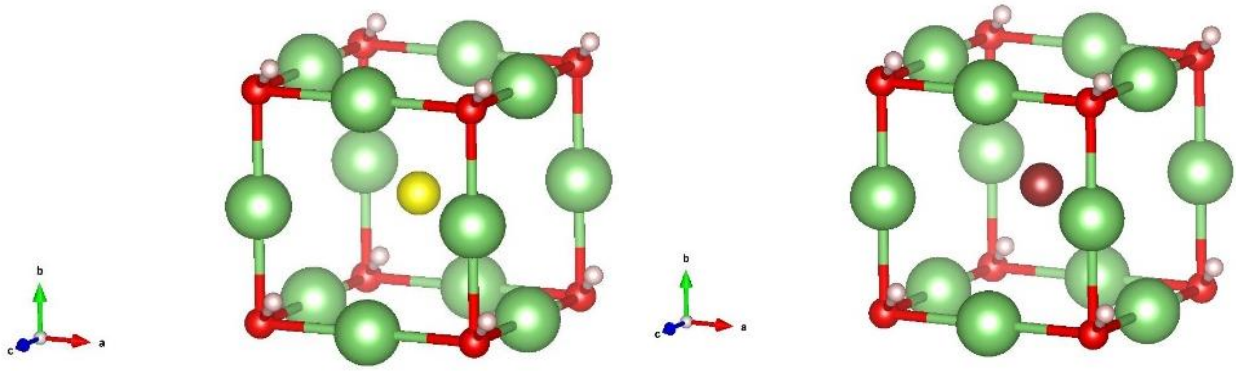

Figure 3.6. Left: cubic Li_3SOH, Right: Li_3SeOH. Green atoms represent Li^+ position, red atoms represent O^{2-} positions, light pink atoms represent H^+ positions, burgundy atoms represent Se^{2-} positions and yellow atoms represent S^{2-} positions.

LiF is a highly stable competing phase, which makes an F^- containing LiRAP convex hull energy significantly higher relative to the LiF phase. As a way of maintaining a cubic structure that aligns with the recommended T_F values whilst also having less stable competing phases than the previously proposed F^- anions, hydroxide OH^- groups were used. *Pm-3m* space group structures were modelled with the OH^- group occupying the octahedral corner sites of the structure. T_F values were calculated as 0.863 and 0.909 for Li_3SOH and Li_3SeOH respectively, which aligns to similar values calculated for Li_3OCl and Li_3OBr. Their relative stabilities were studied in relation to their most stable competing phases LiOH and Li_2S/Li_2Se. Li_3SOH and Li_3SeOH were found to have relative stability energies of 90.5meV/atom and 70meV/atom respectively, favouring the formation of LiOH and Li_2S/Li_2Se. Due to their convex hull energies being significantly higher than the 50meV threshold of being deemed as metastable, the attempted synthesis of these structures was not carried out.

Li_2MOS (M = Ca, Zn, Mg)

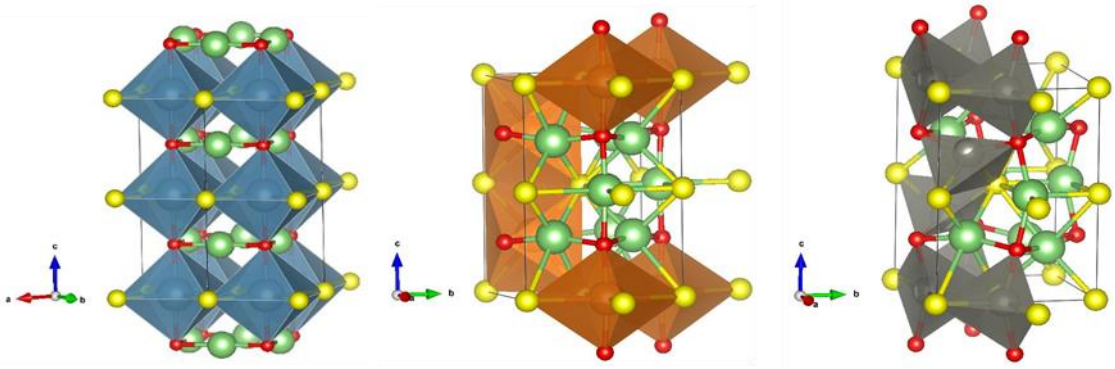

Figure 3.7. Left: Li_2CaOS, Middle: Li_2MgOS, Right: Li_2ZnOS. Green atoms represent Li^+ position, red atoms represent O^{2-} positions, yellow atoms represent S^{2-} positions, blue polyhedra represent the $CaOS^{2-}$ group, orange polyhedra represent the $MgOS^{2-}$ group, grey polyhedra represent $ZnOS^{2-}$ group.

The optimized structures of Li_2MOS (M = Ca, Mg, Zn) with the lowest TGSE (most stable) were selected from the symmetrically unique M doped structures produced by simdope [32] and are shown in **figure 3.7 and 3.8**. In Li_2CaOS the Ca^{2+} ions occupy 6 co-ordinate octahedral positions, which is expected in an undistorted anti-perovskite. The octahedra are positioned in a layered ordering separated by Li_2O groups, this was found to be the optimal disorder within the structure. For Li_2MgOS the Mg^{2+} ions again occupy 6 co-ordinate octahedral positions, but in a less ordered fashion compared to Li_2CaOS, where the Mg^{2+} groups align along the c axis, whilst also layering perpendicular to the c axis in the 110 direction. In Li_2ZnOS, there is more disorder with the arrangement of Zn^{2+} ions, where they are 4 co-ordinate tetrahedral sites arranged with disorder within the structure. The Zn polyhedra can be separated in layers, where there is a layer of pentahedral ZnO_2S_3 which have Zn atoms shifted along the b-axis such that the Zn atoms are no longer octahedrally co-ordinated to the S^{2-} atom. These layers are separated by tetrahedral ZnO_2S_2 groups where the Zn^{2+} atoms have shifted along the c axis away from their octahedrally co-ordinating S^{2-} atom. The octahedral tilting seen in Li_2ZnOS gives the structure a *P2221* space group and the tilting can be described as an $a^0b^-c^-$ tilt using Glazer notation [43]. Tilting in the structure can be explained by Zn's preference to be tetrahedrally co-ordinated in the structure.

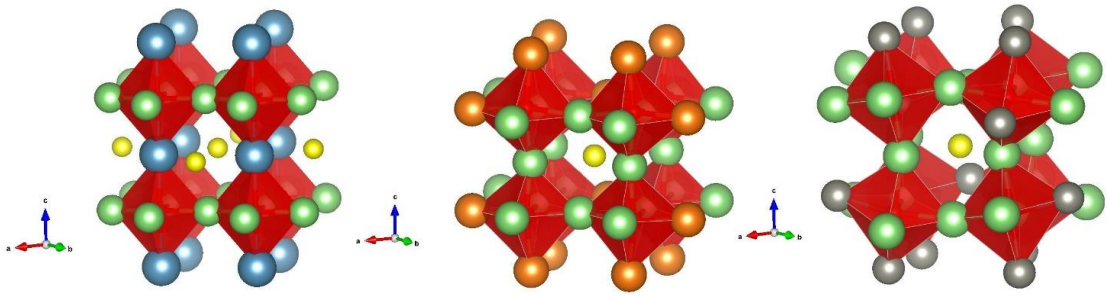

Figure 3.8. Left: Li_2CaOS, Middle: Li_2MgOS, Right: Li_2ZnOS optimized targets. Green atoms represent Li^+ position, red atoms represent O^{2-} positions, and yellow atoms represent S^{2-} positions. Red polyhedra represent the OLi_4M_2 groups.

Table 3.2 Convex Hull Energies of Li_2MF (M = Ca, Mg, Zn) target materials.

Structure	Energy Above Hull (meV/atom)
Li_2CaOS	69
Li_2MgOS	122
Li_2ZnOS	60
Li_2FeOS*	21

* Reference Calculation for the known Li_2FeOS

Li_2ZnOS was found to be the most stable structure (**table 3.2**) from those studied with an energy above the hull of 60 meV/atom with decomposition into Li_2O and ZnS. Li_2CaOS was only slightly less stable with an energy above the hull of 69 meV/atom with decomposition into Li_2S and CaO, both could be considered metastable under the correct conditions. Li_2MgOS was determined to be unstable with an energy above the hull of 122 meV/atom with decomposition into Li_2S and MgO. For reference, the same techniques were carried out on Li_2FeOS, which was found to have an energy above the hull of 21meV/atom indicating the structure as metastable which aligns with the study carried out on Li_2FeOS [26,33] where the polycrystalline structure is formed but decomposes and the

single crystal appears to be slightly more stable. The phase diagrams for the Li_2MOS target materials can be found in the S.I (S.I 3-6).

3.4. Discussion

For Li_3XF (X = S, Se), it is understandable that the energy above the hull was high leading to all proposed structures except from Li_3SeF to be unstable. This can be explained due to the relative stabilities of the competing phases. Table 1 in the S.I. displays the formation energies (E_{form}) calculated in this study relative to the phase elements and the E_{form} calculated by the ElemNet E_{form} predictor. For Li_3SF, both LiF and Li_2S are highly stable. Our calculated formation energy (E_{Form}) for LiF was -3.055 eV/atom (-2.972 eV/atom given by ElemNet [39]) and -1.353 eV/atom (-1.454 eV/atom ElemNet) for Li_2S, therefore any target materials which compete against these phases for formation will likely decompose or not form at all. This is also true for Li_3SeF with LiF and Li_2Se where Li_2Se has a formation energy of -1.272 eV/atom (-1.278 eV/atom ElemNet). Although in Li_3SeF, Li_2Se is less stable than Li_2S which leads to Li_3SeF being potentially metastable in nature. When comparing the calculated E_{Form} and ElemNet values of both Li_3SeF and Li_3SF, the calculated values are higher in energy than the ElemNet values, with the most significant difference being seen with Li_3SeF. The calculated E_{Form} for Li_3SeF is roughly 0.22 eV/atom higher than the ElemNet E_{Form}. This would indicate that using ElemNet E_{Form}, Li_3SeF would be predicted as stable as the lower E_{Form} of ElemNet and higher ElemNet E_{Form} of Li_2Se and LiF compared to calculated values would lead to a lower higher relative stability of Li_3SeF compared to its decomposition products.

The $GdFeO_3$ type orthorhombic distortion and $LaAlO_3$ type rhombohedral tilting demonstrated a significant decrease in stability for both Li_3SF and Li_3SeF, except for the distorted orthorhombic Li_3SF, where its energy above the hull was lowered from 73 meV/atom in the cubic phase to 69 meV/atom in the distorted orthorhombic phase. Neither structure relaxed back to a cubic structure. The deviation away from the 'ideal' perovskite followed the principle of the Goldschmidt tolerance factor, given the T_F for Li_3SeF and Li_3SF were 0.927 and 0.879 respectively, the most stable structure based on the factor would be a cubic structure. Deviation away from cubic has shown a decrease in stability which supports the Goldschmidt principle. Swapping in positions of the S^{2-}, Se^{2-} and F^- has also demonstrated that deviation away from the T_F displays a significant decrease in stability. T_F values for both 'swapped' Li_3SeF and Li_3SF were 0.539 and 0.568 respectively which would identify the structures to be closest to their ideal structure at a highly distorted symmetry. Li_3SOH and Li_3SeOH were both less stable than their F^- counterparts by +17 meV/atom and +22 meV/atom when compared

to Li_3SF and Li_3SeF respectively. Despite the less stable competing phase of LiOH in comparison to LiF, the target structures themselves were much less stable. This result was counter-intuitive and contrary to what was thought in relation to lowering the stability of the competing phases, i.e., from using F^- with a LiF (-3.055 eV/atom E_{form}) competing phase to a less stable LiOH competing phase with a E_{form} of -2.307 eV/atom (-1.626 eV/atom ElemNet) as Li_3SeF was found to be the most stable candidate with the lowest E_{Hull} of 48 meV/atom. To create a new competitive target LiRAP material in relation to the convex hull energy, less stable competing phases (lower E_{form}) would be required to lower the relative energy of the competing phases which would in turn decrease the stability requirement of the target material, and the target material itself would require a lower E_{form} (higher stability).

All three Li_2MOS target materials were found to be less stable than Li_2FeOS in relation to their E_{Hull}. The calculated and ElemNet E_{form} of Li_2FeOS was much higher (less stable) compared to Li_2CaOS, Li_2MgOs and Li_2ZnOS which initially indicate it as a less stable compound in comparison to the other target materials. However, the lower E_{Hull} of Li_2FeOS is a result of having less stable competing phases, with decomposition into Li_2S, Fe_2O_3, and Fe indicated by the convex hull energy calculation. Decomposition for Li_2CaOS was found to be CaO and Li_2S, MgO and Li_2S for Li_2MgOS and ZnS and Li_2O for Li_2ZnOS. CaO and MgO have a lower E_{form} than ZnS, Li_2O, Fe_2O_3, which make them more stable, hence more competitive under synthesis. This explains the higher E_{Hull} values calculated for both Li_2CaOS and Li_2MgOS in comparison to Li_2FeOS and Li_2ZnOS.

Decomposition favouring Li_2S, MgO or CaO and Li_2O and ZnS, for Li_2MgOS, Li_2CaOS, and Li_2ZnOS was expected due to the lower competing phase E_{form} (higher stability) for Li_2CaOS, Li_2MgOS and Li_2ZnOS. Li_2ZnOS had the lowest E_{Hull} from the Li_2MOS target materials, this is due to the low stability (higher E_{form}) of its decomposition phases Li_2O and ZnS relative to the MO and Li_2S decomposition phases which have a lower E_{form}. For a substituted Li_2MOS material to be viable, the total ground state of the target material would need to be significantly lower (more stable) to be closer to the convex hull energy.

Since our research was carried out, a recent study by Fujii and Gao et al [30] was carried out which led to the high pressure synthesis of a series of anti-prevoskites, M_3FCh (M = Li, Na; Ch = S, Se, Te). In their study they successfully synthesised Li_3SeF and Li_3SF, although for Li_3SF a much higher pressure was required to stabilise the structure at over 20 GPa as opposed to under 5 GPa for Li_3SF. Their results in synthesising the compounds demonstrates the metastability of Li_3SeF and that the more unstable Li_3SF can be formed but at much higher pressures with more difficulty, but also that the anti-perovskite structures are a viable family of structures in which further research and exploration to identify a potential superionic solid-state conductor is possible.

3.5. Conclusion

In this study, we have reported the computational convex hull energy studies carried out on Li_3XF (X = S, Se), Li_3XOH (X = S, Se) and Li_2MOS (M = Ca, Mg, Zn). We have also reported the attempted synthesis of the most promising candidate studied, Li_3SeF. The objective was to explore further into the LiRAP field and attempt to identify new solid-state electrolyte and cathode materials. Following the Goldschmidt tolerance factor as an indicator of stability for selecting appropriate cation and anion combination proved to be successful, the 'swapped' Li_3XF materials with reduced T_F displayed significantly lower stability, with the rhombohedral tilted and distorted orthorhombic structures also decreasing stability. Cubic Li_3SeF was found to be the most stable of all the proposed candidates with a stability of 48meV/atom. The experimental regime proved to yield no stable anti-perovskite materials. Li_3XOH (X = S, Se) were found to be unstable relative to their decomposition products. For the Li_2MOS (M = Ca, Mg, Zn) anti-perovskites, none were found to be stable. The study has shown that there is potential to further explore and study the LiRAP field, using both computational and experimental techniques to identify new materials.

3.6. References

1 P. G. Bruce, S. a. Freunberger, L. J. Hardwick and J.-M. Tarascon, *Nat. Mater.*, 2012, **11**, 19–29.

2 W. Xu, J. Wang, F. Ding, X. Chen, E. Nasybulin, Y. Zhang and J.-G. Zhang, *Energy Environ. Sci.*, 2014, **7**, 513–537.

3 R. Younesi, G. M. Veith, P. Johansson, K. Edstrom and T. Vegge, *Energy Environ. Sci.*, 2015, **8**, 1905–1922.

4 B. E. Taylor, A. D. English and T. Berzins, *Mater. Res. Bull.*, 1977, **12**, 171–181.

5 M. Subramanian, R. Subramanian and A. Clearfield, *Solid State Ionics*, 1986, **18**–**19**, 562–569.

6 R. Kanno, T. Hata, Y. Kawamoto and M. Irie, *Solid State Ionics*, 2000, **130**, 97–104.

7 N. Kamaya, K. Homma, Y. Yamakawa, M. Hirayama, R. Kanno, M. Yonemura, T. Kamiyama, Y. Kato, S. Hama, K. Kawamoto and A. Mitsui, *Nat. Mater.*, 2011, **10**, 682–686.

8 O. Amiel, D. C. Frankel and H. Wada, *J. Solid State Chem.*, 1995, **116**, 409–421.

9 V. Thangadurai, H. Kaack and W. J. F. Weppner, *J. Am. Ceram. Soc.*, 2003, **86**, 437–440.

10 M. O'keeffe and J. O. Bovin, *Science*, 1979, **206**, 599–600.

11 L. Latie, G. Villeneuve, D. Conte and G. Le Flem, *J. Solid State Chem.*, 1984, **51**, 293–299.

12 G. Schwering, A. Hönnerscheid, L. van Wüllen and M. Jansen, *ChemPhysChem*, 2003, **4**, 343–348.

13 Y. Zhao and L. L. Daemen, *J. Am. Chem. Soc.*, 2012, **134**, 15042–15047.

14 Y. Li, W. Zhou, S. Xin, S. Li, J. Zhu, X. Lü, Z. Cui, Q. Jia, J. Zhou, Y. Zhao and J. B. Goodenough, *Angew. Chemie Int. Ed.*, 2016, **55**, 9965–9968.

15 A. Emly, E. Kioupakis and A. Van der Ven, *Chem. Mater.*, 2013, **25**, 4663–4670.

16 Y. Zhang, Y. Zhao and C. Chen, *Phys. Rev. B*, 2013, **87**, 134303.

17 X. Lü, G. Wu, J. W. Howard, A. Chen, Y. Zhao, L. L. Daemen and Q. Jia, *Chem. Commun.*, 2014, **50**, 11520–2.

18 Z. Lu, C. Chen, Z. M. Baiyee, X. Chen, C. Niu and F. Ciucci, *Phys. Chem. Chem. Phys.*, 2015, **17**, 32547–32555.

19 Y. Zhao, D. J. Weidner, J. B. Parise and D. E. Cox, *Phys. Earth Planet. Inter.*, 1993, **76**, 1–16.

20 Y. Zhao, *J. Solid State Chem.*, 1998, **141**, 121–132.

21 A. Yoshiasa, D. Sakamoto, H. Okudera, M. Sugahara, K. Ota and A. Nakatsuka, *Zeitschrift für Anorg. und Allg. Chemie*, 2005, **631**, 502–506.

22 A. K. Padhi, K. S. Nanjundaswamy and J. B. Goodenough, *J. Electrochem. Soc.*, 1997, **144**, 1188–1194.

23 K. Mizushima, P. C. Jones, P. J. Wiseman and J. B. Goodenough, *Mater. Res. Bull.*, 1980, **15**, 783–789.

24 A. R. Armstrong and P. G. Bruce, *Nature*, 1996, **381**, 499–500.

25 M. M. Thackeray, W. I. F. David, P. G. Bruce and J. B. Goodenough, *Mater. Res. Bull.*, 1983, **18**, 461–472.

26 Z. Lu and F. Ciucci, *J. Mater. Chem. A*, 2018, **6**, 5185–5192.

27 L. Enciso-Maldonado, M. S. Dyer, M. D. Jones, M. Li, J. L. Payne, M. J. Pitcher, M. K. Omir, J. B. Claridge, F. Blanc and M. J. Rosseinsky, *Chem. Mater.*, 2015, **27**, 2074–2091.

28 E. Ahiavi, J. A. Dawson, U. Kudu, M. Courty, M. S. Islam, O. Clemens, C. Masquelier and T. Famprikis, *J. Power Sources*, 2020, **471**, 228489.

29 M. J. Clarke, J. A. Dawson, T. J. Mays and M. S. Islam, *ACS Appl. Energy Mater.*, 2021, **4**,

5094–5100.

30 S. Fujii, S. Gao, C. Tassel, T. Zhu, T. Broux, K. Okada, Y. Miyahara, A. Kuwabara and H. Kageyama, *J. Am. Chem. Soc.*, 2021, **143**, 10668–10675.

31 E. A. Zhurova, Y. Ivanov, V. Zavodnik and V. Tsirelson, *Acta Crystallogr. Sect. B Struct. Sci.*, 2000, **56**, 594–600.

32 S. P. Ong, W. D. Richards, A. Jain, G. Hautier, M. Kocher, S. Cholia, D. Gunter, V. L. Chevrier, K. A. Persson and G. Ceder, *Comput. Mater. Sci.*, 2013, **68**, 314–319.

33 K. T. Lai, I. Antonyshyn, Y. Prots and M. Valldor, *J. Am. Chem. Soc.*, 2017, **139**, 9645–9649.

34 J. P. Perdew, K. Burke and M. Ernzerhof, *Phys. Rev. Lett.*, 1996, **77**, 3865–3868.

35 G. Kresse and J. Furthmüller, *Phys. Rev. B*, 1996, **54**, 11169–11186.

36 W. H. Press, B. P. Flannery, S. A. Teukolsky, W. T. Vetterling and H. Gould, *Am. J. Phys.*, 1987, **55**, 90–91.

37 H. J. Monkhorst and J. D. Pack, *Phys. Rev. B*, 1976, **13**, 5188–5192.

38 R. D. Shannon, *Acta Crystallogr. Sect. A*, 1976, **32**, 751–767.

39 A. Agrawal, B. Meredig, C. Wolverton and A. Choudhary, in *2016 IEEE 16th International Conference on Data Mining Workshops (ICDMW)*, IEEE, 2016, pp. 1276–1279.

40 S. Geller, *J. Chem. Phys.*, 1956, **24**, 1236–1239.

41 S. Geller and V. B. Bala, *Acta Crystallogr.*, 1956, **9**, 1019–1025.

42 J. Lee, T. Lee, K. Char, K. J. Kim and J. W. Choi, *Acc. Chem. Res.*, 2021, **54**, 3390–3402.

43 A. M. Glazer, *Acta Crystallogr. Sect. B Struct. Crystallogr. Cryst. Chem.*, 1972, **28**, 3384–3392.

3.7. Supporting Information

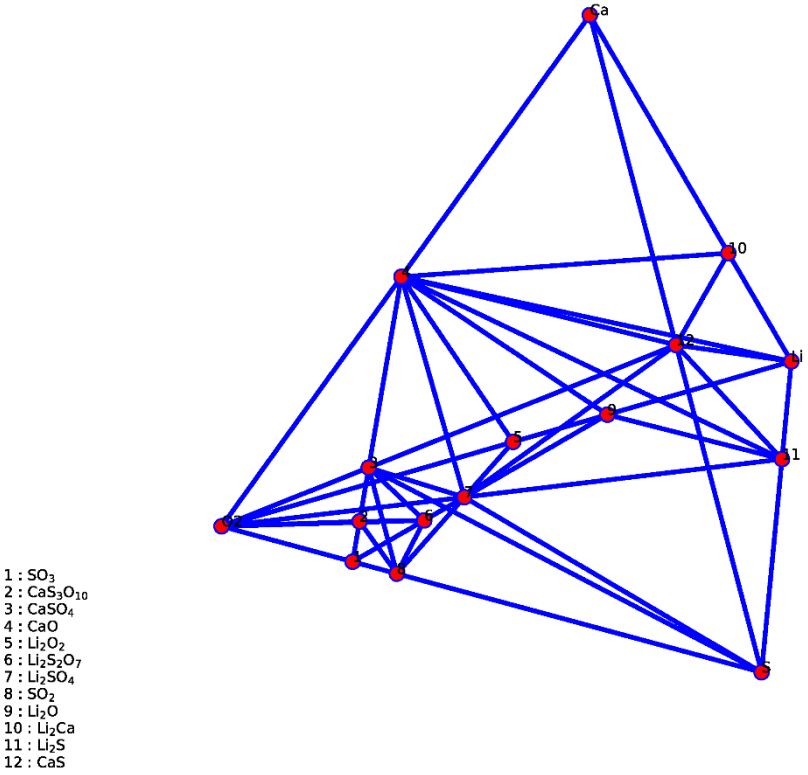

S.i.1: Phase Diagram of Li_2CaOS. All phases are known stable compounds with a composition formed of the components of the target material (Li-Ca-O-S). E_{Hull} for Li_2CaOS was 69 meV/atom with decomposition into Li_2S and CaO.

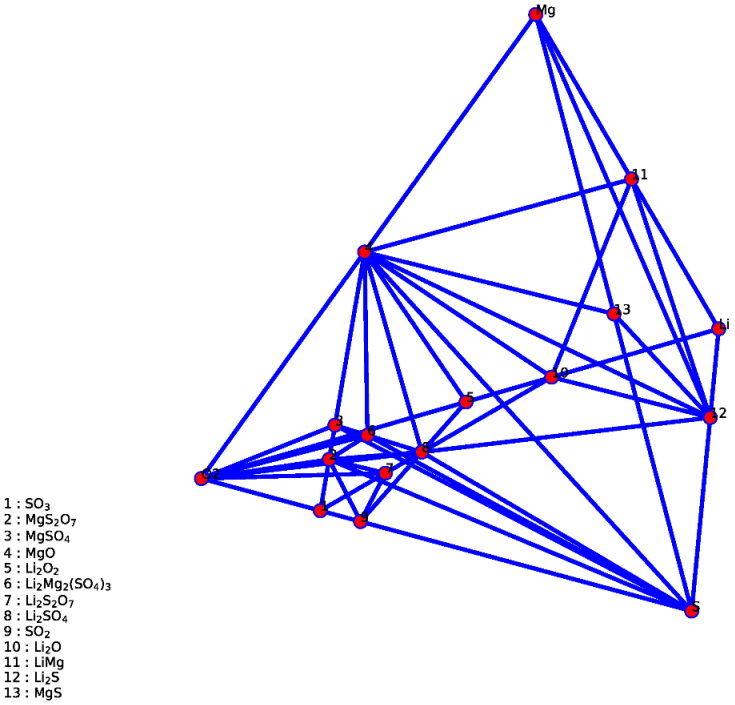

S.i.2: Phase Diagram of Li_2MgOS. All phases are known stable compounds with a composition formed of the components of the target material (Li-Mg-O-S). E_{Hull} for Li_2MgOS was 122 meV/atom with decomposition into Li_2S and MgO.

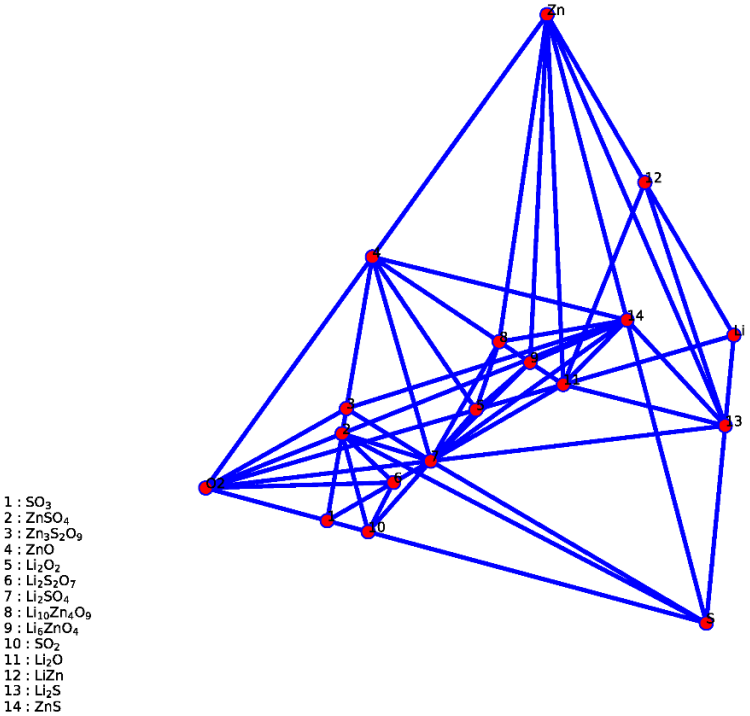

S.i.3: Phase Diagram of Li_2ZnOS. All phases are known stable compounds with a composition formed of the components of the target material (Li-Zn-O-S). E_{Hull} for Li_2ZnOS was 60 meV/atom with decomposition into Li_2O and ZnS.

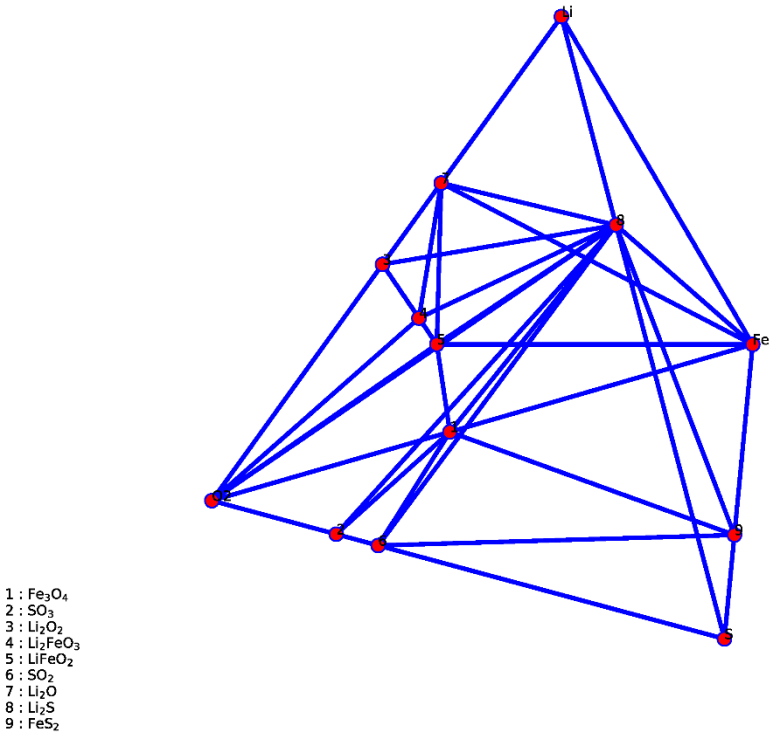

S.i.4: Phase Diagram of Li_2FeOS. All phases are known stable compounds with a composition formed of the components of the target material (Li-Fe-O-S). E_{Hull} for Li_2FeOS was 21 meV/atom with decomposition into Fe_2O_3, Fe and Li_2S.

S.I. Table 1: Formation Energy Comparison to ElemNet Formation Energy.

Composition	Formation Energy (eV/atom)	ElemNet Formation Energy (eV/atom) *
Li_3SF	-1.704	-1.750
Li_3SeF	-1.541	-1.776
Li_2S	-1.353	-1.454
Li_2Se	-1.272	-1.278
LiF	-3.055	-2.972
LiOH	-2.307	-1.630
Li_2O	-2.045	-1.948
Li_2FeOS	-1.332	-1.748
Li_2MgOS	-2.580	-1.945
Li_2CaOS	-2.495	-2.031
Li_2ZnOS	-1.383	-1.763
MgO	-2.721	-3.038
CaO	-2.964	-3.146
ZnS	-0.809	-0.941
Fe_2O_3	-1.275	-1.569

* = Data from Agrawal, A., Meredig, B., Wolverton, C. & Choudhary, A. A Formation Energy Predictor for Crystalline Materials Using Ensemble Data Mining. in *2016 IEEE 16th International Conference on Data Mining Workshops (ICDMW)* 1276–1279 (IEEE, 2016). doi:10.1109/ICDMW.2016.0183

Chapter 4: Investigation of the relative stability of $Na_2Fe_2OS_2$ a new oxysulphide cathode material

Contribution

All computational work that was carried out in this section was performed by R. E. Morris with support from M. S. Dyer. Experimental work which included the synthesis and characterisation of the $Na_2Fe_2OS_2$ target material along with the experimental report given in this paper [1], was performed by Jacinthe Gamon and Arnaud J. Perez.

4.1. Introduction

With increasing demand for development of new battery technologies to replace more traditional fossil fuel reliant energy production, there is an emphasis on improving all components to the battery cell. This includes development of an improved material to be used as a cathode. Many factors are considered whilst identifying a new material, one of which is the relative abundance of the material globally. When considering this, Na-ion technologies are an ideal candidate for further developing lower energy density storage technology due to its abundance. Na has an upper continental crust abundance (ucca) of 2.567 wt% relative to Li which has a ucca of 0.0022 wt%.[2]

Na ion battery cathode technologies currently include transition metal oxides, transition metal fluorides, polyanion compounds and chalcogenides. In layered-structured sodium transition metal oxides, they are most commonly found to be Na_xMO_{2+y} ($0<x\leq1$, $-0.25\leq y\leq 0.25$). As a result of the ionic radius of Na, the ions occupy 6-fold co-ordinated sites as opposed to lithium which can occupy both octahedral and tetrahedral sites. C Delmas et al. [3] suggested that layered oxides are classified into separate classifications which constitutes of O2, O3, P2 and P3. These classifications represent the structures where the letter O, identifies the Na ions occupying the octahedral sites surrounded by 6 O^{2-} ions, and the letter P, identifies the Na ions occupying a central position of prism sites surrounded by 6

O^{2-} ions. The numeric representation in the O2, O3, P2 and P3 classification identifies the packing type of the O ion as prismatic or octahedral layers within the cell.

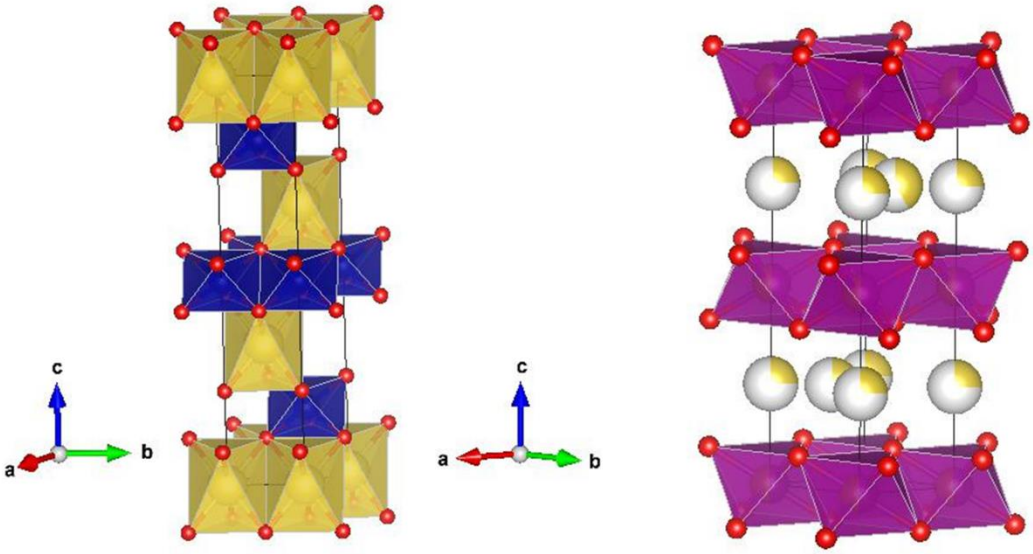

Figure 4.1. Left: O-Type $NaCoO_2$ (ICSD 96428 [4]).Yellow polyhedral consist of 6-fold co-ordinated Na^+ atom (yellow) with red O^{2-} atoms, blue polyhedral consist of 6-fold co-ordinated Co^{3+} atom (blue) with red O^{2-} atoms. Right: P-Type $Na(Fe_{0.5}Mn_{0.5})O_2$ (ICSD 231006 [5]). Purple polyhedral consist of a 6-fold co-ordinated shared occupancy site of Fe^{3+} atoms (brown) with Mn^{3+} atoms (purple) which are co-ordinated with red O^{2-} atoms. Purple polyhedral are separated by a partial occupied Na^+ atom (yellow) layer.

Delmas et al. [6] was amongst the first to study O-type cathodes in the early 1980s for use in Sodium Ion Batteries (SIBs) with their study on the Na_xCoO_2 ($0.5 \leq x \leq 1$) structure, unfortunately Co presents a problem in its' use in SIBs as the relative abundance of Co, which has a ucca of 0.0012% wt% [2], is low, making it cost inefficient for widescale use globally. $NaNi_{0.5}Mn_{0.5}O_2$ which was first studied by Komaba et al. [7], was one alternative O-type cathode which has a higher material abundance compared to Co. This cathode material is considered to be a potential candidate due to it showing a reversible capacity of 185 mAh g^{-1} in the potential region of 2.5-4.5 V. Doping studies have also been carried out to further improve the cycling rate and stability capability, for example, Mg doping into $NaMn_{0.5}Ni_{0.2}Fe_{0.3}O_2$ was carried out by Liu et al. [8]. They found that doping the O-type layered oxide with Mg substituting Mn, enlarged the interlayer spacing consequently improving Na^+ diffusion and rate capability but also reduces lattice strains induced by Na^+ intercalation/deintercalation, that the TM-O bond shrinks which enhances layered structure stability and that the doping with Mg mitigates structural distortion/volume change.

P-type cathodes studied include $Na_{2/3}[Fe_{1/2}Mn_{1/2}]O_2$, which achieved a reversible capacity of 190 mAh g^{-1} with an average voltage of 2.75 V versus Na metal, the energy density was found to be 520 mWh g^{-1} this study was carried out by Komaba et al. [9] Layered oxides are known to suffer from a decreasing capacity, in P-type cathodes, cation substitution has been studied to resolve this limitation, such as the study carrier out by Yang et al.[10] on $Na_{0.66}Ni_{0.33-x}Zn_xMn_{0.67}O_2$ where Zn substitution was introduced to suppress Na^+/vacancy ordering, they also found that Zn substitution improved the voltage and capacity retention significantly.

Polyanion SIB cathode materials studied consist of olivine $NaFePO_4$, NASICON, $Na_3V_2(PO_4)_3$, NASICON $Na_{3+y}M_{2-x}M'_x(PO_4)_3$ and transition metal fluorides. The $NaFePO_4$ olivine has been studied as a cathode for SIBs, nanostructured $NaFePO_4$ was found to be electrochemically active as opposed to the stable maricite phase of the compound, the active nanostructure has a highly active amorphous phase, achieving a high reversible capacity of 145mAh g^{-1} at 0.2°C, and a high cyclic stability of roughly 89% capacity retention over 6300 cycles) [11]. $NaFePO_4$ has also been successfully synthesised in other studies using various methods such as ion substitution using chemical and electrochemical substitution of Li with Na [12–14]. NASICONS have also been studied, $Na_3V_2(PO_4)_3$ in particular, however, the conductivity of $Na_3V_2(PO_4)_3$ was found to be low hence the material has poor cycling performance and low reversible capacity [15]. To resolve this, methods have been employed such as using a carbon framework to wrap the $Na_3V_2(PO_4)_3$ material. Cao et al. [16] employed this method and found by wrapping $Na_3V_2(PO_4)_3$ with a carbon framework, the reversible capacity achieved is 115 mAh g^{-1} and a long cycling stability of 54% capacity retention after 20,000 cycles.

Transition metal fluorides are another type of polyanion materials studied as potential SIB cathode materials. Reported enhancement of the operating voltage as a result of the increase in ionicity of the M-F bond can be achieved by introducing F^- ions, this is demonstrated by the study on the polyanionic sodium vanadium fluorophosphates, $Na_3(VO_{1-x}PO_4)_2F_{1+2x}$ ($0 \leq x \leq 1$) which was carried out by Ceder et al.[17] In this study they found that the sodium vanadium fluorophosphates had a high energy density of roughly 500 Wh kg^{-1}, $Na_3V_2(PO_4)_2FO_2$ has a reversible capacity of 120 mAh g^{-1} and $Na_3V_2(PO_4)F_3$ was found to have a reversible capacity of 110mAh g^{-1}.

Oxychalcogenides have also been considered viable candidates for cathode materials, such as $Na_2Fe_2OSe_2$, which was first reported by J. He et al. [18] as a new layered iron oxychalcogenide, it was reported for its interesting magnetic and electronic properties. It has a reported theoretical capacity of 162mAh g^{-1} and due to its layered structure with a high amount of Na, a good conductivity should be seen in the Fe_2O layer. It has an anti-Ruddlesden-Popper structure with an anti-ferromagnetic (AFM) arrangement of the Fe^{2+} atoms, examples of which can be seen in **Figure 4.3**. Studies have been carried out to identify magnetic orderings in oxychalcogenides, such as a study carried out by Lee et al

[19] where the $A_2Fe_2OQ_2$ (A= Sr, Ba; Q= S, Se) system was studied. DFT calculations used to identify the magnetic ordering of the structure found that a checkerboard type AFM was favoured. More recently, computational searches have been performed in the iron based oxysulphide field to identify new cathode materials such as Zhu and Scanlon et al [20], where they find new oxychalcogenides, but also identify a series of known oxychalcogenides which are considered stable and metastable in their searches.

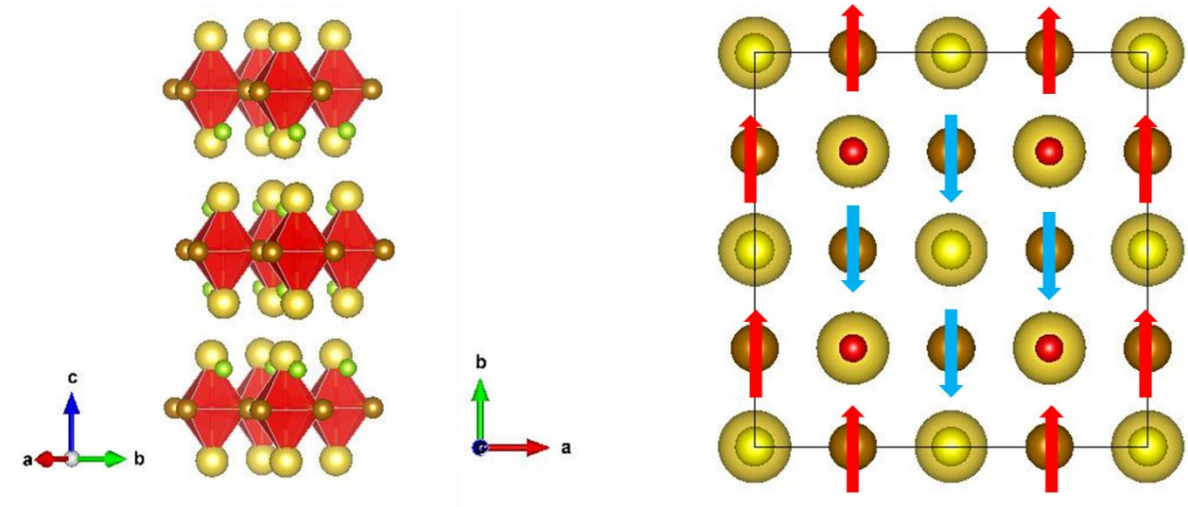

Figure 4.2. Left: $Na_2Fe_2OSe_2$ (ICSD 186502 [18]. Right: Blocked Checkerboard Ordered $Na_2Fe_2OSe_2$ [21]. Yellow atoms are Na^+, brown atoms are Fe^{2+}, red atoms are O^{2-}, and green atoms are Se^{2-}. The Red and blue arrows represent different magnetic orderings of up and down spins.

In this study we explore $Na_2Fe_2OS_2$ by initially carrying out a convex hull calculation to identify the relative stability of $Na_2Fe_2OS_2$ relative to its phase field. We then identified the magnetic arrangement of the structure by carrying out magnetic stability calculations, using a series of various arrangements consisting of non-magnetic (NM), ferromagnetic (FM) and anti-ferromagnetic (AFM). The anti-ferromagnetic arrangements are split into three different AFM arrangements. We also calculated and plotted the band structure and partial density of states (pDOS) to better understand the electronic properties of $Na_2Fe_2OS_2$. Phonon frequencies were also calculated using PhonoPy [22] to identify imaginary frequencies which will indicate if a true global minimum stability value for the structure was found. The objective of the calculation is to support the experimental synthesis and identification of $Na_2Fe_2OS_2$, carried out by Gammon and Perez et al [1]. **Figure 4.2** shows the structure and blocked-checkerboard AFM arrangement of the Fe^{2+} atoms based on the research carried out by Stadnik et al [21], where they identified the experimental magnetic ordering as blocked-checkerboard for the selenide equivalent through Mössbauer spectroscopy.

4.2. Methods

Band Structure & pDOS of $Na_2Fe_2OS_2$

The band structure and pDOS of the blocked checkerboard anti-ferromagnetic $Na_2Fe_2OS_2$ were calculated using the fully ordered anti-K_2NiF_4 type, Ruddlesden-Popper structure.

Computational Methods

Relaxations. Density functional theory (DFT) calculations were performed using the Vienna ab-initio Simulation Package (VASP) [23] with the PBE+U exchange-correlation functional with a generalized gradient approximation (GGA) [24] and the projector augmented wave approach (PAW) [25]. An energy cutoff of 650 eV is used for the plane-wave basis expansion. The Brillouin zone was sampled by a 6 × 6 × 4 Monkhorst-Pack grid [26]. The break condition for the ionic relaxation loop was selected as 0.01eV. The self-consistence loop's convergence criterion was set as 10^{-5} eV. Energies were minimized using the conjugate gradient algorithm [27].

Magnetic ordering. $Na_2Fe_2OS_2$ was initially studied using the LDA+U Dudarev method [28]. The value of $U_{eff} = U - J$ (where U and J are Coulomb exchange interaction) used in this calculation was 5 eV for Fe. Non-magnetic (NM), ferromagnetic (FM), and three anti-ferromagnetic (AFM) orderings were studied. Anti-ferromagnetic orderings selected were; stripe-like anti-ferromagnetic (AFM1), checkerboard anti-ferromagnetic (AFM2) and blocked checkerboard anti-ferromagnetic (AFM3).

Convex Hull. To calculate the convex hull energy of $Na_2Fe_2OS_2$, the Na-Fe-O-S phase field stability was calculated using thermodynamically stable (E_{Hull} = 0 meV/atom) Na-Fe-O-S compounds from the Inorganic Crystal Structure Database [29], along with the ground state $Na_2Fe_2OS_2$ with a blocked checkerboard ordering. Calculations for phases to form the convex hull were performed at 0 K with the same parameters as stated above with the appropriate LDA+U parameters. Convex hull energy (E_{Hull}) calculations for $Na_2Fe_2OS_2$ were carried out using Pymatgen software [30]. This was done by performing relaxations on all competing phases for a given target material and creating a convex hull from their total ground state energies (TGSE).

Band Structures and pDOS. Electronic band structures and partial density of states were calculated for all fully ordered $Na_2Fe_2OS_2$ magnetic orderings. pDOS for all AFM1 and AFM2 orderings can be found in S.I 1 and 2. Calculations were performed using similar parameters as listed in the relaxation calculations but performed as non-self-consistent calculations (non-SC).

4.3. Results

$Na_2Fe_2OS_2$ Convex Hull Energy

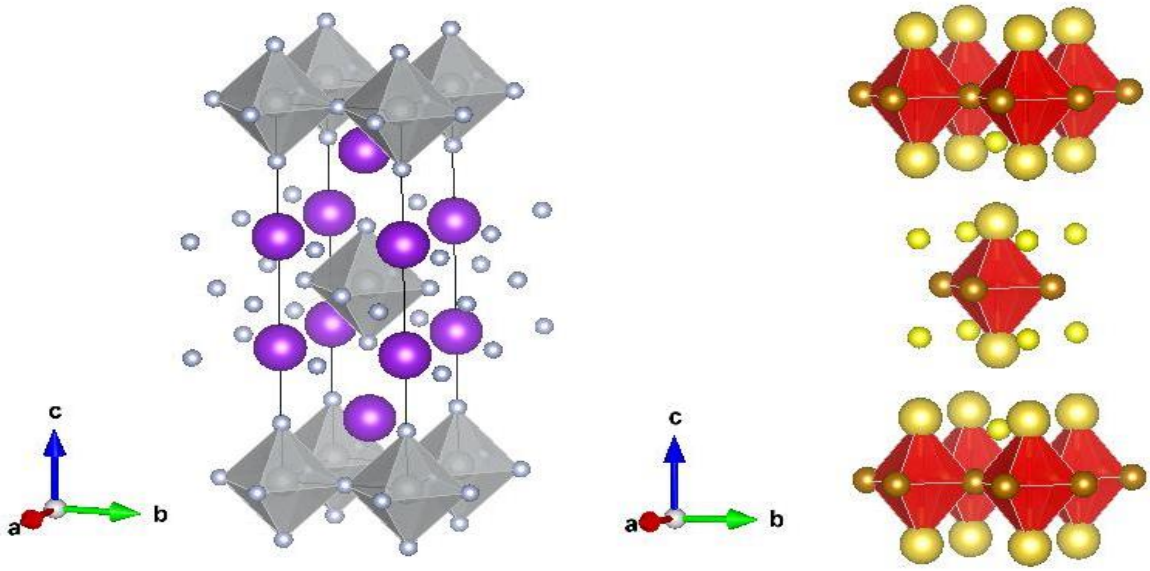

Figure 4.3. Anti-Ruddlesden-Popper left: K_2NiF_4 (ICSD 73450 [31]) . Grey polyhedra consist of a six-fold co-ordinate Ni^{2+} atom with small light-grey F^- atoms, large purple atoms are K^+. Right: $Na_2Fe_2OS_2$ [1]. Large light-yellow atoms are Na^+, brown atoms are Fe^{2+}, red atoms are O^{2-}, and small yellow atoms are S^{2-}.

$Na_2Fe_2OS_2$ is isotypic in comparison to its selenide equivalents [18]. It has an anti-K_2NiF_4 type structure, where K_2NiF_4 belongs to the Ruddlesden-Popper series of structures. Ruddlesden-Popper structures are perovskite structures which consist of layers of perovskite slabs separated with interlayer cations with the general formula of $[AX][ABX_3]_n$. A positions consist of large cations, with B positions occupied by a smaller cation an X by an anion which can be seen in **Figure 4.3** above. For the $Na_2Fe_2OS_2$ structure in this study, the $[ABX_3]$ is an anti-perovskite slab, where the A sites are occupied by a large sulphur atom, the B sites are occupied by an oxygen atom which is co-ordinated to four Fe atoms which are within the same layer, and two Na atoms which are in the layers above and below. The anti-rocksalt layer [AX] for $Na_2Fe_2OS_2$ is $[SNa]^-$ and the anti-perovskite slab (layer) $[ABX_3]$ for the structure in this study is $[SO(Fe_2Na)]^+$. Another structural description of this $Na_2Fe_2OS_2$ structure consists of a double Na layer, $[Na_2]^{2+}$, followed by a layer of $[Fe_2OS_2]^{2-}$, this formation would then repeat.

The atoms within the structure consist of multiple environments. For the Fe atoms, they are positioned in an octahedral site, where they are co-ordinated by four S atoms which are positioned above and

below the square planar layer (*ac* plane), the square planar layer (anti-[CuO_2] type) is constructed of two O atoms co-ordinating to the Fe atom. Oxygen atoms are therefore octahedrally co-ordinated by four Fe atoms in the *ab* plane, and two Na atoms along the *c* axis. The Na atoms are co-ordinated in a distorted octahedral position, where Na is co-ordinated with a short Na-O distance along the *c* axis, a short Na-S co-ordination along the *c* axis and four long Na-S co-ordination distances distorted towards the *c* axis on the *ab* plane. S is co-ordinated with 5 Na atoms, 1 along the *c* axis and 4 on the same *ab* plane, however, the S atom is distorted away from its *ab* layer along the *c* axis towards the closest Fe_2O layer.

The convex hull energy calculated for the non-magnetic structure of $Na_2Fe_2OS_2$ was significantly over the hull, with an energy of 623 meV/atom over the hull. For an accurate identification of the true convex hull energy of $Na_2Fe_2OS_2$, a more thorough investigation of the magnetic ordering was required.

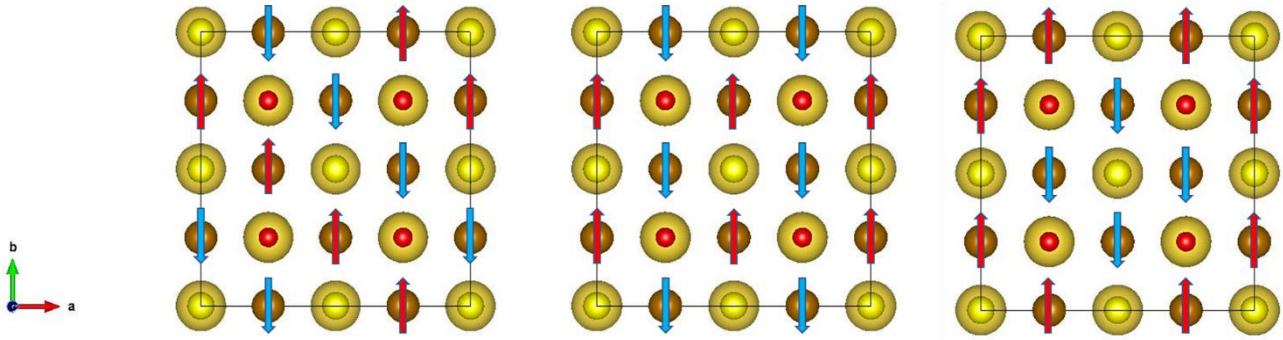

Figure 4.4. $Na_2Fe_2OS_2$ Anti-ferromagnetic Ordering. Left: AFM1, Middle: AFM2, Right: AFM3. Yellow atoms are Na^+, brown atoms are Fe^{2+}, red atoms are O^{2-}. The Red and blue arrows represent different magnetic orderings of up and down spins.

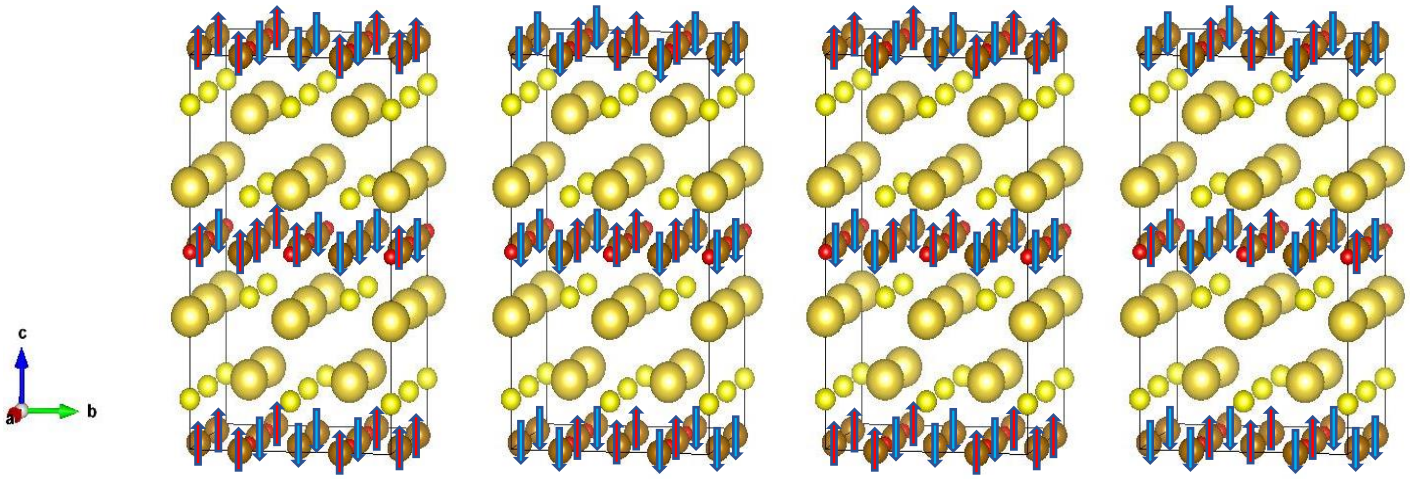

Figure 4.5. $Na_2Fe_2OS_2$ Layered Anti-ferromagnetic Ordering. Left: AFM3, Center-Left: AFM3-Aligned, Center-Right: AFM3-Alternating, Right: AFM3-Orthorhombic-Distribution.

Magnetic orderings for the structure at the Fe_2O layer was carried out using 8 different magnetic orderings, which consisted of non-ferromagnetic (NM), ferromagnetic (FM) and 6 different anti-ferromagnetic orderings, AFM1 **Fig 4 (left)**, AFM2 **Fig 4 (middle)**, AFM3 **Fig 5 (left)**, AFM3-Aligned **Fig 5 (center-left)**, AFM3-Alternating **Fig 5 (center-right)** and AFM3-Ortho **Fig 5 (right)**. Anti-ferromagnetic 1 (AFM1) consists of a stripe-like anti-ferromagnetic state, in which Fe atoms on the *ab* plane have alternating spins in rows which are perpendicular to the *b* axis (Fe atoms along rows are anti-ferromagnetic relative to each other). Anti-ferromagnetic 2 (AFM2) consists of a checkerboard anti-ferromagnetic state, where all Fe atoms along the rows perpendicular to the *b* axis are ferromagnetic (all the same spin) and alternating rows are anti-ferromagnetic (opposite spin). Anti-ferromagnetic 3 (AFM3) consists of a blocked-checkerboard anti-ferromagnetic state, where an initial row of Fe atoms perpendicular to the *b* axis are all ferromagnetic (same spin) and the following row along the *b* axis consists of alternating spins on Fe atoms which are anti-. The AFM3 variations consist of variance in AFM3 ordering on alternating layers along the *c* axis. AFM3-Aligned consists of AFM3 layers which are ferromagnetic in relation to the *c* axis layers, AFM3-Alternating consists of AFM3 layers which are anti-ferromagnetic in relation to the *c* axis layers, and AFM3-Ortho where an orthorhombic distribution of blocked checkerboard ordering is seen, where the usual blocked checkerboard layer of rows of ferromagnetically ordered Fe atoms alternate with anti-ferromagnetically ordered Fe atoms, are layered between a layer of Fe atoms where the rows consist of a ferromagnetically ordered row, alternating with two sequential antiferromagnetic rows. The orderings used are similar to those in a study on the magnetic ordering of $Na_2Fe_2OSe_2$ by Stadnik et al [21].

Magnetic Ordering	Energy Above Hull (meV/atom)	Total Ground State Energy (meV/atom)
Non-Magnetic (NM)	623	-4.407
Ferromagnetic (FM)	15	-5.016
Anti-ferromagnetic 1 (AFM1)	1	-5.029
Anti-ferromagnetic 2 (AFM2)	3	-5.027
Anti-ferromagnetic 3 (AFM3)	0	-5.030
Anti-ferromagnetic 3 Aligned (AFM3-Aligned)	5	-5.025
Anti-ferromagnetic 3 Alternating (AFM3-Alternating)	5	-5.025
Anti-ferromagnetic 3 Distorted Orthorhombic (AFM3-Ortho)	5	-5.026
Broken Symmetry 1	0	-5.030
Broken Symmetry 2	0	-5.030

Table 4.1. Convex Hull energies and Total Ground State Energies of $Na_2Fe_2OSe_2$ with varying magnetic ordering.

From the magnetic orderings studied, all structures are considered metastable except for the non-magnetic calculation. The most stable magnetic ordering found for $Na_2Fe_2OS_2$ is the AFM3 blocked-checkerboard ordering with an energy above the hull of 0 meV/atom, therefore the AFM3 magnetically ordered structure is considered the stable product forming the convex hull. The broken symmetry structures had almost identical total ground state energies to that of the original AFM3

structure, with a slight increase in energy at the meV/atom level, this is due to the structures relaxing back to the higher symmetry structure.

$Na_2Fe_2OS_2$ Bandstructure, Bandgap, pDOS and Phonon Frequency

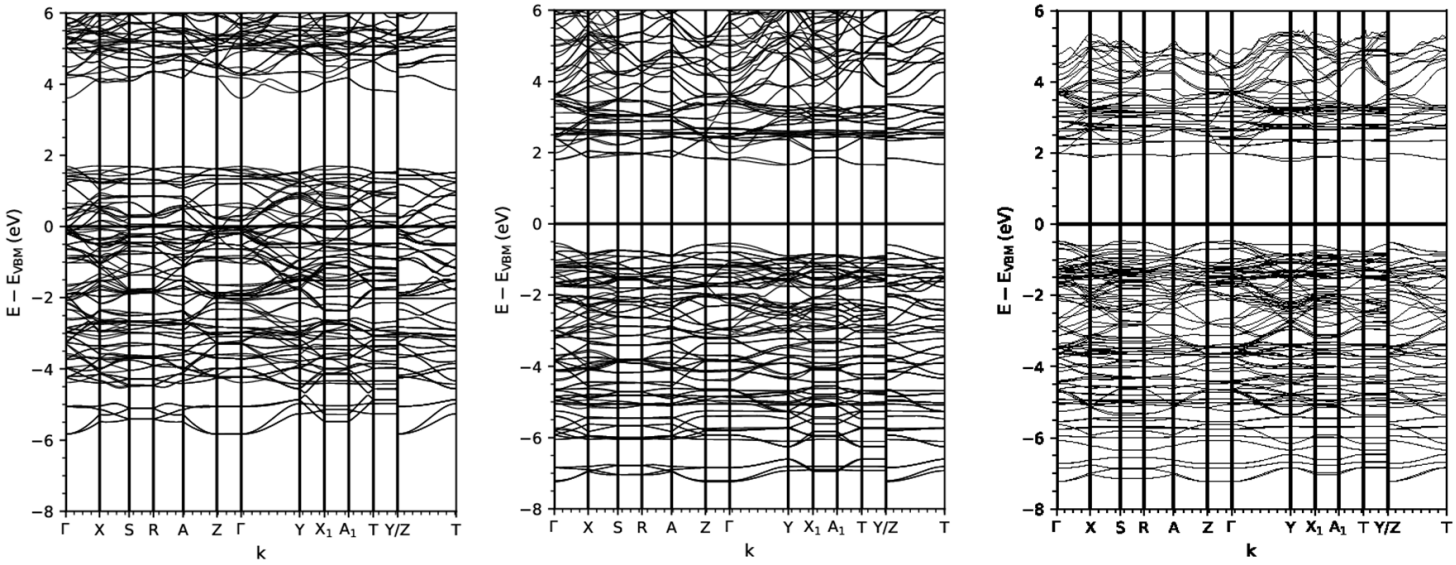

Figure 4.6. Bandstructure plots for: *Left (a): NM, Middle (b): FM, Right (c): AFM3.*

The bandstructures of NM, FM and AFM3 are all displayed above in **Figure 4.6**. The NM ordering bandstructure **Figure 4.6 (a)**, shows that there is a clear absence of a bandgap at the Fermi level, which leads to the indication that the structure is metallic-like in nature. A bandgap can be seen of roughly 1.8 eV above the Fermi level for the NM structure. In the FM ordered structure, **Figure 4.6 (b)**, the band gap extends to roughly 2.2 eV with an absence of bands at the Fermi level. The maximum valence band can be seen at 0.5 eV below the Fermi level and a maximum conduction band at 1.7 eV above the Fermi level. The band gap in the ferromagnetic ordered structure indirectly allows for interband transitions when considering energies larger than 2.2 eV from the Γ to Y direction. In the AFM3 ordered structure **Figure 4.6 (c)**, the band gap extends to 2.15 eV with the maximum conduction band at 1.75 eV above the Fermi level, and the maximum valence band at roughly 0.4 eV below the Fermi level. The valence band maximum consists of Fe d states and S states, and the

conduction band consists of Fe d states with O states as shown in the projected DOS in **figure 4.7**. The more electronegative O states are lower in the valence band than the S states.

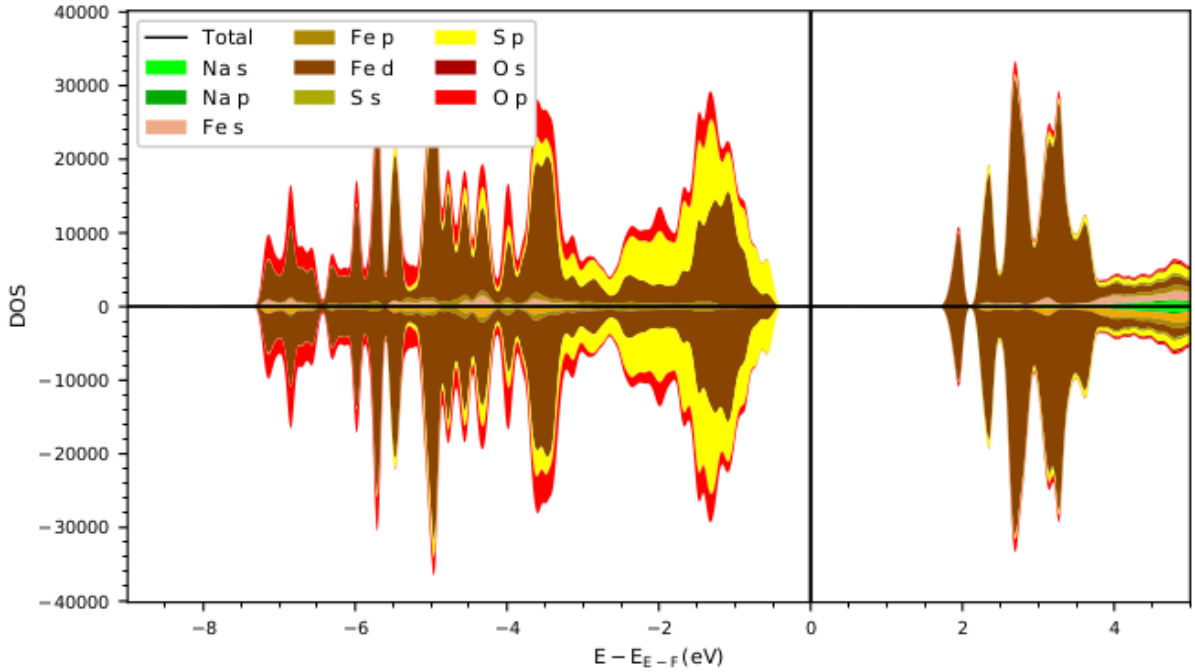

Figure 4.7. pDOS plot for $Na_2Fe_2OS_2$ *AFM3 blocked checkerboard.*

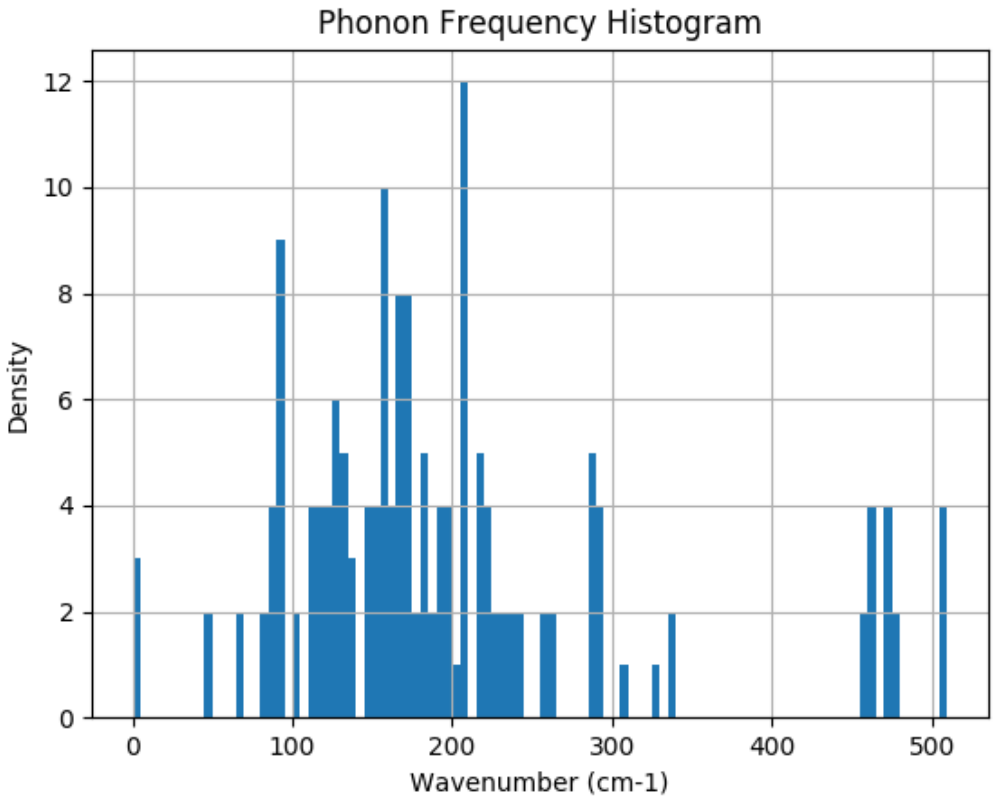

Figure 4.8. Phonon Frequency plot for AFM3 Ordered $Na_2Fe_2OS_2$.

Phonon frequencies calculated for the AFM3 ordered structure identified three very small imaginary frequencies from the three translational modes, which is expected for a stable structure.

4.4. Discussion

For $Na_2Fe_2OS_2$, the energetic variance in terms of convex hull energy between magnetic orderings is relatively low, with a difference of only 15 meV/atom between the most stable ordering, blocked checkerboard (AFM3), and the least stable, the ferromagnetic ordering (FM). The non-magnetic structure has a significant increase in E_{hull} of over 620 meV/atom compared to the stable AFM3 structure. This comes as no surprise as magnetic interaction of the Fe atom within the structure has a significant contribution to the stability of the structure. The ordering difference of AFM1, AFM2 and AFM3 leads to only a slight variance in energy, of 1, 3 and 0 meV/atom over the hull respectively, indicating that whilst the magnetic ordering certainly does have an impact in relation to stability, the anti-ferromagnetic ordering only leads to a small energetic change for a given layer. The difference in energy found when varying the AFM3 ordering between layers is minimal. From four variations of the ordering between layers AFM3, AFM3-Alternating, AFM3-Aligned, AFM3-Orthorhombic-Distribution (AFM3-ortho-dist) there is a difference of 5 meV/atom between the most stable layer arrangement of AFM3 (0 meV/atom) and AFM3-ortho-dist (5 meV/atom), although it can be seen that AFM3-Alternating and AFM3-ortho-dist both have energies over the hull of 5 meV/atom and with AFM3-aligned with an energy over the hull of 4.7 meV/atom. This indicates that varying the magnetic ordering between layers does not lead to a significant change in stability, although the AFM3 ordering shown in **Figure 4.5** is the most stable ordering. The phonon frequency plotted in **Figure 4.8** also demonstrates that the AFM3 ordered structure is stable, in the frequency values given, only 3 were considered imaginary, which indicates stability.

The bandstructure shows a clear bandgap within the -0.5 to 2 eV region with a band gap of roughly 2.15 eV. A conduction band minimum can be seen at the Γ to Y direction with a valence band maximum at the same space. In comparison to bandstructures studied on the $Na_2Fe_2OSe_2$ by Stadnik et al [21], a larger bandgap can be seen in the $Na_2Fe_2OS_2$ which is to be expected. Empty Se states are lower in energy in comparison to the empty S states, therefore a larger bandgap is observed with the inclusion of the S atoms within the structure. When looking at the pDOS plots in **Figure 4.7**, in the AFM3 structure, the unoccupied conduction band is formed of Fe d states, the occupied valence band

consists of S p states where the lower energy occupied O p states are seen more dominant in the lower energy region of the pDOS.

4.5. Conclusion

In this study, we have reported on the stability of $Na_2Fe_2OS_2$ using convex hull energy calculations using the Pymatgen software. We also identified the most stable magnetic ordering on the structure using a series of various magnetic orderings. Bandstructure, bandgap and phonon frequency calculations were carried out and bandstructure, pDOS and phonon frequency plots were generated from the calculations. The purpose of the study was to investigate the stability and magnetic ordering of the $Na_2Fe_2OS_2$ structure to support the development of the structure for its use as a cathode material. Initial convex hull energy calculations identified the non-magnetic structure to be significantly over the hull. Magnetic ordering calculations found the structure to be much more stable, as expected, with the most optimal magnetic ordering found to be the blocked-checkerboard magnetic arrangement (AFM3) with an energy over the hull of 0 meV/atom, identifying the structure to be classified as a stable structure. Bandstructure, bandgap, pDOS and phonon frequencies for all magnetic orderings were calculated and plotted identifying the interaction of states within the structure.

4.6. References

1 J. Gamon, A. J. Perez, L. A. H. Jones, M. Zanella, L. M. Daniels, R. E. Morris, C. C. Tang, T. D. Veal, L. J. Hardwick, M. S. Dyer, J. B. Claridge and M. J. Rosseinsky, *J. Mater. Chem. A*, 2020, **8**, 20553–20569.

2 A. A. Yaroshevsky, *Geochemistry Int.*, 2006, **44**, 48–55.

3 C. Delmas, C. Fouassier and P. Hagenmuller, *Phys. B+C*, 1980, **99**, 81–85.

4 Y. Takahashi, Y. Gotoh and J. Akimoto, *J. Solid State Chem.*, 2003, **172**, 22–26.

5 B. Mortemard De Boisse, D. Carlier, M. Guignard, E. Guerin, M. Duttine, A. Wattiaux and C. Delmas, *Chem. Mater.*, 2018, **30**, 7672–7681.

6 C. Delmas, J. Braconnier, C. Fouassier and P. Hagenmuller, *Solid State Ionics*, 1981, **3**–**4**, 165–169.

7 S. Komaba, T. Nakayama, A. Ogata, T. Shimizu, C. Takei, S. Takada, A. Hokura and I. Nakai, *ECS Trans.*, 2019, **16**, 43–55.

8 C. Zhang, R. Gao, L. Zheng, Y. Hao and X. Liu, *ACS Appl. Mater. Interfaces*, 2018, **10**, 10819–10827.

9 N. Yabuuchi, M. Kajiyama, J. Iwatate, H. Nishikawa, S. Hitomi, R. Okuyama, R. Usui, Y. Yamada and S. Komaba, *Nat. Mater.*, 2012, **11**, 512–517.

10 X. Wu, J. Guo, D. Wang, G. Zhong, M. J. McDonald and Y. Yang, *J. Power Sources*, 2015, **281**, 18–26.

11 Y. Liu, N. Zhang, F. Wang, X. Liu, L. Jiao and L.-Z. Fan, *Adv. Funct. Mater.*, 2018, **28**, 1801917.

12 W. Tang, X. Song, Y. Du, C. Peng, M. Lin, S. Xi, B. Tian, J. Zheng, Y. Wu, F. Pan and K. P. Loh, *J. Mater. Chem. A*, 2016, **4**, 4882–4892.

13 Y. Fang, Q. Liu, L. Xiao, X. Ai, H. Yang and Y. Cao, *ACS Appl. Mater. Interfaces*, 2015, **7**, 17977–17984.

14 Y. Zhu, Y. Xu, Y. Liu, C. Luo and C. Wang, *Nanoscale*, 2013, **5**, 780–787.

15 Y. Lyu, Y. Liu, Z.-E. Yu, N. Su, Y. Liu, W. Li, Q. Li, B. Guo and B. Liu, *Sustain. Mater. Technol.*, 2019, **21**, e00098.

16 Y. Fang, L. Xiao, X. Ai, Y. Cao and H. Yang, *Adv. Mater.*, 2015, **27**, 5895–5900.

17 M. Bianchini, P. Xiao, Y. Wang and G. Ceder, *Adv. Energy Mater.*, 2017, **7**, 1700514.

18 J. B. He, D. M. Wang, H. L. Shi, H. X. Yang, J. Q. Li and G. F. Chen, *Phys. Rev. B*, 2011, **84**, 205212.

19 H. Kabbour, E. Janod, B. Corraze, M. Danot, C. Lee, M.-H. Whangbo and L. Cario, *J. Am. Chem. Soc.*, 2008, **130**, 8261–8270.

20 B. Zhu and D. O. Scanlon, *ACS Appl. Energy Mater.*, 2022, **5**, 575–584.

21 F. Nejadsattari, Z. M. Stadnik and J. Żukrowski, *J. Alloys Compd.*, 2015, **639**, 547–555.

22 L. Chaput, A. Togo, I. Tanaka and G. Hug, *Phys. Rev. B*, 2011, **84**, 094302.

23 G. Kresse and J. Furthmüller, *Phys. Rev. B*, 1996, **54**, 11169–11186.

24 J. P. Perdew, K. Burke and M. Ernzerhof, *Phys. Rev. Lett.*, 1996, **77**, 3865–3868.

25 P. E. Blöchl, *Phys. Rev. B*, 1994, **50**, 17953–17979.

26 H. J. Monkhorst and J. D. Pack, *Phys. Rev. B*, 1976, **13**, 5188–5192.

27 M. C. Payne, M. P. Teter, D. C. Allan, T. A. Arias and J. D. Joannopouios, *Rev. Mod. Phys.*, 1992, **64**, 1045–1097.

28 S. Dudarev and G. Botton, *Phys. Rev. B - Condens. Matter Mater. Phys.*, 1998, **57**, 1505–1509.

29 A. Belkly, M. Helderman, V. L. Karen and P. Ulkch, *Acta Crystallogr. Sect. B Struct. Sci.*, 2002, **58**, 364–369.

30 S. P. Ong, W. D. Richards, A. Jain, G. Hautier, M. Kocher, S. Cholia, D. Gunter, V. L. Chevrier, K. A. Persson and G. Ceder, *Comput. Mater. Sci.*, 2013, **68**, 314–319.

31 E. A. Zhurova, Y. Ivanov, V. Zavodnik and V. Tsirelson, *Acta Crystallogr. Sect. B Struct. Sci.*, 2000, **56**, 594–600.

4.7. Supporting Information

S.I 1 - $Na_2Fe_2OS_2$ AFM 1 Bandstructure & pDOS

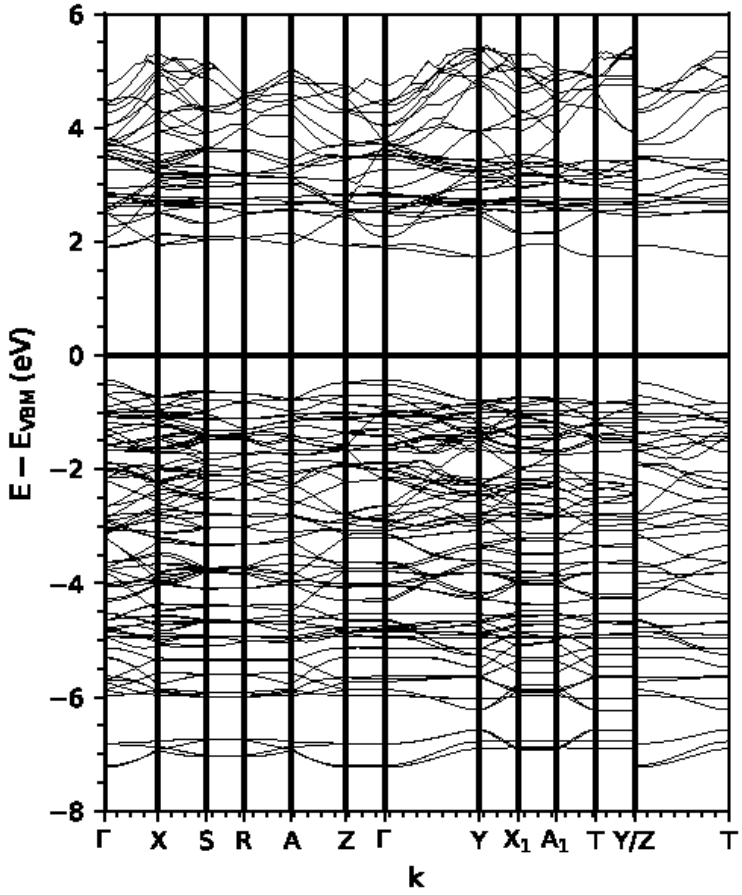

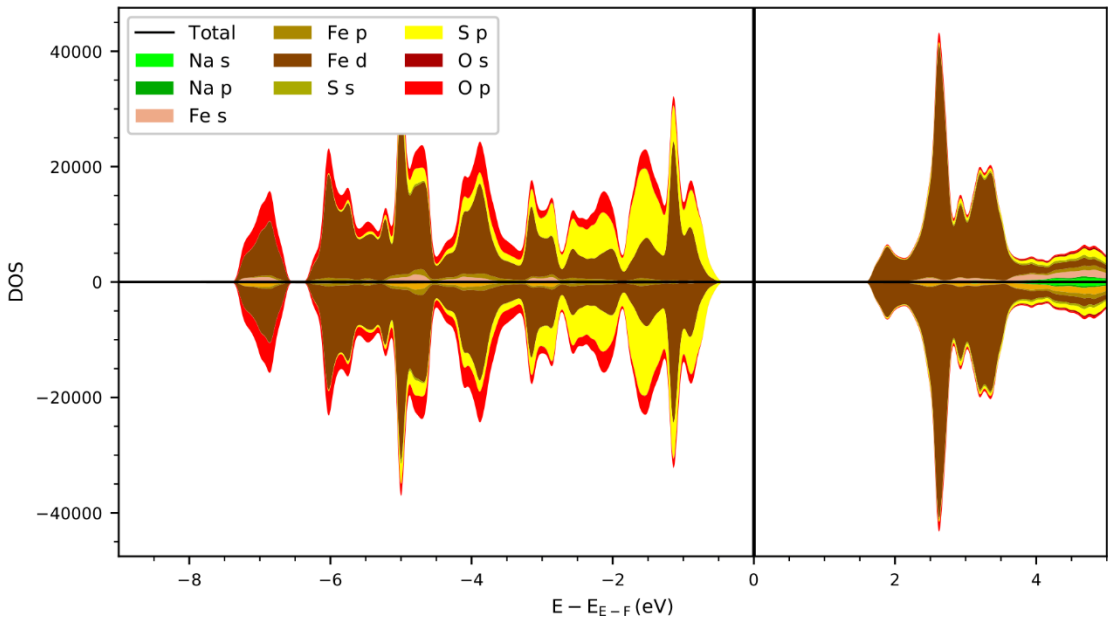

S.I 2 - $Na_2Fe_2OS_2$ AFM 2 Bandstructure & pDOS

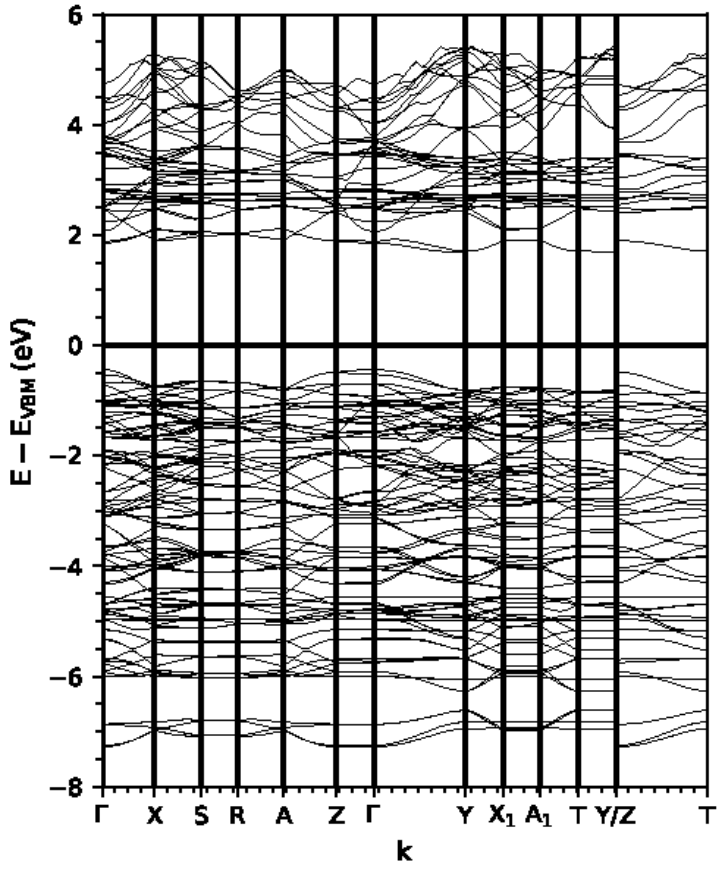

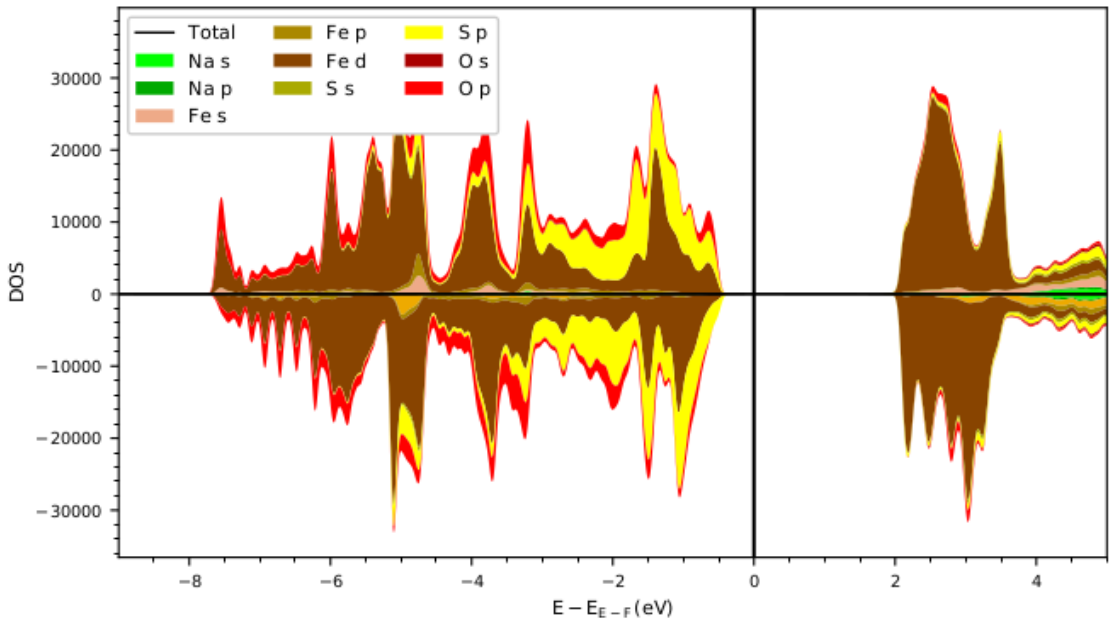

S.I. 2 – Convex Hull Relaxation Data0

Structure	Magnetic ordering	TGSE (eV)	Energy/Atom (eV/atom)	Ehull (meV)
Na		-26.034	-1.302	0.0
O		-79.174	-4.948	0.0
Fe		-10.485	-5.243	0.0
S		-132.086	-4.128	0.0
FeS	Troilite	-128.148	-5.339	0.0
FeS	Mackinawite	-20.943	-5.236	103.8
FeS2		-28.747	-4.791	144.3
Na3Fe2S4		-158.507	-4.403	0.0
Na7Fe2S6		-179.611	-3.991	0.0
Na2FeS2		-85.091	-4.255	0.0
NaFe(SO4)2		-147.108	-6.129	0.0
Na8Fe2O7		-328.094	-4.825	0.0
Fe2(SO4)3		-644.873	-6.322	0.0
Fe2O3		-206.081	-6.869	0.0
FeO		-416.842	-6.513	152.9
Fe3O4		-384.690	-6.869	0.0
FeSO4	Beta-FM	-154.922	-6.455	0.0
Na2FeO3	AFM2	-128.108	-5.338	0.0
Na3FeO3	AFM1	-282.608	-5.047	0.0
NaF3Fe(SO4)3	AFM1	-677.821	-5.946	0.0
Na4FeO4		-702.046	-4.875	0.0
Na5FeO4	AFM1	-373.355	-4.667	0.0
NaFeO2		-70.599	-7.844	0.0
Na2O		-44.919	-3.743	0.0
Na2O2		-50.470	-4.206	0.0
Na2S		-39.906	-3.325	0.0
Na2S2O7		-126.859	-5.766	0.0
Na2S5		-106.990	-3.821	4.7
Na2SO4		-314.507	-5.616	0.0
Na6S2O7		-360.795	-5.306	0.0
NaO2		-26.908	-4.485	0.0
NaS		-28.431	-3.554	0.0
NaS2		-181.219	-3.775	0.0
S8O		-156.278	-4.341	55.6
SO2		-68.895	-5.741	0.0
SO3		-278.721	-5.807	0.0
Na2Fe2OS2	NM	-246.812	-4.407	623.0
Na2Fe2OS3	FM	-280.871	-5.016	14.8
Na2Fe2OS4	AFM1	-281.678	-5.030	1.2
Na2Fe2OS5	AFM2	-281.561	-5.028	2.5
Na2Fe2OS6	AFM3	-281.702	-5.030	0.0
Na2Fe2OS7	AFM3-Aligned	-281.439	-5.026	5.0
Na2Fe2OS8	AFM3-Alternating	-281.424	-5.025	4.7
Na2Fe2OS9	AFM-OrthoDist	-281.439	-5.026	5.0
Na2Fe2OS10	AFM3-BrokenSymm1	-281.701	-5.030	0.0
Na2Fe2OS11	AFM3-BrokenSymm2	-281.702	-5.030	0.0

Chapter 5: High Throughput Investigation of the Bond Valence Sum Mismatch Mapping of Potential Solid-State Electrolytes

Contribution

All computational work that was carried out in this section was performed by R. E. Morris with support from M. S. Dyer.

5.1. Introduction

Bond Valence Sum Mismatch mapping has been developed and studied extensively, being employed in many studies [1–4] as a method of analysing the mobile ion migration pathway (diffusion pathway) of conductive compounds. The theory behind the mapping consists of "accessible" mobile ion (A) sites in a local structure model being identifiable via employing empirical relationships between bond length *R* between the mobile-cation and counter-anion, and the bond-valence S_{A-X} [5].

$$S_{A-X} = \exp\left[\frac{(R_0 - R)}{b}\right] \quad (5.1.1)$$

The mobile sites are identified as sites where the mismatch of the bond valence between bond valence summed over all adjacent counter ions (X) and ideal bond valence (V_{id}) approaches zero.

$$|\Delta V(A)| = \sum_x S_{A-X} - V_{id}(A) \quad (5.1.2)$$

Brese and O'Keeffe developed a series of bond valence parameters by an interpolation scheme for a wide range of solid-state ionic combinations. In their study they used the bond valence parameter

constant (*b*) of 0.37 Å [6]. More recently a more intuitive approach has been employed for the bond valence parameter, with implementation of SoftBV parameters developed by Adams et al [1], improving on the original bond valence parameter of 0.37. A more detailed description of the bond valence method can be found in the chapter 2 methods.

The Bond Valence method of analysis for conductors has been extensively used. Adams has frequently used and developed the BV method for the study of a wide array of materials, primarily focusing on conductors, to study structural pathways, conductivity, migration and for high throughput screening [1,2,7–16]. Adams' study on the pathways of crystalline AgI-AgM_xO_y [9] was one of the earlier examples where the BV method was utilized to study the potential of a structure as a conductor by studying the mobile-ion pathway within a cell. One of the studies carried out which progressed the development of using the BV method as a more accurate method of analysis included Adams' study on the relationship between bond valence and bond softness of alkali halides and chalcogenides [1]. As stated above, this study improved on the original bond valence parameter of 0.37 developed by Brese and O'Keefe [6], as it included weak interactions of the second co-ordination shell, hence the bond valence parameter became a variable value dependent on the cation-anion combination. This in turn led to more accurate bond valence mismatch values. Adams also used the improved BV method to study the ion transport pathways of not only cation ion conductors but also anion conductors, i.e. F^- mobility in PbF_2 and LaF_3 [11]. In 2012, Adams used the BV method to carry out a screening method which was capable of handling large datasets [2]. In this particular study, 13,000 structures from the Inorganic Crystal Structure Database (ICSD) [17] were screened for their potential as superionic conductors, this was a step forward in the development of BV as an inexpensive method to study large datasets.

With current development of new conductor materials, there have been many structures which were previously characterised but not studied electrochemically, this leads to a potential of thousands of structures which are potential conductors. This primary issue in exploring this known but unproven field of materials is the time investment required to electrochemically characterise a structure,

therefore for a field of thousands of structures it is unreasonable to systematically characterise all structures without first identifying potential indicators of their electrochemical performance. To resolve this, computational methods are being employed to screen and indicate which structures are potentially viable as conductors, by using the structural data of different materials in the ICSD [17].

To accelerate the process of materials discovery, various studies have been done utilizing high throughput methods of analysis where over 1000 structures are studied for their conductive properties.

There have been a broad range of studies utilizing high-throughput screening as a part of structural analysis via a variety of different computational techniques. *Ab*-initio methods have been used as a part of structural screening by Ceder et al [18]. Where first principles calculations are used to direct a search for new potential lithium-ion cathode materials. Similarly many other studies have recently utilised first principle calculations as a method of screening [19–21].

Li^+ ion conductors are the main focus within studies, such as the study done by R. Xiao et al [3].Where they use a bond valence force-field approach, with the Morse-Type potential and Coulombic repulsion being calculated on a 3D grid, to calculate the migration barrier energies and conduction pathways within the structures. Other examples in which the bond valence approach has been used as an indicative tool in high-throughput studies include Eremin et al [4], in their study on potential potassium ion conductors, Pan et al [22] where the BV-Ewald method was used to study Lithium ion conductors, Katcho et al [23], where they combined the BV method with machine learning methods, and Shi et al [24], where they combined the BV method with geometric analysis as a new method of studying structures for their transport pathways and potential as conductors. Whilst their methods are unique and have significantly progressed the models of screening that can be used utilizing the BV method, if they have resulted in a significant step forward in the development of new materials as a result of utilizing their methods, is yet to be seen. Due to the variable nature of conductivity and the difficulty in predicting and correlating conductivity with an indicative property, the development of machine learning which

is becoming more commonplace in screening methods will hopefully lead to a more sophisticated approach in prediction.

Atomistic features have also been studied for their plausibility as indicative metrics for conductivity in structures. One such study was carried out by Sendek et al [25] where the processing of over 12,000 structures was carried out to identify potential conductors using a combination of factors such as stability, stoichiometry, raw elemental cost, susceptibility to reduction and atomistic features. Training sets were used to identify correlation between a given metric and conductivity for a list of 40 various lithium conductors.

Having the ability to study structures from a database, based on their viability as solid-state electrolytes and rank the structures on their potential as solid-state electrolytes, will prove to be highly useful. It can improve the process of materials discovery in co-ordination with experimental chemists, by providing direction to which structures are potentially viable candidates, and which are not.

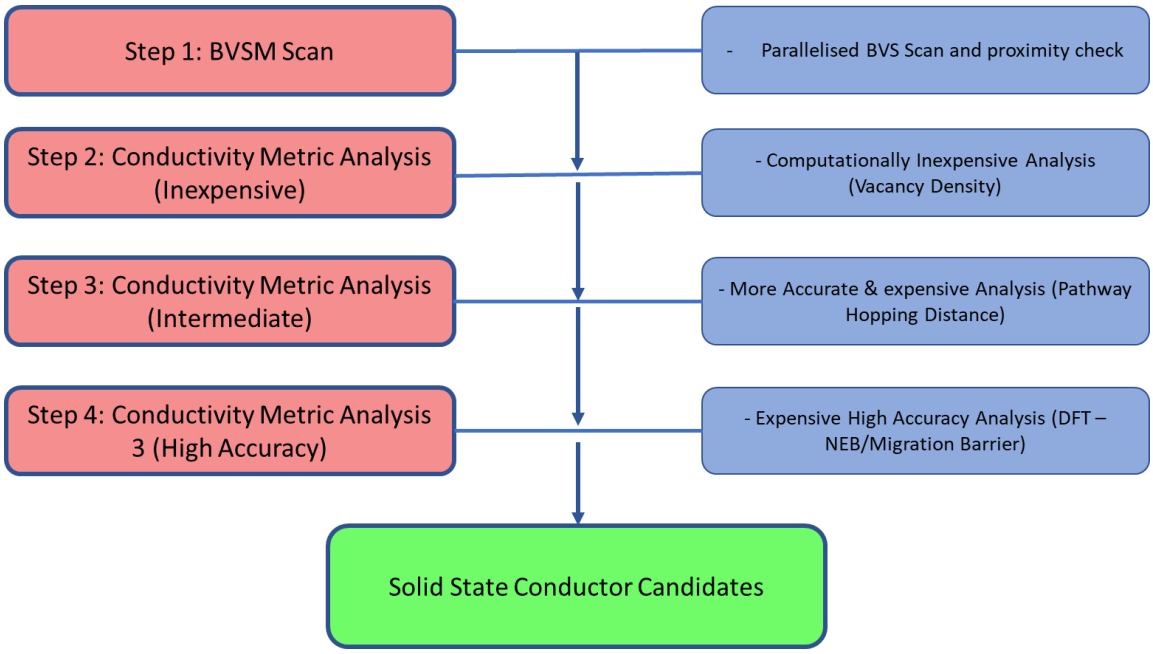

Figure 5.1. High-throughput BVS Screening Method Concept using Vacancy Density, Pathway Hopping Distance, and DFT calculations to identify potential candidates from a database.

In this study, the bond valence sum mismatch method of analysis is utilized along with various structural metrics in an attempt to identify correlation between a given property/metric and conductivity of a structure. This was done as a part of a high-throughput screening process to identify if any conductivity correlating screening steps could be introduced into the process, the concept of the screening process is displayed in **figure 5.1**. We initially explore the vacancy density of structures using the Bond Valence sum mapping method (BVSM) followed by studying the Pathway Hopping Distances (PHD) of vacancy sites within structures. This is followed by the study of using a series of metrics including Mean Partial Occupancy (MPO), Minimum Li Occupancy (MLO) and a series of metrics analysed by a Lithium Featurizer. The data collected is plotted and correlated with the conductivity of a known conductor dataset. Forty known conductors were selected based on a number of factors from the ICSD [17], the factors which determined the selection of a given conductor in the dataset included; (1) Must be a Lithium ion conductor, (2) Must be an Oxide (contain only the O^{2-} anion), (3) Must be a unique database entry, (4) Structure of which conductivity was measured must be the same as the ICSD structure, (5) Must have conductivity measured at room temperature (298 K) The methods and results are discussed and explored. The dataset tables can be seen in the S.I (Table 1-3).

5.2. Methods

Bond Valence Sum Mapping

Mapping of structures was carried out using a Bond Valence Sum Mapping script. The script was initially developed by Dr. Matthew S. Dyer [26] using the Python language. For modelling and functionality of structures, ASE (Atomic Simulation Environment) [27] was used, along with Scipy [28] and Numpy [29]. For a given structure a grid density is plotted in 3D space, for all points, the bond valence sum mismatch at a given point is calculated with an equal value contribution from center of mass calculation which leads to a more realistic isosurface plotting for mobile ion mobility. This leads to the identification of vacancy sites and regions of mobile ion mobility. The center of mass is calculated from the difference of the position relative to the center of mass. Grid points which have a low bond valence mismatch value are plotted within an isosurface, the isosurface can be modified via increasing or decreasing the mismatch cutoff value. The values used for the bond valence parameters were selected from the SoftBV set developed by Adams et al [1].

Vacancy Density

The vacancy density is calculated from generated 'maxima' points within the Bond Valence Sum Mapping. Maxima points are defined as regions of bond valence mismatch which are at their lowest values (optimal positions for mobile ions to reside) where the central cation is close to the centre of mass of the co-ordinating anions, they can also be considered as vacancy sites. Instead of values being identified as BV mismatch, vacancy (maxima) sites are measured by their BV value hence are vacancy sites when BVS for a site is close to the 'ideal valence'. Vacancy sites are defined above a float cutoff value where all sites with BV mismatch and COM contribution values above the cutoff are stored as vacancies. For all vacancies for a given cell, a density of the vacancy sites is calculated from the number of vacancies over the cell volume, the resultant data is given as $n/Å^3$ where n is the number of vacancies. To ensure valid results, a proximity check is also carried out, where vacancy sites which are at unrealistic positions, too close relative to non-mobile cations within a cutoff radius of the non-

mobile cations are removed from the system. **Figure 5.2** shows the vacancy density of a Li_4GeO_4 structure.

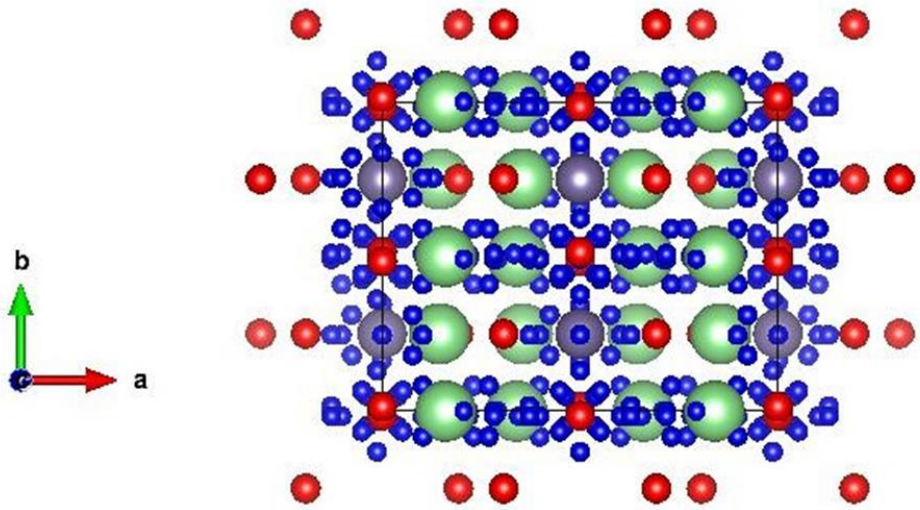

Figure 5.2. Vacancy plotted Li_4GeO_4 (ICSD_016935). Blue spheres show calculated vacancy sites plotted within cell. Green atoms are Li^{+}, purple atoms are Ge^{+4} and red atoms are O^{2-}. For this cell the vacancy density is the total number of blue spheres (vacancy sites, n) divided by the cell volume ($Å^3$).

Pathway Hopping Distance (PHD)

Pathway Hopping Distance is measured by an iterative cascading search of all vacancy sites within a cell. For the given vacancy sites, they are all uniquely identifiable within the supercell, which enables dimensionality to also be defined for a given migration pathway which are built of vacancy sites. For the determination of dimensionality and as to not exclude inter-cell hopping distances, all distances are calculated within a 2x2x2 supercell for a structure. The objective of the Pathway Hopping Distance is to determine a bottle neck hopping distance within a structure. This is done by identifying the distance in which an infinite pathway that percolates the supercell is broken once exceeded. **Figure 5.3** shows a 1x1x2 supercell, two infinite pathways are identifiable pathway 1 (1,2,5,6) and pathway 2 (4,3,8,7). The infinite pathways can be distinguished in this example as there are 4 vacancies in each cell, therefore for a vacancy site number (n), if a chain contains n+4, then an infinite connection is found, in **figure 5.3**'s example this would be 1(n)+4, with 5 being in the same chain, this distinguishes the infinite connection. The PHD will iteratively decrease the cutoff distance for the pathways until the

condition of n+4 is broken and there is no longer an infinite pathway through the cells. This point is known as the bottle neck distance and the distance between both vacancy sites in which the condition is broken is the Pathway Hopping Distance (PHD).

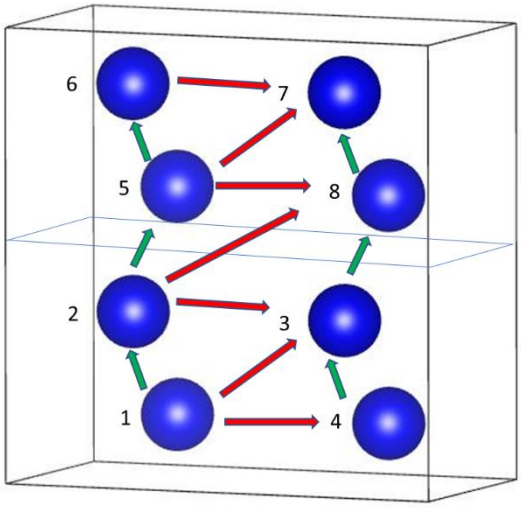

Figure 5.3. Pathway hopping for a 1x1x2 supercell of 4 vacancy sites. Green arrows show connected vacancy sites where distance between is less than the cutoff value. Red arrows show failed connections as distances exceed cutoff value. Infinite pathway identified as a chain where a vacancy site number (n) +4 at any point identifies an infinite pathway i.e. for n=1, where chain contains 1 and 5 (1(n) + 4).

Li Occupancy

Mean Partial Lithium Occupancy (MPLO) and Minimum Lithium Occupancy (MLO) are also used as potential metrics to correlate conductivity. The MPLO is determined from the total Li Occupancy over the lithium multiplicity of the structure. MLO is determined from the minimum lithium occupancy within the structure. All metrics were measured for the known Li conductor dataset.

5.3. Results

The BVSM was carried out using the SoftBV parameters developed by Adams et al [1], although the bond valence parameter 0.37 is a reliable value to use, SoftBV is an improvement on the classic parameter used by Brese and O'keeffe [6]. The bond valence parameter by Brese and O'keeffe relies on the assumption that for a central atom, the bond valence sum is entirely determined by the interactions in the atoms' first co-ordination shell. When considering the mapping of isosurfaces and potential vacancy sites, a more developed method is required, hence the use of SoftBV, where the bond valence parameter varies dependent on the shape of the mobile-ion and counter-ion species' valence pseudopotential. The SoftBV parameter considers weak interactions with atoms from a second co-ordination shell and assumes all counter-ions up to a cutoff of 4-8 Å (dependent on mobile-ion and counter-ion combination) contributes to the bond valence sum.

Vacancy Density

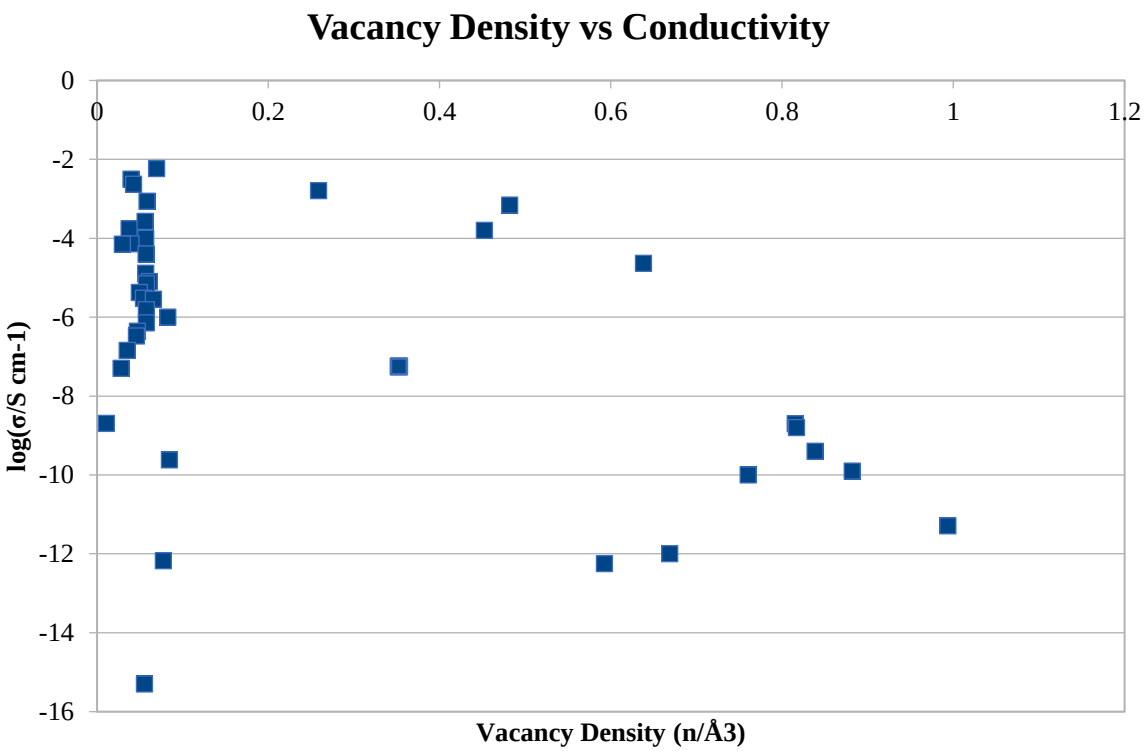

Figure 5.4. Correlation plot of the Vacancy Density (n/Å^3) against the conductivity (log(σ/S cm-1)).

For all 40 known conductors within the dataset, all of their vacancy densities were calculated and correlated against their conductivity. The value ranges of the vacancy densities were in the region of 0.994 n/Å^3 at the highest end and as low as 0.010 n/Å^3 at the lowest end. As seen in **figure 5.4**, a significant density of conductors is seen at the lower region of vacancy density ranging from the 0.010-0.080 n/Å^3. Correlation analysis was also carried out to quantify the correlation between both properties.

For the correlation analysis, true positive correlation consists of a value of 1 at its highest correlation, a true negative correlation consists of a value of -1 and absolute deviance from any correlation consists of a value of 0. For the correlation of Vacancy Density (n/Å^3) vs conductivity (log(σ/S cm^{-1}) the resultant value is -0.459 for this dataset which indicates a negative correlation between the two properties.

The rationale behind selecting vacancy density as a metric for measuring conductivity is simply that given a higher density of sites in which mobile ions can migrate through within a cell would potentially lead to an increase in conductivity. Conductivity is affected by many factors, and the likelihood of facing a bottlenecks which restricts migration decreases in theory when a higher density of vacancy sites and more potential migration pathways can be seen. The correlation analysis identifies the relationship between vacancy density and conductivity as a negative correlation with a value of -0.459 with -1 being an absolute correlation. This would suggest that as the vacancy density increases, the conductivity decreases. Whilst this result is unexpected and counter-intuitive for what we would expect, it's difficult to draw a clear conclusion from the dataset. There is a significant dispersion of results, which is the reason for a low correlation value of -0.459, whereas a clear negative correlation would be expected to be in the range of -0.75 to -1. Rather than following a correlation, a potential cutoff criteria can be considered. Data displays that all conductors with conductivities of more than 1x10^{-4} σ/S cm^{-1} have vacancy density values of no more than 0.482 n/Å^3.

Pathway Hopping Distance (PHD)

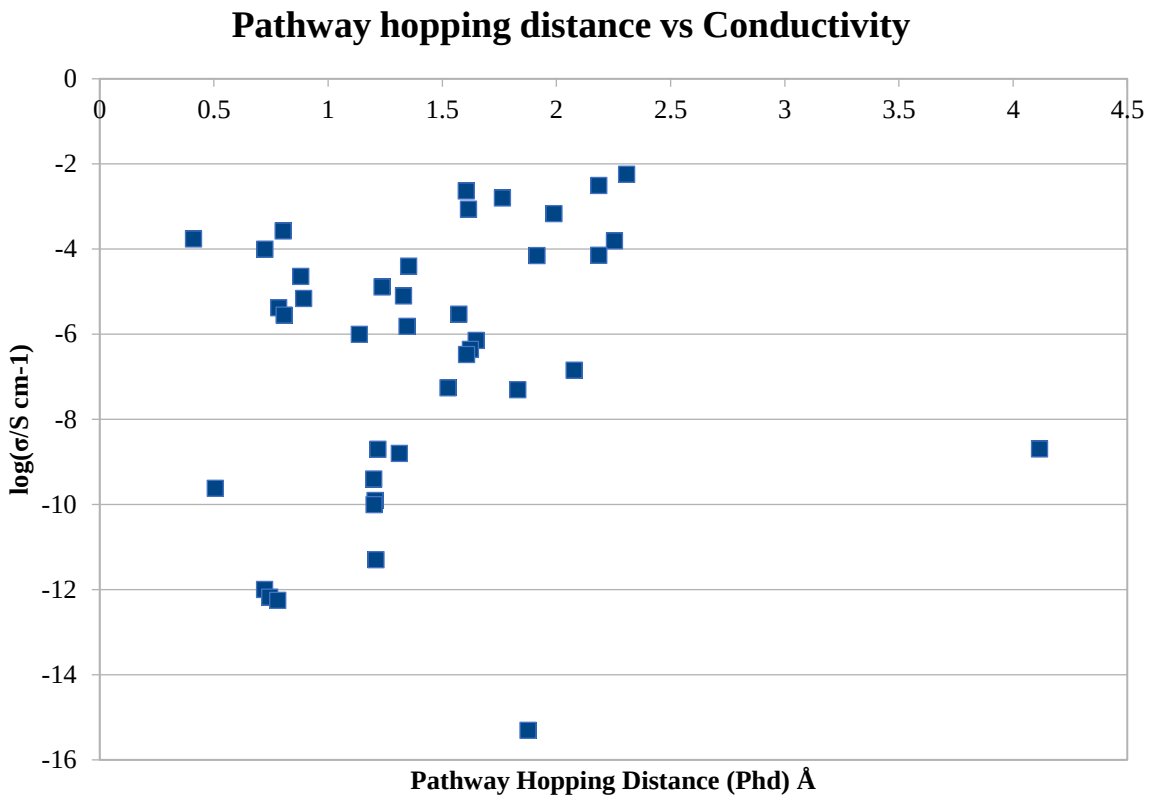

Figure 5.5. Correlation plot of the Pathway Hopping Distance (Å) against the conductivity (log(σ/S cm-1)).

For each structure, the calculation of the Pathway Hopping Distances (PHD) was carried out by iteratively cascading the pathway cut-off values to identify the breakpoint of structural percolation where an infinite connection is no longer maintained by linking the maxima (vacancy) sites within the structure. The sites used for the PHD calculation throughout are the maxima sites exclusively. The range of PHDs which can be seen in **figure 5.5** are from 4.115 Å to 0.410 Å. Although the $LiSn_2(PO_4)_3$ structure which has a value of 4.115 Å appears to be an anomaly in the dataset due to the large density of structures being in the range of 0.410 Å to 2.306 Å, with a gap of 1.809 Å between the highest PHD valued structure and its adjacent structure in relation to PHD.

For the correlation analysis of PHD vs conductivity ($\log(\sigma/S\ cm^{-1})$), a correlation value of 0.171 is given. This value indicates a weak, positive correlation between both properties.

Pathway Hopping Distance was used as a metric as the objective was to find the smallest bottleneck distance for a structure in which an infinitely connected pathway within a structure breaks once exceeded. The premise is that with a shorter PHD, less energy is required for an atom to migrate between the two vacancy sites. Potentially with smaller hopping distances we would find that conductivity increases. The correlation analysis identifies a positive correlation of 0.171, which is considered a very weak correlation with 0 being considered as no correlation whatsoever. No conclusions can be drawn between the correlation of PHD against conductivity for this dataset, although similarly to vacancy density, a cutoff could be considered. All conductors with a conductivity higher than $1x10^{-4}$ S cm^{-1} have PHD of 2.5 Å or less, which is expected, although this cutoff region is not particularly useful when considering conductivity, as almost all conductors are within this region. When looking at **figure 5.5**, there is a region where all the highest conductors reside, which is in the PHD range of 1.6-2.3 Å.

Mean Partial Lithium Occupancy (MPLO)

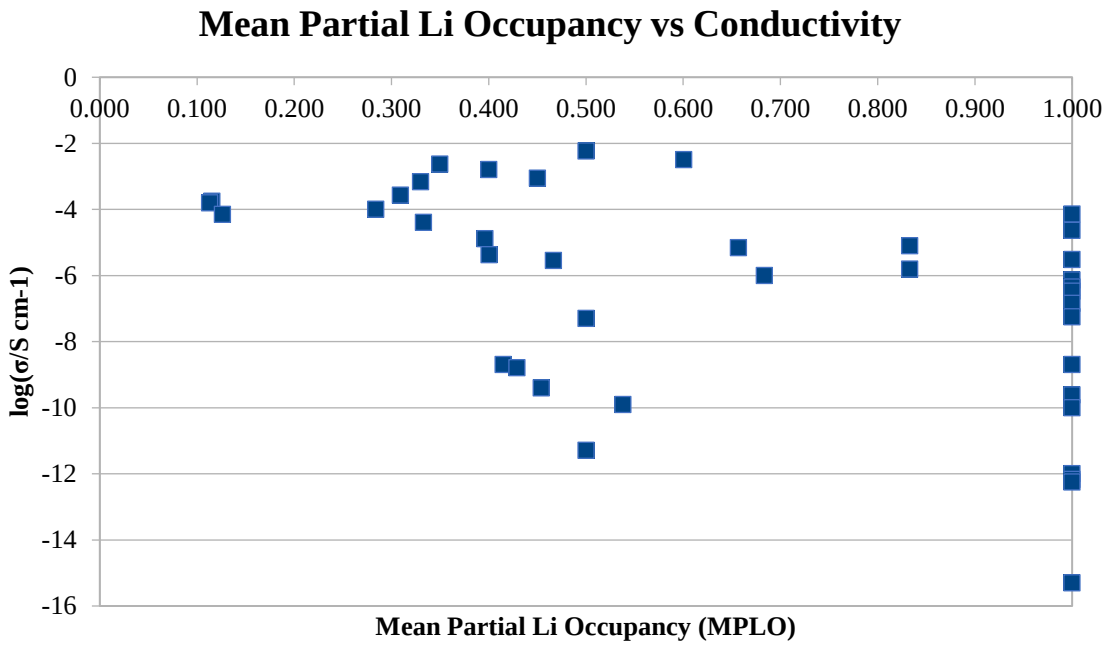

Figure 5.6. Correlation plot of the Mean Partial Li Occupancy (MPLO) against the conductivity (log(σ/S cm-1)).

The Mean Partial Lithium Occupancy (MPLO) of each structure was determined and correlated. **Figure 5.6** displays the MPLO plotted against the conductivity. The range of occupancy consists of

0.115 at the lowest end to 1.000 at the top end. There are two density regions within the correlation plot, one region is at the 1.000 value boundary where a significant number of structures can be seen. The other region is loosely scattered across the entire MPLO range but with a higher conductivity.

For the correlation analysis of MPLO vs conductivity (log(S cm^{-1})), a correlation value of -0.502 is given. This value indicates a negative correlation between both properties. We can also see that from this dataset, the maximum conductivity for a structure without partial occupancy is less than 10^{-4} S cm^{-1}, this identifies that partial occupancy is a requirement for achieving a high ionic conductivity.

The mean partial lithium occupancy (MPLO) was used as a metric to identify which structures had the most lithium site partial occupancies. The rationale behind using MPLO as a metric is that with more partial occupancies within a structure, Li mobile ions have more sites in which to migrate through, increasing the viability of increased conductivity. Correlation analysis for MPLO identified a correlation value of -0.502 which is a negative correlation. This indicates with increasing MPLO, the conductivity decreases. With the value of -0.502, a true correlation cannot be identified with this dataset, although it has a stronger relationship to conductivity than the other metrics, this is still unreliable as an indicator to introduce as a screening process step. When considering the datapoints in figure 5, the conductors with the highest conductivity all consist of MPLO values within the 0.3-0.6 range. The result is somewhat unexpected, as similar to the other metrics, the results are somewhat counter-intuitive relative to the rationale of selecting the metrics.

Minimum Lithium Occupancy (MLO)

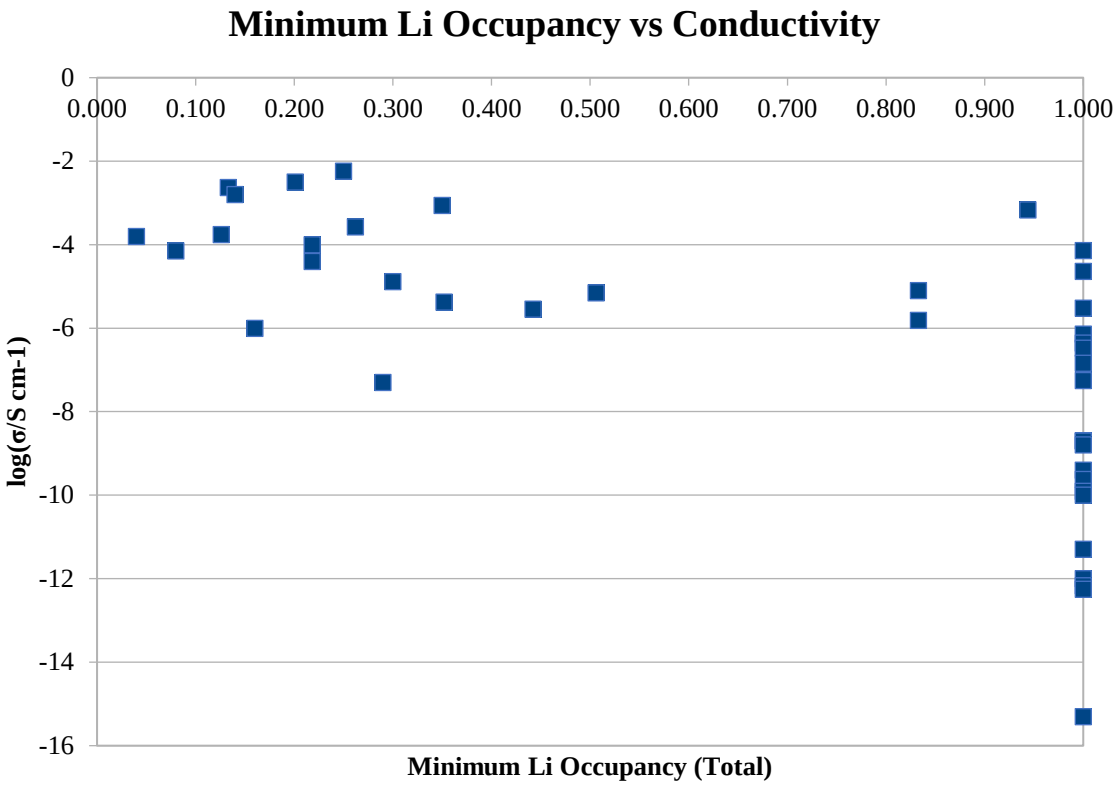

Figure 5.7. Correlation plot of the Minimum Li Occupancy (MPLO) against the conductivity (log(σ/S cm-1)).

The Minimum Lithium Occupancy (MLO) of each structure was determined and correlated. **Figure 5.7** displays the MLO plotted against the conductivity. The range of occupancy consists of 0.040 at the lowest end to 1.000 at the top end. Similarly, to MPLO, with MLO there are two density regions within the correlation plot, one region is at the 1.000 value boundary where a significant number of structures can be seen. The other region is loosely scattered across the 0.040-0.506 MLO range also similarly to MPLO, with a higher conductivity.

For the correlation analysis of MLO vs conductivity, a correlation value of -0.370 is given. This value indicates a negative correlation between both properties.

Minimum Lithium Occupancy (MLO) was included as an additional metric as the rationale, similar to that of MPLO is that with a low total lithium occupancy within the structure, there would be more sites for Li mobile ions to migrate through, potentially increasing the conductivity. The correlation

analysis for this metric was identified as -0.370, which is a negative correlation. Similar to the others, the low value of -0.307 indicates that there is no strong correlation between MLO and conductivity within the dataset. It is worth noting that the highest conductors with conductivities of $1x10^{-4}$ S cm^{-1} or higher, all consist of MLO values of 0.00 to 0.35 apart from one exception, this leads to potential MLO range cutoffs of up to 0.35 MLO when considering high-throughput screening of structures.

For the metrics selected as potential steps within high-throughput screening for conductors from databases, none of the metrics have displayed a strong correlation with conductivity. Although with larger datasets with more known conductors and more mobile-ion – counter-ion combinations, a clearer image of the validity of these metrics can be better determined either by correlation, or with metric value range classification (i.e. conductors of $1x10^{-4}$ S cm^{-1} are all located within specific ranges of a given metric).

5.4. Conclusion

In this study, we have reported the bond valence sum mapping metrics of vacancy density and pathway hopping distances along with the mean partial lithium occupancy and minimum lithium occupancy and their relation to conductivity. Development of new analytical methods was carried out using BVSM which was initially developed my M. S. Dyer, which includes contribution from centre of mass calculations. The vacancy density was developed from maxima sites within structures which represent sites which are close to the ideal valence and centre of mass contribution, and the PHD analysis was developed from the resultant maxima (vacancy) sites which are generated from the BVSM script. The methods were developed to identify if they would correlate with conductivity of conductors, therefore would be integral screening steps within a high-throughput calculation process for identifying new conductors from a database of structures. From the analysis carried out and correlation between the metrics and the Li conductor dataset used of 40 known conductors, there was no evident correlation in the metrics. The strongest correlation determined was -0.502 from the MPLO, which is a negative correlation. Although this value, is considered low, we cannot conclude that a correlation exists between MPLO and conductivity. Vacancy density, PHD and MLO all displayed weak to no correlations and cannot be considered as indicators of potential conductors. Further analysis of the metrics with larger datasets and with different mobile ions could be carried out to better understand the metrics relationship with conductivity. PHD shows the potential for further studies, to potentially look at combining maxima (vacancy) sites which have been calculated along with the original structural lithium sites, and what impact introducing partial occupancy and disorder to the structural lithium sites could have on the PHD values and its correlation with conductivity.

5.5. References

1 S. Adams, *Acta Crystallogr. Sect. B Struct. Sci.*, 2001, **57**, 278–287.

2 M. Avdeev, M. Sale, S. Adams and R. P. Rao, *Solid State Ionics*, 2012, **225**, 43–46.

3 R. Xiao, H. Li and L. Chen, *J. Mater.*, 2015, **1**, 325–332.

4 R. A. Eremin, N. A. Kabanova, Y. A. Morkhova, A. A. Golov and V. A. Blatov, *Solid State Ionics*, 2018, **326**, 188–199.

5 I. D. Brown, *The Chemical Bond in Inorganic Chemistry*, Oxford University Press, 2006, vol. 9780199298.

6 N. E. Brese and M. O'Keeffe, *Acta Crystallogr. Sect. B Struct. Sci.*, 1991, **47**, 192–197.

7 R. Prasada Rao, H. Chen and S. Adams, *Chem. Mater.*, 2019, **31**, 8649–8662.

8 L. L. Wong, K. C. Phuah, R. Dai, H. Chen, W. S. Chew and S. Adams, *Chem. Mater.*, 2021, **33**, 625–641.

9 S. Adams, *Solid State Ionics*, 1998, **105**, 67–74.

10 S. Adams and J. Swenson, *Phys. Rev. Lett.*, 2000, **84**, 4144–4147.

11 S. Adams, *Solid State Ionics*, 2006, **177**, 1625–1630.

12 S. Adams and R. P. Rao, *Phys. Chem. Chem. Phys.*, 2009, **11**, 3210.

13 S. Adams and R. P. Rao, in *Structure and Bonding*, 2014, vol. 158, pp. 129–159.

14 H. Chen and S. Adams, *IUCrJ*, 2017, **4**, 614–625.

15 Y. Nishitani, S. Adams, K. Ichikawa and T. Tsujita, *Solid State Ionics*, 2018, **315**, 111–115.

16 H. Chen, L. L. Wong, S. Adams and IUCr, *urn:issn:2052-5206*, 2019, **75**, 18–33.

17 A. Belkly, M. Helderman, V. L. Karen and P. Ulkch, *Acta Crystallogr. Sect. B Struct. Sci.*, 2002, **58**, 364–369.

18 G. Ceder, Y.-M. Chiang, D. R. Sadoway, M. K. Aydinol, Y.-I. Jang and B. Huang, *Nature*, 1998, **392**, 694–696.

19 Y. Li and D. J. Singh, *J. Mater. Chem. C*, 2019, **7**, 2436–2442.

20 R. Xiao, H. Li and L. Chen, *J. Mater. Chem. A*, 2020, **8**, 5157–5162.

21 L. Kahle, A. Marcolongo and N. Marzari, *Energy Environ. Sci.*, 2020, **13**, 928–948.

22 D. Chen, J. Jie, M. Weng, S. Li, D. Chen, F. Pan and L. W. Wang, *J. Mater. Chem. A*, 2019, **7**, 1300–1306.

23 N. A. Katcho, J. Carrete, M. Reynaud, G. Rousse, M. Casas-Cabanas, N. Mingo, J. Rodríguez-Carvajal and J. Carrasco, *J. Appl. Crystallogr.*, 2019, **52**, 148–157.

24 B. He, P. Mi, A. Ye, S. Chi, Y. Jiao, L. Zhang, B. Pu, Z. Zou, W. Zhang, M. Avdeev, S. Adams, J. Zhao and S. Shi, *Acta Mater.*, 2021, **203**, 116490.

25 A. D. Sendek, Q. Yang, E. D. Cubuk, K.-A. N. Duerloo, Y. Cui and E. J. Reed, *Energy Environ. Sci.*, 2017, **10**, 306–320.

26 M. S. Dyer, *Bond Val. Sum Mapp. Scr.*

27 A. Hjorth Larsen, J. Jørgen Mortensen, J. Blomqvist, I. E. Castelli, R. Christensen, M. Dułak, J. Friis, M. N. Groves, B. Hammer, C. Hargus, E. D. Hermes, P. C. Jennings, P. Bjerre Jensen, J. Kermode, J. R. Kitchin, E. Leonhard Kolsbjerg, J. Kubal, K. Kaasbjerg, S. Lysgaard, J. Bergmann Maronsson, T. Maxson, T. Olsen, L. Pastewka, A. Peterson, C. Rostgaard, J. Schiøtz, O. Schütt, M. Strange, K. S. Thygesen, T. Vegge, L. Vilhelmsen, M. Walter, Z. Zeng and K. W. Jacobsen, *J. Phys. Condens. Matter*, 2017, 29, 273002.

28 P. P. Eric Jones, Travis Oliphant, *SciPy Tools*.

29 C. R. Harris, K. J. Millman, S. J. van der Walt, R. Gommers, P. Virtanen, D. Cournapeau, E. Wieser, J. Taylor, S. Berg, N. J. Smith, R. Kern, M. Picus, S. Hoyer, M. H. van Kerkwijk, M.

Brett, A. Haldane, J. F. del Río, M. Wiebe, P. Peterson, P. Gérard-Marchant, K. Sheppard, T. Reddy, W. Weckesser, H. Abbasi, C. Gohlke and T. E. Oliphant, *Nature*, 2020, **585**, 357–362.

5.6. Supporting Information

S.I Table 1 – Vacancy Density

Vacancy Density (n/Å3)	Conductivity (σ/S cm-1)	log(σ/S cm-1)	ICSD Code	Compound
0.069416088	5.80E-03	-2.236572006	-	Li3La3W2O12 (400k)
0.039487433	3.16E-03	-2.500312917	427619	Li1.2(Al0.2Ti1.8)(PO4)3
0.042745813	2.35E-03	-2.628932138	163298	Li1.4(Al0.4Ge0.2Ti1.4)(PO4)3
0.25857467	1.60E-03	-2.795880017	267438	LiTa2PO8
0.058331274	8.70E-04	-3.060480747	183873	Li6.75La3(Zr1.75Ta0.25)O12
0.481697603	6.88E-04	-3.162411562	82671	La0.557Li0.33TiO3
0.056007552	2.70E-04	-3.568636236	237146	Li6.5La3Nb1.25 0.75O12
0.037313414	1.75E-04	-3.756961951	55751	Li1.5Fe0.5Ti1.5(PO4)3
0.452221224	1.58E-04	-3.801342913	97658	LiZr2(PO4)3 (Rhombo)
0.056900054	1.00E-04	-4	237141	Li6La3Nb1.5Y0.5O12
0.039542257	7.20E-05	-4.142667504	95979	LiTi2(PO4)3
0.029390335	7.10E-05	-4.148741651	191891	Li1.15(Y0.15Zr1.85)(PO4)3
0.05717104	4.00E-05	-4.397940009	158372	Li5La3Bi2O12
0.638143791	0.000023	-4.638272164	238687	Li7La3Zr2O12 (tetragonal)
0.056760716	1.30E-05	-4.886056648	163861	Li6BaLa2Ta2O12
0.060821857	8.00E-06	-5.096910013	54864	Li5La3Nb2O12
0.057700166	7.00E-06	-5.15490196	237200	Li6SrLa2Ta2O12
0.049235025	4.20E-06	-5.37675071	157628	Li6SrLa2Nb2O12
0.054027816	3.00E-06	-5.522878745	50420	Li3Sc2(PO4)3
0.065683786	2.85E-06	-5.54515514	183607	Li7La3Zr2O12 (cubic)
0.057689184	1.54E-06	-5.812479279	54866	Li5La3Ta2O12
0.082701159	1.00E-06	-6	100169	Li14Zn(GeO4)4
0.057526693	7.20E-07	-6.142667504	69763	LiGe2(PO4)3
0.046925427	4.41E-07	-6.355561411	151920	Li2TiCr(PO4)3
0.045977217	3.34E-07	-6.476253533	151919	Li2TiFe(PO4)3
0.035018844	1.44E-07	-6.841637508	51333	Li2FeZr(PO4)3
0.352476647	5.60E-08	-7.251811973	62244	Li3Fe2(PO4)3
0.02809655	5.00E-08	-7.301029996	89456	LiZr2(PO4)3 (Triclinic)
0.010809485	2.02E-09	-8.694648631	83831	LiSn2(PO4)3
0.815273395	2.000E-09	-8.698970004	-	Li0.83Mg0.83In0.17PO4
0.816786856	1.600E-09	-8.795880017	-	Li0.85Mg0.85In0.15PO4
0.838538975	4.000E-10	-9.397940009	-	Li0.9Mg0.9In0.1PO4
0.084347802	2.40E-10	-9.619788758	8222	Li4SiO4
0.881853125	1.250E-10	-9.903089987	-	Li0.95Mg0.95In0.05PO4
0.760257533	1.00E-10	-10	38209	LiFePO4
0.993576093	5.100E-12	-11.29242982	-	LiMgPO4
0.668544505	1.01E-12	-11.99614184	10257	Li3PO4
0.077374216	6.75E-13	-12.17052618	16935	Li4GeO4
0.592636342	5.640E-13	-12.24873668	19002	Li3VO4
0.05544995	5.00E-16	-15.30103	5427	Li2(Ge7O15)

S.I Table 2 – Pathway Hopping Distance

Pathway Hopping Distance (Å^3)	Conductivity (σ/S cm-1)	log(σ/S cm-1)	ICSD Code	Compound
2.306042822	5.80E-03	-2.24E+00	-	Li3La3W2O12 (1)
2.184194289	3.16E-03	-2.50E+00	427619	Li1.2(Al0.2Ti1.8)(PO4)3
1.605105021	2.35E-03	-2.63E+00	163298	Li1.4(Al0.4Ge0.2Ti1.4)(PO4)3
1.763500468	1.60E-03	-2.80E+00	267438	LiTa2PO8
1.613978431	8.70E-04	-3.06E+00	183873	Li6.75La3(Zr1.75Ta0.25)O12
1.989197613	6.88E-04	-3.16E+00	82671	La0.557Li0.33TiO3
0.803034435	2.70E-04	-3.57E+00	237146	Li6.5La3Nb1.25 0.75O12
0.410181119	1.75E-04	-3.76E+00	55751	Li1.5Fe0.5Ti1.5(PO4)3
2.254101199	1.58E-04	-3.80E+00	97658	LiZr2(PO4)3 (Rhombo)
0.723061997	1.00E-04	-4.00E+00	237141	Li6La3Nb1.5Y0.5O12
2.185023953	7.20E-05	-4.14E+00	95979	LiTi2(PO4)3
1.914275873	7.10E-05	-4.15E+00	191891	Li1.15(Y0.15Zr1.85)(PO4)3
1.351965243	4.00E-05	-4.40E+00	158372	Li5Bi2La3O12
0.879846726	2.30E-05	-4.64E+00	238687	Li7La3Zr2O12 (tetragonal)
1.235554001	1.30E-05	-4.89E+00	163861	Li6La2Ta2Ba1O12
1.329688246	8.00E-06	-5.10E+00	54864	Li5La3Nb2O12
0.892286802	7.00E-06	-5.15E+00	237200	Li6SrLa2Ta2O12
0.783256907	4.20E-06	-5.38E+00	157628	Li6SrLa2Nb2O12
1.572415576	3.00E-06	-5.52E+00	50420	Li3Sc2(PO4)3
0.806392465	2.85E-06	-5.55E+00	183607	Li7La3Zr2O12
1.345189804	1.54E-06	-5.81E+00	54866	Li5La3Ta2O12
1.136616733	1.00E-06	-6.00E+00	100169	Li14Zn(GeO4)4
1.648565727	7.20E-07	-6.14E+00	69763	LiGe2(PO4)3
1.622792989	4.41E-07	-6.36E+00	151920	Li2TiCr(PO4)3
1.605844142	3.34E-07	-6.48E+00	151919	Li2TiFe(PO4)3
2.076489938	1.44E-07	-6.84E+00	51333	Li2FeZr(PO4)3
1.524987754	5.60E-08	-7.25E+00	62244	Li3Fe2(PO4)3
1.829705659	5.00E-08	-7.30E+00	89456	LiZr2(PO4)3
4.115465381	2.02E-09	-8.69E+00	83831	LiSn2(PO4)3
1.217783243	2.000E-09	-8.70E+00	-	Li0.83Mg0.83In0.17PO4
1.311431295	1.600E-09	-8.80E+00	-	Li0.85Mg0.85In0.15PO4
1.199649028	4.000E-10	-9.40E+00	-	Li0.9Mg0.9In0.1PO4
0.50520415	2.40E-10	-9.62E+00	8222	Li4O4Si
1.20532128	1.250E-10	-9.90E+00	-	Li0.95Mg0.95In0.05PO4
1.200838117	1.00E-10	-1.00E+01	38209	LiFePO4
1.209418088	5.100E-12	-1.13E+01	-	LiMgPO4
0.720800981	1.01E-12	-1.20E+01	10257	Li3PO4
0.743716655	6.75E-13	-1.22E+01	16935	Li4GeO4
0.778723334	5.640E-13	-1.22E+01	19002	Li3VO4
1.87518144	5.00E-16	-1.53E+01	5427	Li2(Ge7O15)

S.I Table 3 – Mean Partial Lithium Occupancy (MPLO)

Mean Partial Occupancy	Conductivity (σ/S cm-1)	log(σ/S cm-1)	ICSD Code	Compound
0.500	5.80E-03	-2.236572006	-	Li3La3W2O12 (400k)
0.601	3.16E-03	-2.500312917	427619	Li1.2(Al0.2Ti1.8)(PO4)3
0.350	2.35E-03	-2.628932138	163298	Li1.4(Al0.4Ge0.2Ti1.4)(PO4)3
0.400	1.60E-03	-2.795880017	267438	LiTa2PO8
0.450	8.70E-04	-3.060480747	183873	Li6.75La3(Zr1.75Ta0.25)O12
0.330	6.88E-04	-3.162411562	82671	La0.557Li0.33TiO3
0.309	2.70E-04	-3.568636236	237146	Li6.5La3Nb1.25 0.75O12
0.115	1.75E-04	-3.756961951	55751	Li1.5Fe0.5Ti1.5(PO4)3
0.113	1.58E-04	-3.801342913	97658	LiZr2(PO4)3 (Rhombo)
0.284	1.00E-04	-4	237141	Li6La3Nb1.5Y0.5O12
1.000	7.20E-05	-4.142667504	95979	LiTi2(PO4)3
0.126	7.10E-05	-4.148741651	191891	Li1.15(Y0.15Zr1.85)(PO4)3
0.333	4.00E-05	-4.397940009	158372	Li5La3Bi2O12
1.000	2.30E-05	-4.638272164	238687	Li7La3Zr2O12 (tetragonal)
0.396	1.30E-05	-4.886056648	163861	Li6BaLa2Ta2O12
0.833	8.00E-06	-5.096910013	54864	Li5La3Nb2O12
0.657	7.00E-06	-5.15490196	237200	Li6SrLa2Ta2O12
0.400	4.20E-06	-5.37675071	157628	Li6SrLa2Nb2O12
1.000	3.00E-06	-5.522878745	50420	Li3Sc2(PO4)3
0.466	2.85E-06	-5.54515514	183607	Li7La3Zr2O12
0.833	1.54E-06	-5.812479279	54866	Li5La3Ta2O12
0.683	1.00E-06	-6	100169	Li14Zn(GeO4)4
1.000	7.20E-07	-6.142667504	69763	LiGe2(PO4)3
1.000	4.41E-07	-6.355561411	151920	Li2TiCr(PO4)3
1.000	3.34E-07	-6.476253533	151919	Li2TiFe(PO4)3
1.000	1.44E-07	-6.841637508	51333	Li2FeZr(PO4)3
1.000	5.60E-08	-7.251811973	62244	Li3Fe2(PO4)3
0.500	5.00E-08	-7.301029996	89456	LiZr2(PO4)3
1.000	2.02E-09	-8.694648631	83831	LiSn2(PO4)3
0.415	2.00E-09	-8.698970004	-	Li0.83Mg0.83In0.17PO4
0.429	1.60E-09	-8.795880017	-	Li0.85Mg0.85In0.15PO4
0.454	4.00E-10	-9.397940009	-	Li0.9Mg0.9In0.1PO4
1.000	2.40E-10	-9.619788758	8222	Li4SiO4
0.538	1.250E-10	-9.903089987	-	Li0.95Mg0.95In0.05PO4
1.000	1.00E-10	-10	38209	LiFePO4
0.500	5.100E-12	-11.29242982	-	LiMgPO4
1.000	1.01E-12	-11.99614184	10257	Li3PO4
1.000	6.75E-13	-12.17052618	16935	Li4GeO4
1.000	5.64E-13	-12.24873668	19002	Li3VO4
1.000	5.00E-16	-15.30103	5427	Li2(Ge7O15)

S.I Table 4 – Minimum Lithium Occupancy (MLO)

Minimum Li Occupancy (Total)	Conductivity (σ/S cm-1)	log(σ/S cm-1)	ICSD Code	Compound
0.250	5.80E-03	-2.236572006	-	Li3La3W2O12 (400k)
0.201	3.16E-03	-2.500312917	427619	Li1.2(Al0.2Ti1.8)(PO4)3
0.133	2.35E-03	-2.628932138	163298	Li1.4(Al0.4Ge0.2Ti1.4)(PO4)3
0.140	1.60E-03	-2.795880017	267438	LiTa2PO8
0.350	8.70E-04	-3.060480747	183873	Li6.75La3(Zr1.75Ta0.25)O12
0.944	6.88E-04	-3.162411562	82671	La0.557Li0.33TiO3
0.262	2.70E-04	-3.568636236	237146	Li6.5La3Nb1.25 0.75O12
0.126	1.75E-04	-3.756961951	55751	Li1.5Fe0.5Ti1.5(PO4)3
0.040	1.58E-04	-3.801342913	97658	LiZr2(PO4)3 (Rhombo)
0.218	1.00E-04	-4	237141	Li6La3Nb1.5Y0.5O12
1.000	7.20E-05	-4.142667504	95979	LiTi2(PO4)3
0.080	7.10E-05	-4.148741651	191891	Li1.15(Y0.15Zr1.85)(PO4)3
0.218	4.00E-05	-4.397940009	158372	Li5La3Bi2O12
1.000	2.30E-05	-4.638272164	238687	Li7La3Zr2O12 (tetragonal)
0.300	1.30E-05	-4.886056648	163861	Li6BaLa2Ta2O12
0.833	8.00E-06	-5.096910013	54864	Li5La3Nb2O12
0.506	7.00E-06	-5.15490196	237200	Li6SrLa2Ta2O12
0.352	4.20E-06	-5.37675071	157628	Li6SrLa2Nb2O12
1.000	3.00E-06	-5.522878745	50420	Li3Sc2(PO4)3
0.442	2.85E-06	-5.54515514	183607	Li7La3Zr2O12
0.833	1.54E-06	-5.812479279	54866	Li5La3Ta2O12
0.160	1.00E-06	-6	100169	Li14Zn(GeO4)4
1.000	7.20E-07	-6.142667504	69763	LiGe2(PO4)3
1.000	4.41E-07	-6.355561411	151920	Li2TiCr(PO4)3
1.000	3.34E-07	-6.476253533	151919	Li2TiFe(PO4)3
1.000	1.44E-07	-6.841637508	51333	Li2FeZr(PO4)3
1.000	5.60E-08	-7.251811973	62244	Li3Fe2(PO4)3
0.290	5.00E-08	-7.301029996	89456	LiZr2(PO4)3
1.000	2.02E-09	-8.694648631	83831	LiSn2(PO4)3
1.000	2.000E-09	-8.698970004	-	Li0.83Mg0.83In0.17PO4
1.000	1.600E-09	-8.795880017	-	Li0.85Mg0.85In0.15PO4
1.000	4.000E-10	-9.397940009	-	Li0.9Mg0.9In0.1PO4
1.000	2.40E-10	-9.619788758	8222	Li4SiO4
1.000	1.250E-10	-9.903089987	-	Li0.95Mg0.95In0.05PO4
1.000	1.00E-10	-10	38209	LiFePO4
1.000	5.100E-12	-11.29242982	-	LiMgPO4
1.000	1.01E-12	-11.99614184	10257	Li3PO4
1.000	6.75E-13	-12.17052618	16935	Li4GeO4
1.000	5.640E-13	-12.24873668	19002	Li3VO4
1.000	5.00E-16	-15.30103	5427	Li2(Ge7O15)

Chapter 6: Investigation of Magnesium Anti-bixbyites as Multi-valent Solid Conductors

Contribution

All computational work that was carried out in this section was performed by R. E. Morris with support from M. S. Dyer.

6.1. Introduction

In the search for new solid-state electrolyte materials, multivalent cations have also been considered such as magnesium and calcium. Studies on solid state electrolytes have recently focused on magnesium spinels primarily [1–3] . In an attempt to reduce the demand on lithium by the primary lithium-ion driven conductor material field, magnesium is considered a potential candidate due to its abundance and its potential to increase the energy density [4]. The increase in energy density of magnesium relative to lithium is due to it carrying twice the charge per ion. Magnesium cathodes are currently used in magnesium batteries (3,830 $Ah1^{-1}$) and have a larger energy density than graphite lithium anodes (700 $Ah1^{-1}$) and metal lithium anodes (2,000 $Ah1^{-1}$) [5,6]. Applying the increased charge density of magnesium for use as an electrolyte could prove to be valuable in creating smaller more efficient batteries.

The problem currently faced by multi-valent conductors including magnesium is the lack of mobility at room temperature [7]. Studies have been carried out to try and progress the conductivity of multi-valent conductors, but high conductivity can only be seen at higher temperatures. Some examples of this include, Ikeda et al.[8] who found $MgZr_4(PO_4)_6$ has a conductivity of $2.9x10^{-5}$ Scm^{-1} at 400^{o}C and

$6.1x10^{-3}$ Scm^{-1} at 800°C, Imanaka et al.[9] achieved a Mg^{2+} conductivity of up to 10^{-2} Scm^{-1} at 800°C with an Mg composite $Zr_2O(PO_4)_2$ phase and Higahi et al.[10] demonstrated a Mg^{2+} ionic conductivity of 10^{-6} S cm^{-1} at 150°C for $Mg(BH_4)(NH_2)$. Ceder et al. [2] achieved a Mg^{2+} mobility of $1x10^{-5}$-$1x10^{-4}$ S cm^{-1} at room temperature for a magnesium chalcogenide spinel, which is currently the highest reported Mg^{2+} mobility at room temperature for a solid-state material. A summary of the conductivities can be seen in **table 6.1,** highlighting the potential within Mg conductors to explore and improve upon current materials.

Table 6.1 Summary of conductivities in introduction.

Structure	Conductivity (S cm^{-1})	Temperature (°C)	Reference
$MgZr_4(PO_4)_6$	$2.9x10^{-5}$	400	8
	$6.1x10^{-3}$	800	8
Mg composite $Zr_2O(PO_4)_2$	$1x10^{-2}$	800	9
$Mg(BH_4)(NH_2)$	$1x10^{-6}$	150	10
$MgSc_2Se_4$	$1x10^{-4}$ - $1x10^{-5}$	25	2

No other research has currently been carried out that identifies high conductivity at room temperature for multi-valent conductors, this represents a significant hurdle for the use of magnesium as a conductor. The low room temperature mobility of Mg^{2+} ions must be overcome for it to be considered a viable candidate as a conductor. This introduces many problems for example low mobility leads to the inability of using solid coatings which act as barriers to protect electrodes from reaction with the liquid electrolyte phase, therefore battery technologies using magnesium still suffer from thermal runaway which is one of the significant problems faced by current batteries.

Currently there are not many Mg^{2+} containing conductors. Research has been carried out to develop the intercalation of Mg^{2+} into materials with the aim of producing a viable cathode material, such examples include Aurbach et al [11,4] who initially researched into the intercalation of Mg^{2+} into the Mo_6S_8 Chevrel phase with a potential of 1.0-1.3V and a 135 mA h g^{-1} maximum charge capacity.

Other materials have also been studied to identify the intercalation potential with Mg^{2+}. V_2O_5 intercalation with Mg^{2+} was carried out by Zhu et al, where Mg^{2+} was inserted into the inner layer spacing [12]. $CoSiO_4$ [13] , MoO_3 [14], NbS_3 [15], TiS_2 (cubic and layered) [16], are also examples of materials in which Mg^{2+} intercalation has been possible.

Ceder et al carried-out a computational study of Mg intercalation into a fixed spinel-based host structure [1], **figure 6.1** shows an example of a magnesium spinel structure. Using ab initio methods, they identified that the intercalation of Mg into Mn_2O_4 was found to be a good candidate utilizing Mg^{2+} as mobile ions. Yin et al .[17] intercalated experimentally Mg into $MgMn_2O_4$ from an organic electrolyte. Further advancements with Mg conductors were made, ternary spinel magnesium chalcogenides MgX_2Z_4 (X = In, Y, Sc) and (Z = S, Se) ($Fd\bar{3}m$) was discovered and developed by Ceder et al [2]. In their study they demonstrate via tuning of crystal structure and chemistry that higher magnesium mobility can be achieved. They used a combination of ab initio calculations, synchrotron X-ray diffraction (XRD), electrochemical impedance spectroscopy and solid-state nuclear magnetic resonance (SS-NMR) to identify new crystalline Mg conductors which have high Mg^{2+} ion mobility at room temperature.

Ceder et al.[2] selected the spinel structure to investigate and develop based on a number of factors which consist of the theory that magnesium mobility is highest in structures where the Mg^{2+} ions are in unfavourable coordination and that the structures have a high cell volume per anion. Statistical analysis of the Inorganic Crystal Structural Database (ICSD) identifies that Mg^{2+} favours octahedral coordination in sulfides and oxides [1,18,19]. It is also reported with computational studies that high mobility of an ion is achievable when the stable site coordination of the ion is considered unfavourable and the activated state coordination is considered more favourable [1,18]. This leads to a decrease in the migration energy barrier faced by a mobile ion. Along with minimizing coordination environment change along the migration pathway a low energy barrier for the mobile ion is achieved [18,20]. The optimal framework for an Mg conductor is considered to be a close-packed framework where the Mg^{2+} ion is not occupying an octahedrally coordinated site. Therefore Cedar et al. [2] considered a spinel to be

a good conductor due to Mg^{2+} occupying a tetrahedral coordinated stable site. With the aim of reducing the migration energy barrier faced by the Mg^{2+} ions to promote mobility, as mentioned previously, an additional factor was considered, where if an increase in cell volume per anion is seen, then a reduction of migration energy barrier can be found [20,21]. The energy of the migration barrier decreases from O^{2-} to S^{2-} to Se^{2-} to Te^{2-} in the given order. This knowledge let them to study sulfide and selenide spinels.

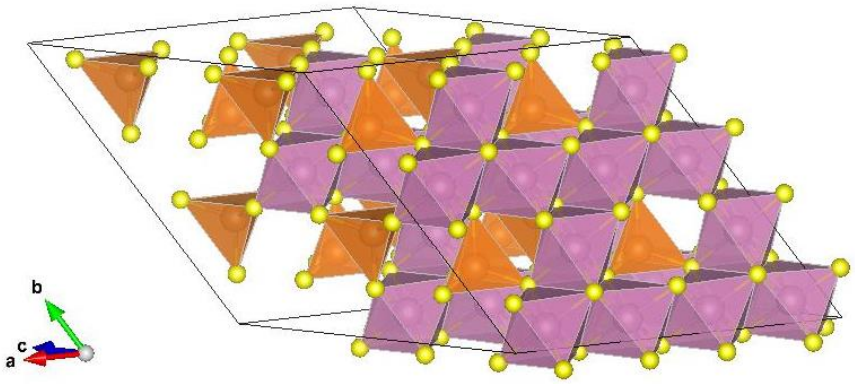

Figure 6.1. Mg Spinel, $MgIn_2S_4$ unit cell (MP-20493 [22]). Orange polyhedra consist of a tetrahedrally co-ordinated orange Mg^{2+} atom, co-ordinated with yellow S^{2-} atoms. Purple polyhedral consist of a six-fold co-ordinated purple In^{3+} atom co-ordinated with yellow S^{2-} atoms.

Another example of a crystal with a cubic closed packed structure and with the metal at a tetrahedral site is an anti-bixbyite. O'Keeffe et al [23] reported a full refinement of the Mg_3N_2 and Zn_3N_2 crystal structures using time-of-flight powder neutron diffraction and confirmed the atom arrangement with Mg and Zn in the tetrahedral sites with a cubic closed packed array. **Figure 6.2** shows an example of a magnesium anti-bixbyite containing indium. They found that the general positions in the cubic structure has metal atoms at the 48*e* positions of $Ia\bar{3}$ and two six-fold coordinated N atom sites at the N(1), 8*b* position and the N(2) 24*d* positions.

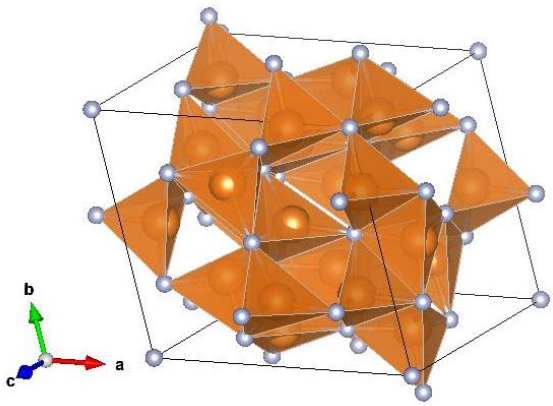

Figure 6.2. Cubic Closed Packed Array Anti-bixbyite Mg_3N_2 unit cell (MP-1559 [22]) . Orange polyhedral consist of a 4-fold co-ordinated Mg^{2+} atom, co-ordinated with grey N^{3-} atoms.

For the binary nitride Mg_3N_2 a study was also carried out identifying the metal doping capabilities into the anti-bixbyite structure by Schnick et al [24]. In this study they synthesised Eu^{2+} doped Mg_3N_2 (Mg_3N_2:Eu^{2+}) by reacting Mg with NaN_3 and EuF_3 in a sodium flux at 760°C using welded tantalum ampules. These studies demonstrated the capability of doping metals into the cubic closed packed anti-bixbyite structure which consists of Mg occupying the tetrahedral site.

In this study we explore the stability and convex hull energies of doped Mg_3N_2 anti-bixbyite using trivalent and tetravalent cations with the purpose of identifying a potential Mg^{2+} divalent solid-state electrolyte. The objective of creating a doped anti-bixbyite structure is to create disorder and vacancies within the structure to promote ionic mobility. Al, Ga and In were selected as dopants as they are all trivalent metals. Therefore, for every 2 Al, Ga, or In atom 3 Mg^{2+} ions are displaced creating vacancies within the structure. Similarly, for Zr, Sn and Si, they were selected as tetravalent metals and semi-metals. Doping of each Zr, Sn or Si atom would displace 2 Mg^{2+} atoms therefore creating a larger ratio of vacancies per dopant ion than the trivalent metals. The rationale behind the study is based on the research carried out by Ceder et al [2] in which they considered the optimal framework for a Mg^{2+} conductor to be a cubic closed packed array. Combined with the study by O'Keeffe et al [23] and Schnick et al [24], where the anti-bixbyite Mg_3N_2, is synthesised with the $Ia\bar{3}$ space group, cubic close packed array and doped with the Eu^{2+} metal. Mg_3N_2 is considered as a potentially viable solid-state

electrolyte candidate. Mg^{2+} in the anti-bixbyite structure is also tetrahedrally coordinated in its stable site, which is considered an unfavourable site relative to an octahedrally co-ordinated site. We also explore the stability and convex hull energy of silicide doped Mg_3N_2 with the objective of introducing an increased Mg^{2+} to anion ratio by moving Mg_3N_2 closer to Mg_2Si along the solid-state solution. We report the results in three sections based on the dopants used, which are the following: (1) $Mg_{2.75+}X_{0.125}N_2$ (X = Zr, Sn, Si), (2) $Mg_{2.625}X_{0.25}N_2$ (X = Al, Ga, In) and (3) silicide Mg_3N_2. In each section we report and discuss the relative stabilities, convex hull energies and the decomposition routes faced by each doped structure.

6.2. Methods

Computational Methods

Optimizations of all materials was carried out using DFT calculations utilizing the Perdew-Burke-Ernzerhof generalized gradient approximation [25]. The Vienna ab-initio Simulation Package (VASP) was used to perform the relaxations [26]. The geometry optimizations were performed using a conjugate gradient algorithm with Gaussian smearing [27]. For the k-point sampling of the Brillouin zone integrals, a 6×6×6 Monkhorst-Pack grid was used [28], and an energy cutoff of 650 eV was set for the plane wave basis-set. The relaxation of the unit cell was done by the total energy minimization with breakdown conditions for the sc-loop set to $1x10^{-5}$ eV and -0.01 eV for the ionic relaxation loop.

Convex hull energy (E_{Hull}) calculations for target materials were carried out using the Pymatgen software [29]. This was done by performing relaxations on all competing phases for a given target material and creating a convex hull from their total ground state energies (TGSE). Competing phases for a target material were selected as stable compounds (E_{Hull} = 0 meV/atom), which consisted of elements present in the target material.

6.3. Results

$Mg_{2.75}X_{0.125}N_2$ (X = Zr, Sn, Si)

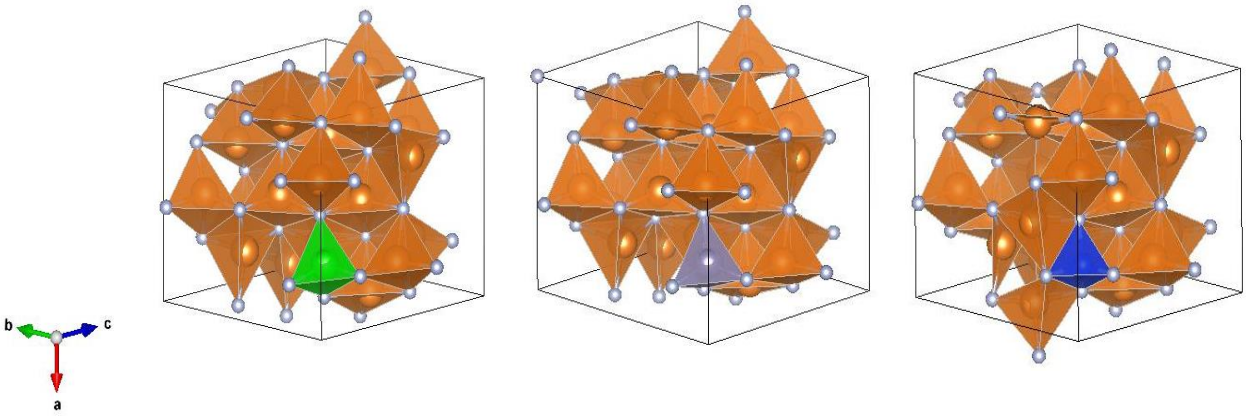

Figure 6.3. $Mg_{2.75}X_{0.125}N_2$ unit cell, Mg within favoured tetrahedral co-ordination, doped X atom within tetrahedral co-ordination. Left: $Mg_{2.75}Zr_{0.125}N_2$, Middle: $Mg_{2.75}Sn_{0.125}N_2$, Right: $Mg_{2.75}Si_{0.125}N_2$.

The cubic closed packed array anti-bixbyite $Mg_{2.75}X_{0.125}N_2$ structure the dopant ions, Zr, Sn, and Si are all doped into and substituting Mg at the tetrahedral (*48e*) site to create a vacancy of $X_{0.125}$ per formula unit, their crystal structures can be seen in **figure 6.3**. The structures convex hull energies were all calculated relative to their competing phases, which consisted of primarily binary compounds formed of nitrides. All three dopant structures were found to have convex hull energies above the hull with energies of 39, 31 and 57 meV/atom above the hull for the Zr, Sn and Si doped structures, respectively. The calculated energies are displayed in **Table 6.2** below.

Table 6.2. Convex Hull Energies of $Mg_{2.75}X_{0.125}N_2$ (M = Zr, Sn, Si) target materials.

Structure	TGSE (eV)	Energy/Atom (eV/atom)	E_{hull} (meV/atom)
$Mg_{2.75}Zr_{0.125}N_2$	-204.710	-5.248	39
$Mg_{2.75}Sn_{0.125}N_2$	-196.250	-5.032	31
$Mg_{2.75}Si_{0.125}N_2$	-200.694	-5.146	57

As a result of having energies above the hull, all 3 doped structures had more favourable decomposition. Decomposition of the $Mg_{2.75}Zr_{0.125}N_2$ favoured Zr_3N_4 and Mg_3N_2 both binary nitrides with a predicted ratio of 94% Mg_3N_2 and 6% Zr_3N_4 being formed. For $Mg_{2.75}Sn_{0.125}N_2$, the decomposition favoured binary nitrides of Sn_3N_4 and Mg_3N_2, similar to the decomposition of the Zr doped structures, with a similar ratio of formation of 94% Mg_3N_2 and 6% Zr_3N_4. For the Si doped structure, $Mg_{2.75}Si_{0.125}N_2$, the decomposition favoured $MgSiN_2$ with a formation ratio of 10% and Mg_3N_2 with a formation ratio of 90%.

$Mg_{2.625}X_{0.25}N_2$ (X = Al, Ga, In)

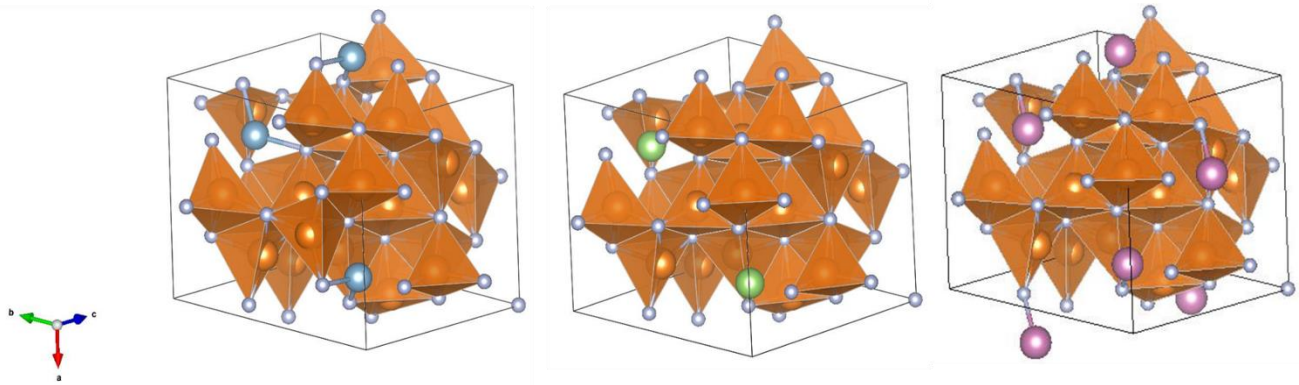

Figure 6.4. $Mg_{2.625}X_{0.25}N_2$ unit cell, Mg within favoured tetrahedral co-ordination, doped X atom within tetrahedral co-ordination. Left: $Mg_{2.625}Al_{0.25}N_2$, Middle: $Mg_{2.625}Ga_{0.25}N_2$, Right: $Mg_{2.625}In_{0.25}N_2$. Orange atoms are Mg^{2+}, large grey atoms are Al^{3+}, large green atoms are Ga^{3+}, large purple atoms are In^{3+}, and the small grey atoms are N^{3-} atoms.

The cubic closed packed array anti-bixbyite was also doped with Al, Ga, and In into the Mg tetrahedral (*48e*) site of the Mg_3N_2 structure to create a vacancy of $X_{0.125}$ per formula unit with the resultant structure of $Mg_{2.625}X_{0.25}N_2$, their crystal structures can be seen in **figure 6.4**. From the convex hull energy calculations for all three doped structures, energies of 51, 43, and 40 meV/atom were found for $Mg_{2.625}Al_{0.25}N_2$, $Mg_{2.625}Ga_{0.25}N_2$, and $Mg_{2.625}In_{0.25}N_2$, respectively. The calculated energies are displayed in **table 6.3** below. As a result of having energies above the hull, all 3 doped structures had more favourable decomposition. $Mg_{2.625}Al_{0.25}N_2$ was found to have favourable decomposition of binary nitrides, AlN, and Mg_3N_2 with a formation ratio of 10% AlN and 90% Mg_3N_2. For the

decomposition of $Mg_{2.625}Ga_{0.25}N_2$, the binary nitrides of GaN and Mg_3N_2 was found to be more favourable with a similar formation ratio of 10% GaN and 90% Mg_3N_2. For $Mg_{2.625}In_{0.25}N_2$ the favourable decomposition similar to both other doped structures was found to be InN and Mg_3N_2 with the same formation ratio of 10% InN and 90% Mg_3N_2.

Table 6.3. Convex Hull Energies of $Mg_{2.625}X_{0.25}N_2$ (M = Al, Ga, In) target materials.

Structure	TGSE (eV)	Energy/Atom (eV/atom)	E_{hull} (meV/atom)
$Mg_{2.625}Al_{0.25}N_2$	-202.429	-5.190	51
$Mg_{2.625}Ga_{0.25}N_2$	-197.304	-5.059	43
$Mg_{2.625}In_{0.25}N_2$	-194.366	-4.984	40

Mg_3N_2 Silicide

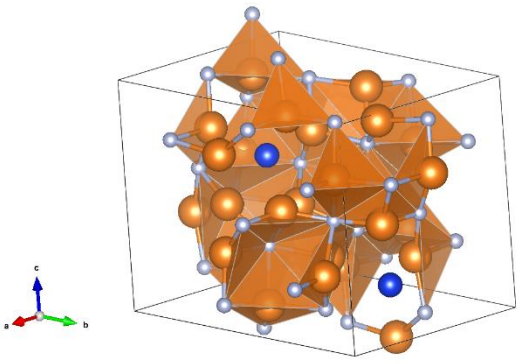

Figure 6.5. $Mg_{3.125}N_{1.75}Si_{0.25}$ unit cell, Mg within favoured tetrahedral co-ordination. Silicide positioned in the 6-fold co-ordinated N sites. Orange atoms are Mg^{2+} atoms, blue atoms are Si^{4-} atoms, grey atoms are N^{2-} atoms.

Silicide doped Mg_3N_2 was also studied. The Si^{4-} silicide anion in this structure was doped into the close packed cubic array at the 6-fold co-ordinated N sites. This generates an increased ratio of Mg within the structure increasing from 3 Mg ions per formula unit in Mg_3N_2, to 3.125 Mg ions per formula unit in a silicide doped $Mg_{3.125}N_{1.75}Si_{0.25}$. The convex hull calculation identified the most

stable doped conformation to be 135 meV/atom above the hull. The calculated energy for the silicide doped structure can be seen below in **table 6.4**. Decomposition of this structure favoured Mg_2Si and Mg_2N with a formation ratio of 15% Mg_2Si and 85% Mg_2N.

Table 6.4. Convex Hull Energies of $Mg_{2.625}X_{0.25}N_2$ (M = Al, Ga, In) target materials.

Structure	TGSE (eV)	Energy/Atom (eV/atom)	E_{hull} (meV/atom)
$Mg_{3.125}N_{1.75}Si_{0.25}$	-186.923	-4.559	135

6.4. Discussion

As mentioned in the introduction the rationale for doping the Mg_3N_2 anti-bixbyite structure with various metals is to introduce vacancies within the structure. With the cubic closed packed array anti-bixbyite being considered an ideal candidate for divalent Mg^{2+} conductivity. The combination of introducing vacancies within an ideal structure is to attempt to induce and enhance conductivity within the structure.

For the $Mg_{2.75}X_{0.125}N_2$ (X = Zr, Sn, Si) structures, all calculations identified that the structures had energies above the convex hull. Although, for $Mg_{2.75}Zr_{0.125}N_2$ and $Mg_{2.75}Sn_{0.125}N_2$, with energies above the hull of 39 and 31 meV/atom, respectively, their energies are within the 0-50 meV/atom range of being considered metastable, whereas for $Mg_{2.75}Si_{0.125}N_2$ has an energy above the hull of 57 meV/atom, therefore this structure is considered unstable. The primary factor behind the instability of these compounds is the competing stability from the anti-bixbyite Mg_3N_2 and the binary nitrides of the dopant cations. As seen from the decomposition from these structures the Mg_3N_2 structure along with the binary nitride of the dopant cations, Zr_2N_3, Sn_3N_4 and for Si, a ternary nitride $MgSiN_2$, their high stability relative to the target structures leads to the hull being formed by the binary and ternary nitrides forcing the convex hull energy of the target structures to be above the hull.

For the $Mg_{2.625}X_{0.25}N_2$ (X = Al, Ga, In) structures, the structures were also found to be all above the convex hull. $Mg_{2.625}Ga_{0.25}N_2$ and $Mg_{2.625}In_{0.25}N_2$ had convex hull energies of 43 meV/atom and 39 meV/atom above the hull, respectively, therefore they are also considered as metastable. $Mg_{2.625}Al_{0.25}N_2$ has a convex hull energy of 51 meV/atom above the hull, so is narrowly considered unstable. Similar to the $Mg_{2.75}X_{0.125}N_2$ (X = Zr, Sn, Si) structures, the instability seen from these doped structures is a result of the high stability of their competing phases. For each structure decomposition is seen to form the anti-bixbyite closed cubic packed array of Mg_3N_2 and binary nitrides of the dopant cation, AlN, GaN, and InN.

Silicide doping of the Mg_3N_2 was carried out to create a structure which had an increased ratio of Mg^{2+} mobile ions within the structure. By substituting N with the silicide ion, an increased ratio of Mg^{2+} is required to charge balance the structure. Moving the target structure along the solid-state solution of Mg_3N_2 Mg_2Si. The convex hull energy of $Mg_{3.125}N_{1.75}Si_{0.25}$ of 135 meV/atom is considered unstable, with the decomposition into the Mg_2Si and Mg_2N, the competing phases are considered too stable for the silicide doped structure to form.

From all Mg_3N_2 structures studied, the experimental synthesis of the structures was only considered for $Mg_{2.75}Zr_{0.125}N_2$, $Mg_{2.75}Sn_{0.125}N_2$, $Mg_{2.625}Ga_{0.25}N_2$, and $Mg_{2.625}In_{0.25}N_2$. The attempted synthesis of these compounds was carried out and found that products formed align with the decomposition calculated by the convex hull energy calculations. Further research is required to investigate the metastable Zr, Sn, Ga and In doped structures to identify if different methods of synthesis would be successful in creating these compounds. With any successful synthesis of the compounds, their conductivities would be of particular interest, to identify what the impact on inducing vacancies and disorder would have on the conductivity. It would also be impactful to identify if the proposed rationale that a closed cubic packed array with a tetrahedral stable Mg^{2+} site and an octahedral vacancy site would support improved conductivities from the synthesised compounds.

6.5. Conclusion

In this study, we have reported the computational convex hull energy studies carried out on $Mg_{2.75}X_{0.125}N_2$ (X = Zr, Sn, Si), $Mg_{2.625}X_{0.25}N_2$ (X = Al, Ga, In) and the $Mg_{3.125}N_{1.75}Si_{0.25}$ structures using Pymatgen software to create disorder and identify the appropriate conformers. The objective of this study was to try and identify a new potential candidate as a divalent solid-state electrolyte by creating structurally doped vacancies within the anti-bixbyite structure by introducing a trivalent and tetravalent cation, removing Mg ions to charge balance the structure, and also to increase the ratio of Mg^{2+} ions within the structure by substituting N with Si ions and introducing more Mg ions to charge balance the structure, moving the structure along the solid state solution of Mg_3N_2 and Mg_2Si. The study found that the $Mg_{2.75}Zr_{0.125}N_2$, $Mg_{2.75}Sn_{0.125}N_2$, $Mg_{2.625}Ga_{0.25}N_2$, and $Mg_{2.625}In_{0.25}N_2$ structures were all considered metastable, with the remaining structures having convex hull energies too high relative to the hull to be considered metastable. Synthesis of the compounds was attempted but unfortunately was unsuccessful. The study has identified that the potential to explore multi-valent ionic conductors is an area which can potentially provide new conductors, further experimental synthesis attempts can potentially create doped anti-bixbyite structures as potential solid-state electrolytes.

6.6. References

1 M. Liu, Z. Rong, R. Malik, P. Canepa, A. Jain, G. Ceder and K. A. Persson, *Energy Environ. Sci.*, 2015, **8**, 964–974.

2 P. Canepa, S.-H. Bo, G. Sai Gautam, B. Key, W. D. Richards, T. Shi, Y. Tian, Y. Wang, J. Li and G. Ceder, *Nat. Commun.*, 2017, **8**, 1759.

3 J. Koettgen, C. J. Bartel and G. Ceder, *Chem. Commun.*, 2020, **56**, 1952–1955.

4 D. Aurbach, Z. Lu, A. Schechter, Y. Gofer, H. Gizbar, R. Turgeman, Y. Cohen, M. Moshkovich and E. Levi, *Nature*, 2000, **407**, 724–727.

5 H. D. Yoo, I. Shterenberg, Y. Gofer, G. Gershinsky, N. Pour and D. Aurbach, *Energy Environ. Sci.*, 2013, **6**, 2265.

6 J. Muldoon, C. B. Bucur and T. Gregory, *Chem. Rev.*, 2014, **114**, 11683–11720.

7 E. Levi, Y. Gofer and D. Aurbach, *Chem. Mater.*, 2010, **22**, 860–868.

8 S. Ikeda, M. Takahashi, J. Ishikawa and K. Ito, *Solid State Ionics*, 1987, **23**, 125–129.

9 N. Imanaka, Y. Okazaki and G. Adachi, *Ionics (Kiel).*, 2001, **7**, 440–446.

10 S. Higashi, K. Miwa, M. Aoki and K. Takechi, *Chem. Commun.*, 2014, **50**, 1320–1322.

11 A. Mitelman, M. D. Levi, E. Lancry, E. Levi and D. Aurbach, *Chem. Commun.*, 2007, 4212.

12 W. Yu, D. Wang, B. Zhu, S. Wang and L. Xue, *Solid State Commun.*, 1987, **61**, 271–273.

13 Y. Zheng, Y. NuLi, Q. Chen, Y. Wang, J. Yang and J. Wang, *Electrochim. Acta*, 2012, **66**, 75–81.

14 M. E. Spahr, P. Novák, O. Haas and R. Nesper, *J. Power Sources*, 1995, **54**, 346–351.

15 W. Yuan, *Solid State Ionics*, 1995, **76**, 253–258.

16 N. Amir, Y. Vestfrid, O. Chusid, Y. Gofer and D. Aurbach, *J. Power Sources*, 2007, **174**, 1234–1240.

17 J. Yin, A. B. Brady, E. S. Takeuchi, A. C. Marschilok and K. J. Takeuchi, *Chem. Commun.*, 2017, **53**, 3665–3668.

18 Z. Rong, R. Malik, P. Canepa, G. Sai Gautam, M. Liu, A. Jain, K. Persson and G. Ceder, *Chem. Mater.*, 2015, **27**, 6016–6021.

19 I. D. Brown, *Acta Crystallogr. Sect. B Struct. Sci.*, 1988, **44**, 545–553.

20 Y. Wang, W. D. Richards, S. P. Ong, L. J. Miara, J. C. Kim, Y. Mo and G. Ceder, *Nat. Mater.*, 2015, **14**, 1026–1031.

21 R. D. Shannon, *Acta Crystallogr. Sect. A*, 1976, **32**, 751–767.

22 A. Jain, S. P. Ong, G. Hautier, W. Chen, W. D. Richards, S. Dacek, S. Cholia, D. Gunter, D. Skinner, G. Ceder and K. A. Persson, *APL Mater.*, 2013, **1**, 011002.

23 D. E. Partin, D. J. Williams and M. O'Keeffe, *J. Solid State Chem.*, 1997, **132**, 56–59.

24 F. Hintze, N. W. Johnson, M. Seibald, D. Muir, A. Moewes and W. Schnick, *Chem. Mater.*, 2013, **25**, 4044–4052.

25 J. P. Perdew, K. Burke and M. Ernzerhof, *Phys. Rev. Lett.*, 1996, **77**, 3865–3868.

26 G. Kresse and J. Furthmüller, *Phys. Rev. B*, 1996, **54**, 11169–11186.

27 W. H. Press, B. P. Flannery, S. A. Teukolsky, W. T. Vetterling and H. Gould, *Am. J. Phys.*, 1987, **55**, 90–91.

28 H. J. Monkhorst and J. D. Pack, *Phys. Rev. B*, 1976, **13**, 5188–5192.

29 S. P. Ong, W. D. Richards, A. Jain, G. Hautier, M. Kocher, S. Cholia, D. Gunter, V. L. Chevrier, K. A. Persson and G. Ceder, *Comput. Mater. Sci.*, 2013, **68**, 314–319.

6.7. Supporting Information

Phase Diagrams

$Mg_{2.75}Zr_{0.125}N_2$

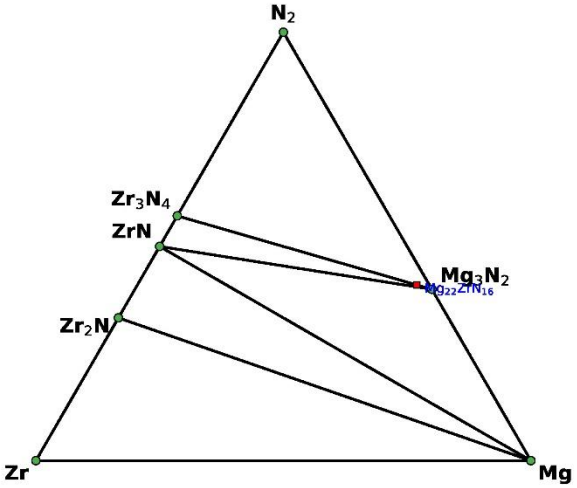

$Mg_{2.75}Sn_{0.125}N_2$

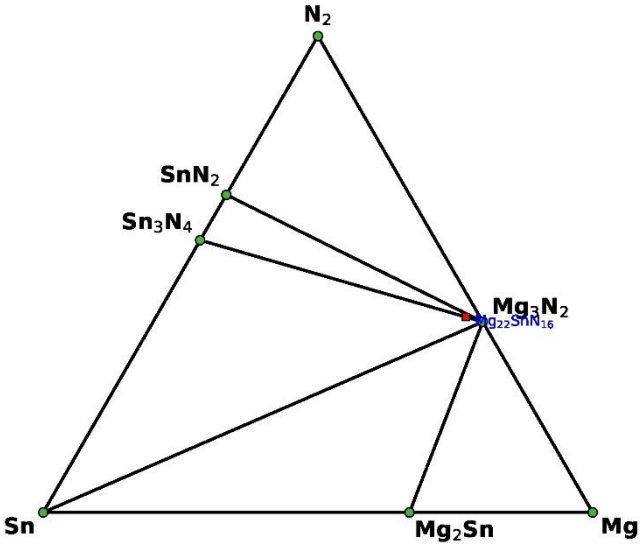

$Mg_{2.75}Si_{0.125}N_2$

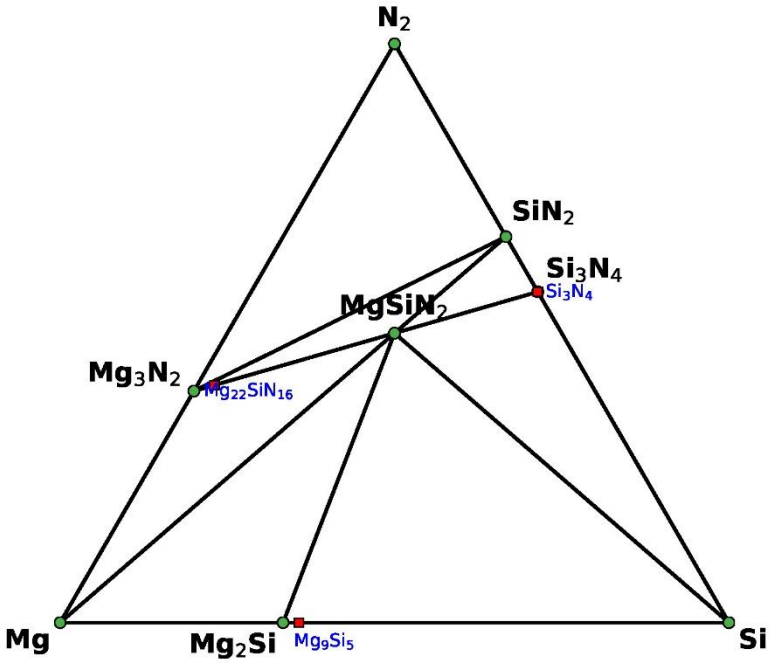

$Mg_{2.625}Al_{0.25}N_2$

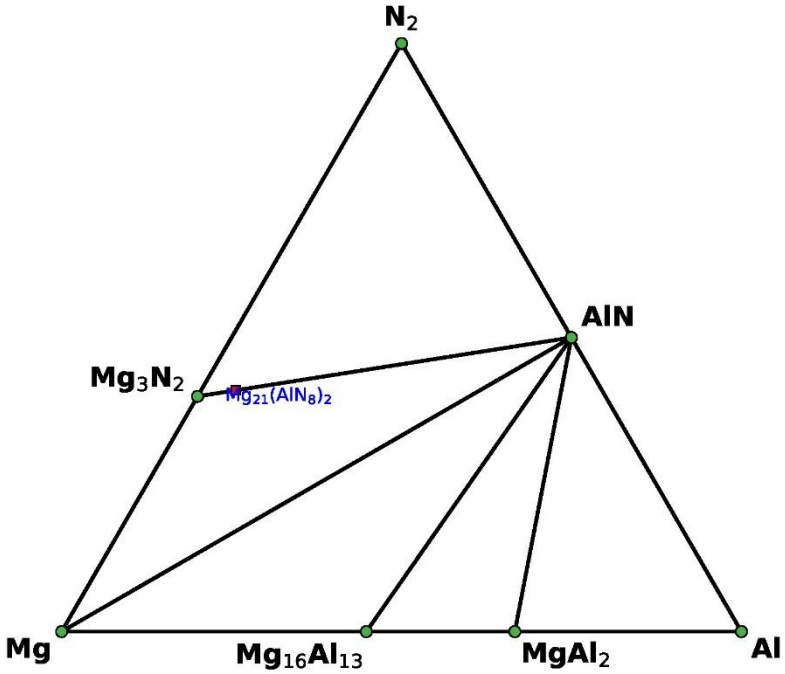

$Mg_{2.625}Ga_{0.25}N_2$

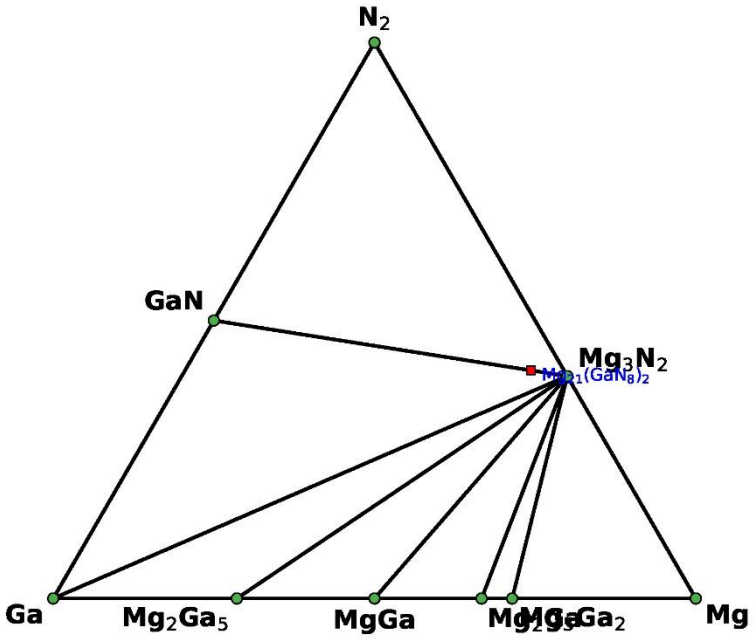

$Mg_{2.625}In_{0.25}N_2$

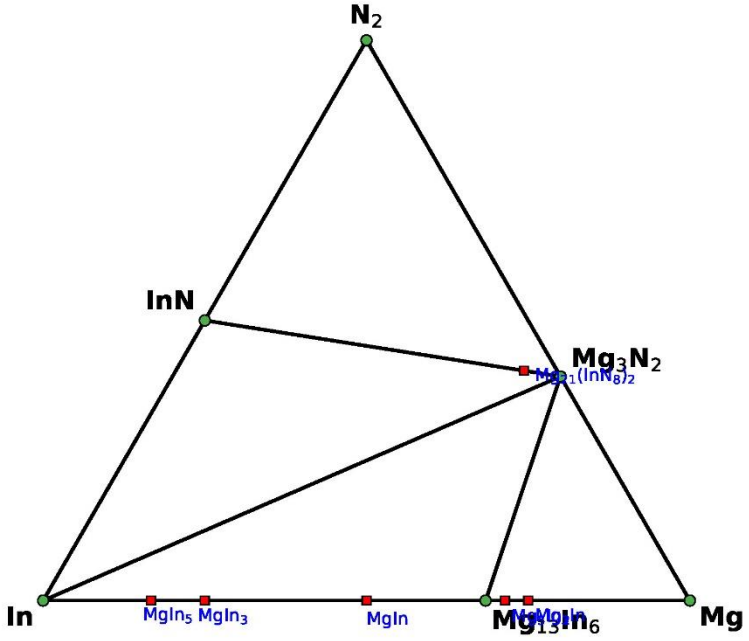

$Mg_{3.125}N_{1.75}Si_{0.25}$ (Silicide)

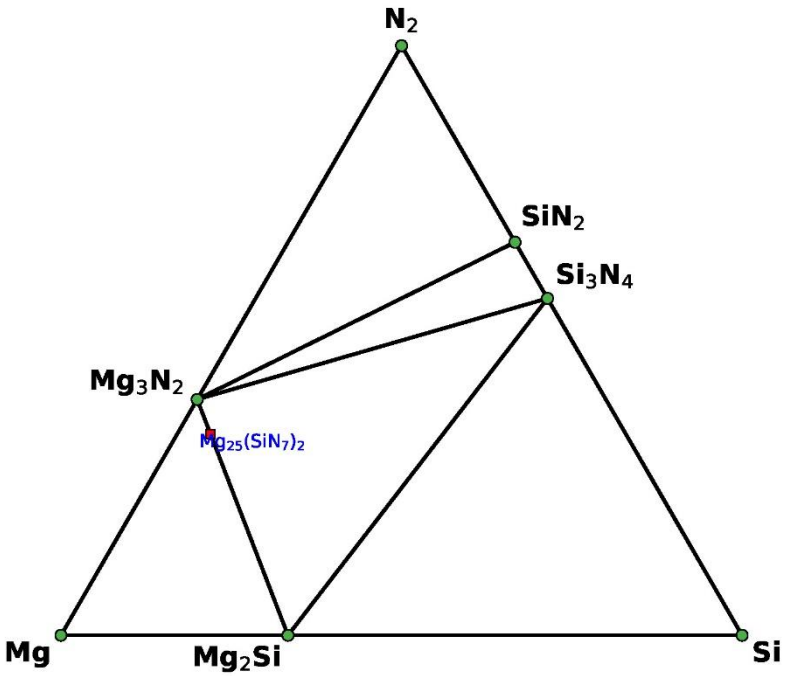

Chapter 7: Concluding the Investigation

In my thesis the computational investigation into identifying solid-state superionic conductors has been carried out in four distinct chapters which are separated by crystal structural families and/or the computational methods used. Different approaches were used in an attempt to identify new potential superionic conductor candidates from high-throughput methods to more specific structural investigations. DFT methods along with Bond-valence methods were used. The conclusions of each chapter in given at the end of each one. The summary of each chapter of research is given once again in this section.

The research carried out which has been demonstrated in this thesis has given new insight into a series of different structural families such as the lithium rich anti-perovskite and the doping of known structures such as the anti-bixbyite magnesium structure, demonstrating that using tolerance factors can indeed lead to identifying new structures using the convex hull energies of the structures as a reflection of stability, that the computational approach can be used as a precursor to synthesis. The computational study of the $Na_2Fe_2OS_2$ oxychalcogenide also demonstrates that not only as a precursor but our methods can be used retrospective to the synthesis of compounds in providing a better understanding of the structure, such as identifying the magnetic ordering and the convex hull energy of the structure. Whilst these approaches to identifying new candidates are successful, a new outlook must be considered which adopts high-throughput calculations which will allow for an accelerated approach of probing large datasets of structures. The study into using the Bond Valence Sum Mapping method to identify new metrics such as the valence density and pathway hopping distance as a potentially indicative method of identifying conductors, whilst no strong correlation was found, it has opened new potential research into those metrics.

Further studies of lithium rich anti-perovskites using the tolerance factor as an indicator of suitability for cation and anion combinations, similarly through manipulating crystal structures to create vacancies via doping such as the magnesium anti-bixbyite will lead to the identification of new materials and potentially superionic conductors. Through further study of the high-throughput approach of using bond valence sum mapping with a combination of metrics and a larger dataset will lead to a better understanding of correlation between analytical metrics and conductivity. This in turn will lead to accelerated discovery of conductors.